UNIVERSITÀ DEGLI STUDI DI BERGAMO
Facoltà di Ingegneria
Dipartimento di Ingegneria Industriale

DOTTORATO DI RICERCA
IN
TECNOLOGIE PER L'ENERGIA E L'AMBIENTE

XXVIII ciclo

anno 2016

Numerical investigation of primary break-up of conical swirled jets

Doctoral thesis:
Claudio Galbiati

Supervisors:
Prof. G. E. Cossali
Eng. S. Tonini

Dipartimento di Ingegneria e Scienze Applicate. Università degli studi di Bergamo
ISBN 978-88-97413-17-2
Open access copy available at: http://hdl.handle.net/10446/53313

Abstract

Primary break-up is a hard element to be described into the atomization chain, since experimental works are rare especially for swirl atomizers. In the past, different models had been developed to define the mechanism which leads to break-up of jets and, in this way, the characteristics of the sub-sequent produced spray. These models had been validated against experimental data in simplified conditions, for example using round jets; however they cannot be generalized for all the other categories. Moreover, these models were based on simplified assumptions, for example they neglected turbulence. Thus their application to conical swirled jets is tricky and could produce misleading results. In absence of experimental data, Volume of Fluid Direct Numerical Simulations (VOF DNS) could help to provide more information about the produced primary spray and its characteristics, such as droplets velocity components, location, size and shape in the whole investigated domain.
However, in order to simulate conical swirled jets from aeronautical pressure swirl atomizers, realistic velocity profiles of both liquid and gas phases together with the characteristics of the external environment are required as input parameter. Semi-empirical or analytical correlations, indeed, may provide an estimation of these data, but they can be properly applied only to a small group of test cases, if compared with the huge amount of possible configurations with different geometries, liquid properties and operating conditions. VOF RANS and LES are performed to provide the internal nozzle flow characteristics, and the subsequent initial jet characteristics.
For this reasons, in this work VOF Reynolds Averaged Navier-Stokes (RANS) and Large Eddy Simulation (LES) have been performed to provide a proper

simulation of the internal nozzle flow and the subsequent initial jet characteristics. In addition, a sensitivity analysis has been performed to evaluate the effect of various turbulence model (i.e. RNG $k - \epsilon$, Reynolds Stress Model and LES) on the final numerical results.
Then, these informations have been applied to reproduce the following jet development and its subsequent break-up. To reach this goal a DNS code from the University of Stuttgart, Free Surface 3D (FS3D), has been adapted and used. As shown, the achieved results could be useful to define the principal phenomena involved in the atomization process. Moreover, comparison with a well known analytical method are presented in order to underline possible drawback and improvements.
For both the internal and the external flow numerical simulations, a grid dependence study, as well as the effect of various operating conditions, has been investigated to exclude any important and unwanted dependences.

Keywords: Pressure Swirl Atomizer, Conical Swirled Jet, DNS, Primary break-up.

Acknowledgments

Part of the research leading to these results has received funding from the FIRST (Fuel Injector Research for Sustainable Transport) Project (FP7/2007-2013) under grant agreement n. 265848. The author would like to acknowledge AVIO Group for providing the injector geometry and operating conditions.

Thank to Prof. G. E. Cossali for the opportunity to be part of his group, providing all the required tools and knowledge to carry on the research activities. Thank to Dr. S. Tonini for her support and help on the setup and analysis of the internal nozzle flow simulations. The author would like to acknowledge the Eng. P. Conti for his support on the setup of the internal nozzle flow simulation and the Super Computing Applications and Innovation System (SCAI CINECA) for the numerical resources made available to perform the numerical simulations of the atomizer internal flow.

The author acknowledges the Prof. B. Weigand and the ITLR (Institut

für Thermodynamik der Luft-und Raumfahrt) department of University of Stuttgart for the hospitality and for the possibility to use their numerical code (FS3D) to investigate the conical swirled jet break-up. A special thank is for Dipl.-Eng. M. Ertl for his support on the setup of the simulations with the FS3D code, and for the High Performance Computing Center Stuttgart (HLRS) for the numerical resources made available to perform the simulations of the conical swirled jet break-up.

Thanks are, finally, due to Cariplo Foundation for its financial support through the grant *"FYRE - Fostering Young REsearchers"* which partially supported the 7 months period spent at the University of Stuttgart.

Contents

Nomenclature

$2h$	Liquid film thickness $[m]$
$2h_b$	Liquid lamella thickness at the break-up point $[m]$
$2h_o$	Liquid film thickness at the atomizer exit section $[m]$
$2h_\alpha$	Liquid lamella thickness evaluated at the exit section of the atomizer considering the phase variable α $[m]$
$2h_{K_v}$	Liquid lamella thickness evaluated at the exit section of the atomizer considering flow field informations (ΔP and K_v) extracted from the simulations $[m]$
$2h_{P_{Go}=0}$	Liquid lamella thickness evaluated at the exit section of the atomizer considering the point where the gauge pressure becomes equal to 0 $[m]$
α	Phase variable adopted into the VOF method
β	Angle of the convergent section of the atomizer $[deg]$
ΔP	Pressure drop the whole atomizer $[bar]$
ΔP_σ	Differential pressure force across the surface boundary $[Pa]$

ΔP_{hole}	Pressure drop the nozzle of the atomizer $[bar]$
$\dot{m}_l$	Liquid mass flow rate $[kg/s]$
ϵ_t	Liquid turbulent dissipation rate at the exit section of the atomizer $[m^2/s^3]$
ϵ_{in}	Turbulent dissipation rate at inlet section $[m^2/s^3]$
η	Wave amplitude $[m]$
η_0	Initial wave amplitude $[m]$
η_b	Wave amplitude at the jet break-up point $[m]$
η_c	Grid cell size $[m]$
η_k	Kolmogorov length scale $[m]$
λ	Wave length $[m]$
Λ_s	Wave length of the most unstable wave $[m]$
μ_l	Liquid dynamic viscosity $[Pas]$
ω	Complex wave growth rate $[m/s]$
ω_i	Imaginary part of the wave growth rate $[m/s]$
ω_r	Real part of the wave growth rate $[m/s]$
Ω_s	Growth rate real part of the most unstable wave $[m/s]$
$\overline{w_i}$	Averaged tangential velocity induced by the inlet channels $[m/s]$
$\overrightarrow{k}$	External body force vector $[m/s^2]$
$\overrightarrow{u}$	Velocity vector $[m/s]$
$\overrightarrow{V}$	Liquid velocity vector $[m/s]$

ρ	Density $[kg/m^3]$
ρ_g	Gas density $[kg/m^3]$
ρ_l	Liquid density $[kg/m^3]$
σ	Surface tension $[N/m]$
$\sqrt{\overline{\vec{u}'}^2}$	Averaged turbulent velocity fluctuations $[m/s]$
τ	Break-up time $[s]$
$\tau_{r,\theta}$	Shear stress along the radial and the azimuthal coordinate $[N/m^2]$
θ	Spray cone angle $[deg]$
$\theta(x)$	Spray cone angle defined considering the Rizk and Lefebvre [69] definition $[deg]$
$\theta_{tan}(x)$	Spray cone angle defined considering the angle of the tangent line at the external edge profile along the axial direction x $[deg]$
θ_{VR}	Spray cone angle defined considering the liquid velocity ratio at the exit section of the atomizer $[deg]$
$\widehat{n}_\gamma$	Normal vector to the liquid surface (positive coming out the liquid
A_e	Maximum distance of the liquid structure surface from its center of gravity $[m]$
a_e	Minimum distance of the liquid structure surface from its center of gravity $[m]$
A_i	Total inlet area $[m^2]$
A_o	Outlet section area $[m^2]$
$A_{o,ac}$	Air-core area at the outlet section of the atomizer $[m^2]$

AR	Aspect ratio []
C	Constant coefficient
C_d	Discharge coefficient []
d_c	Injection chamber diameter $[m]$
d_D	Droplet diameter after the jet break-up $[m]$
d_d	Calculated droplet diameter from the simulations $[m]$
d_i	Inlet channel diameter $[m]$
d_L	Ligament diameter $[m]$
d_o	Nozzle diameter $[m]$
d_r	Infinitesimal variation of the radial position of the fluid particle p
d_s	Swirl chamber diameter $[m]$
d_x	Grid cell size along the axial direction $[m]$
d_{ac}	Air-core diameter $[m]$
$d_{d,max}$	Biggest measured/calculated droplet diameter $[m]$
$d_{d,min}$	Smallest measured/calculated droplet diameter $[m]$
d_{Hi}	Hydraulic diameter of the inlet channel $[m]$
$d_{L,DNS}$	Ligament diameter extracted from the DNS simulations $[m]$
dy	Grid cell size along the y direction $[m]$
dz	Grid cell size along the z direction $[m]$
F_c	Centrifugal force $[N]$

F_p	Induced pressure force $[N]$
f_γ	Surface tension resulting force $[N/m^3]$
FN	Flow number $[m^2]$
g	Gravity acceleration - 9.81 $[m/s^2]$
h	Half of the liquid lamella thickness $[m]$
h_o	Half of the liquid lamella thickness at the exit section of the atomizer $[m]$
I	Identity matrix
J	Constant variation of liquid lamella thickness $[sm]$
K	Atomizer constant $A_i/(d_s d_o)$ []
k	Wave number $[m^{-1}]$
K_s	Wave number of the most unstable wave $[m^-1]$
k_t	Liquid turbulent kinetic energy at the exit section of the atomizer $[m^2/s^2]$
K_v	Velocity coefficient []
K_ϵ	Constant parameter set equals to 1
k_{in}	Turbulent kinetic energy at inlet section $[m^2/s^2]$
$K_{S,DNS}$	Wave number of the most unstable wave extracted from the DNS VOF simulations $[m^-1]$
KF	Kolmogorov factor []
L_b	Break-up length $[m]$
l_c	Injection chamber length $[m]$

l_i	Length of the tangential inlet channels $[m]$
l_o	Length of the nozzle (hole) of the atomizer $[m]$
l_s	Length of the swirl chamber $[m]$
L_t	The largest turbulent fluctuation $[m]$
$L_{b,h}$	Break-up length defined in correspondence of the axial distance x where the first hole can be found on the liquid film $[m]$
$L_{b,s}$	Break-up length evaluated adopting the Dumochel et al. [16] definition $[m]$
L_{in}	Turbulent length scale at the inlet section $[m]$
$l_{s,c}$	Length of the convergent section of the pressure swirl atomizer $[m]$
m_p	Mass of a generic fluid particle $[kg]$
Oh	Ohnesorge number []
P	Pressure $[bar]$
p	Fluid particle
P_c	Injection chamber pressure $[bar]$
$P_j(x)$	Perimeter of the jet liquid interface in correspondence of the axial distance x $[m]$
P_{Go}	Gauge pressure at the exit section of the atomizer $[bar]$
Q	Ratio between gas and liquid density ρ_g/ρ_l []
Q_l	Volumetric liquid flow rate $[m^3/s]$
r	Radial coordinate $[m]$

r_b	Radial distance of the external edge of the jet $[m]$
r_i	Inlet channel radius $[m]$
r_m	Distance between the inlet channel axis and the atomizer axis $[m]$
r_o	Nozzle radius $[m]$
r_p	Initial radial distance of the mass particle m_p from the atomizer axis $[m]$
r_v	Radial distance from the atomizer axis where the swirl velocity profile change from a solid body rotation vortex profile to a free vortex profile
r_{ac}	Air-core radius $[m]$
$r_{ext}(x)$	External jet edge profile along the axial direction x $[m]$
$r_{o,ac}$	Air-core radius at the exit section of the atomizer $[m]$
r_o	Nozzle radius $[m]$
Ra	Surface roughness $[m]$
Re_i	Reynolds number evaluated at the inlet channel []
Re_o	Reynolds number evaluated at the exit section of the atomizer []
Re_t	Turbulent Reynolds number []
Re_{HL}	Reynolds number defined by Horvay and Leuckel [32] []
Re_W	Reynolds number defined by Walzel [89] []
S	Stress tensor
S_0	Swirl number adopted by Horvay and Leuckel [32] to define X []
$S_j(x)$	Jet liquid interface in correspondence of the axial distance x $[m^2]$

S_{HL}	Swirl number defined by Horvay and Leuckel [32] []
St	Strouhal number []
St_1	Strouhal number of the precession mode []
St_2	Strouhal number of the helical mode []
t	Time $[s]$
TI	Turbulent intensity []
U	Magnitude of the relative liquid-gas velocity $[m/s]$
U_i	Characteristic velocity of the flow within the inlet channel $[m/s]$
u_o	Liquid axial velocity at the exit section of the atomizer $[m/s]$
u_{axial}	Liquid axial velocity $[m/s]$
u_{in}	Liquid velocity component along the x direction $[m/s]$
u_{radial}	Liquid radial velocity $[m/s]$
u_{swirl}	Swirl velocity component $[m/s]$
V	Absolute liquid velocity magnitude $[m/s]$
v_l	Liquid kinematic viscosity $[m^2/s]$
v_{in}	Liquid velocity component along the y direction $[m/s]$
V_{ls}	Liquid structure volume $[m^3]$
w_i	Local tangential velocity along radial direction $[m/s]$
W_s	Swirl strength $[m/s]$
w_{in}	Liquid velocity component along the z direction $[m/s]$
We_g	Weber gas number []

We_l	Liquid Weber number []
We_s	Weber swirl number []
We_{gc}	Critical Weber number = 27/16 []
X	Ratio between the air-core area and the nozzle exit section area $r_{o,ac}^2/r_o^2$ - theoretical value []
x	Axial coordinate $[m]$
X^*	Corrected value of X []
z	Axial distance from the atomizer exit (positive within the atomizer) $[m]$
ARSM	Algebraic Reynolds Stress Model
DNS	Direct Numerical Simulations
LDA	Laser Doppler Anemometry
LES	Large Eddy Simulation
LEVM	Linear Eddy Viscosity Models
LIF	Laser-Induced Fluorescence
MMD	Mass Median Diameter
PDA	Phase Doppler Anemometry
PIV	Particle Image Velocimetry
RANS	Reynolds Averaged Navier-Stokes equations
RSM	Reynolds Stress Model
SMD	Sauter Mean Diameter
VOF	Volume of Fluid multiphase method

Chapter 1

Introduction

1.1 Motivation

In several industrial fields it is necessary to atomize a liquid jet into smaller droplets. The atomization process yields liquid structure with higher exposed surface (higher number of droplets instead of a single jet): this increment on the total exchange surface leads to improve the exchange phenomenon: for fire systems, the increment of the liquid surface helps to better exchange the heat, while for chemical reaction it helps to improve the mass exchange of the reagents, etc.
The break-up of a liquid jet can be induced by different phenomena, like aerodynamic force, cavitation, turbulence, etc., which occur depending on the type of atomizer. Several kind of atomizers are available which can use different mechanisms to atomize the liquid jet. One of the most common used atomizer is the Pressure Swirl Atomizer (PSA): it can be easily manufactured (it has a simple geometry) and it requires low injection energy, obtaining at the end a good mixing quality between the liquid and the environmental gas, and a rather good atomization (fine spray). For these reasons, PSA are commonly used in combustion systems such as gas turbine engines, internal combustion engines and boilers, to obtain good

quality of mixing between oxidant and fuel. Although this atomizer can be simply manufactured and used, the generated flow is really complex, and then the comprehension of the liquid behaviour cannot be easily achieved, both within and outside the atomizer. The internal flow field is really important, because it defines the initial jet characteristics (evaluated at the exit section of the atomizer). Into the injection chamber, the jet continues to develop until it breaks-up into ligaments and then into droplets under the action of aerodynamic forces. This rupture of the liquid jet is called primary break-up. This atomization stage is really important to define the following evolution of the spray (secondary break-up), but it cannot be easily investigated. Indeed, the current experimental techniques adopted to investigate the spray characteristics, as Phase Doppler Anemometry (PDA), cannot be reliably used due to the high level of noise during the measurement and also to the fact that there are different liquid structures (ligaments and droplets) which yields a drastic increment of the measurement disturbance.

The present work aims to define one methodology to investigate the primary break-up of a conical swirled jet, produced by a pressure swirl atomizers, consisting of a 3D multiphase numerical simulation of the conical swirled jet. To set-up correctly this simulation, the jet characteristics at the exit section of the atomizer must be accurately defined; this assumption is true also for the analytical models, where the emerging jet characteristic are set as input data. In literature several works able to define the initial jet characteristics using analytical assumptions or semi-empirical correlations can be found , but not all of them are able to cover the large number of geometric, fluids and operating conditions. Therefore, the investigation methodology takes into account also a multiphase numerical simulations of the internal nozzle flow, such as to provide the more realistic inlet boundary for the successive break-up investigations (analytical models or DNS).

In this work, the proposed methodology is applied to a specific atomizer for aeronautic engines, but it can be generally adopted to investigate every kind of simplex atomizers, and the subsequent jet break-up.

1.2 Thesis layout

The thesis layout will be the following:

- *Chapter 2. Pressure Swirl Atomizer*, a general description of the pressure swirl atomizer and its operating principles it is reported;
- *Chapter 3. State of the art*, a review of the atomizer internal flow field and the conical swirled jet development investigations performed in the past with experiments and simulations is shown;
- *Chapter 4. Internal nozzle flow investigations*, where the numerical set-up of the internal nozzle flow simulations are explained, and the following results are discussed;
- *Chapter 5. Conical swirled jet development and the subsequent primary break-up*, where the numerical set-up of the 3D multiphase DNS is presented, and the following break-up informations extracted are compared with an analytical model;
- *Chapter 6. Conclusion and future developments*, where the principal results of the entire work are summarized and possible improvements are proposed.

Chapter 2

Pressure swirl atomizer

2.1 General description

Conical swirled jets are produced by pressure swirl atomizers (PSA). It is one of the simplest kind of atomizer that is possible to find for its simple geometry/manufacturing with a low energy consumption [48].
Generally, it is composed by few tangential inlet channels connected to the main body of the atomizer, which is the swirl chamber (see Figure 2.1). The latter one is connected to the nozzle by a converging zone. Therefore, the liquid is forced through the channels into the swirl chamber: the tangential inlet channels induce an high angular velocity to the liquid, thereby creating the air-core vortex. After the injection into the ambient gas, the jet gradually expands due to the centrifugal force induced by the swirl motion. The final spray has a wide cone angle, which is an important desired characteristic required for different industrial applications as it is for aero-engine applications. In this case, a wide spray is required to achieve the correct mixing between the oxidant and the fuel to have an uniform combustion. The cone angle depends on the relative magnitude of the tangential and the axial components of the velocity at the exit section of the atomizer.

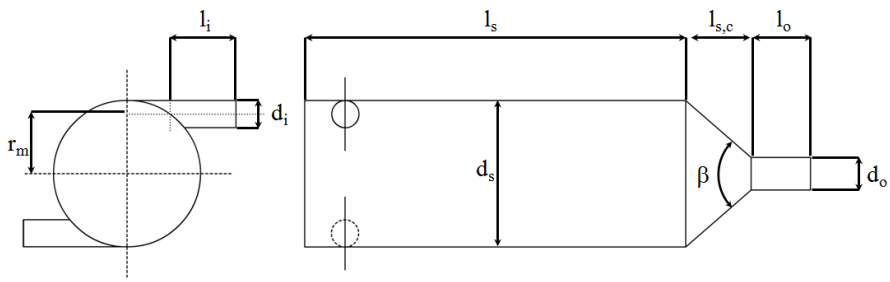

Figure 2.1: Simple geometry for a PSA.

Figure 2.1 shows a typical configuration for this kind of injector: two cylindrical inlet channels connected tangentially to the swirl chamber wall, and orthogonally to the axis of the atomizer. The swirl chamber is composed by a cylindrical part and the converging zone is a truncated cone. Changing the length of each section leads to have different performances of the atomizer, that must be evaluated case by case. More over, different topological configurations can be adopted, where they mainly differ in the method used to induce the swirl motion: for example the inlet channels can be tilted to give to the liquid an axial component together with the circumferential one.

Several authors tried to define an universal law able to describe the behaviour of this kind of atomizer by changing the geometric length of each part of the atomizer [83][24][5][48][7][96], the operating conditions and the liquid adopted; often this procedure is based on fitting the experimental data obtained changing the atomizer geometry (one parameter at time), and some of them are reported in Appendix A. However, for a strong variation of the geometry, their results cannot be representative of the real atomizer performances, and then a further validation must be carried out.

2.2 The atomizer internal flow

The qualitative description of the internal nozzle flow can be done considering the macro-scale of the flow. Starting from the inlet channels, their aim is to induce a tangential velocity to the liquid: for the geometry shown in Figure 2.1, the inlet velocity has only a tangential component, while the axial and the radial ones are equal to zero. This is true only for this specific geometry, but if the inlet channels are connected to the swirl chamber with a non zero angle to the meridian plane, the flow enters with a tangential and axial velocity components. Moreover, if the inlet channels are tilted along the axis of the atomizer, the flow enters with a all components different from zero, as it is the case for the geometry shown in Figure 2.2.

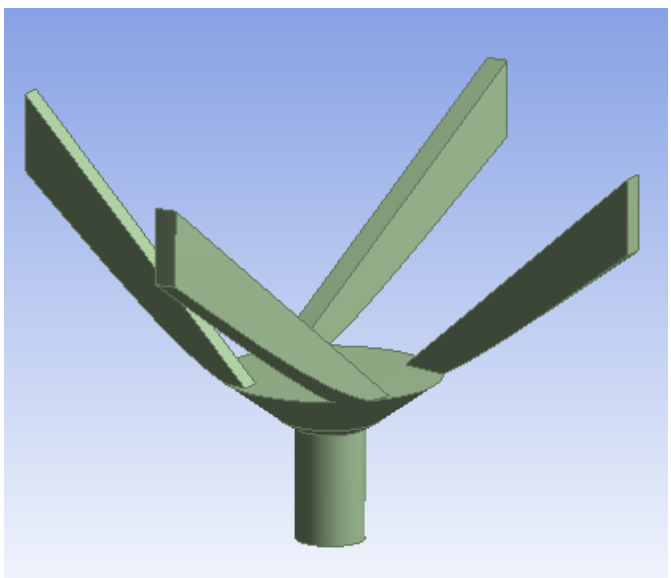

Figure 2.2: A different possible configuration of PSA: the inlet channels are not normal to the axis of the atomizer and no cylindrical swirl chamber is present ($l_s = 0$).

Just to simplify the description of the internal nozzle flow, the inlet channels are considered to be normal to the axis of the atomizer. Under this condition, the initial value of the axial velocity is null, while along the atomizer it assumes a positive value, due to the conservation of the continuity equation. The swirl motion continues to be present and its strength depends on the inlet velocity. Ideally, for a low viscosity liquid, the swirling motion can be largely irrotational, which means:

$$\nabla \times \overrightarrow{V} \tag{2.1}$$

where $\overrightarrow{V}$ represents the liquid velocity vector. This ensures that the tangential velocity component is of the form of

$$u_{swirl} \propto 1/r \tag{2.2}$$

which represents the free potential vortex (see the last part of the graph shows in Figure 2.3 for $r > r_v$). This relation must be approximately the same for a given radius at any axial position. Eq. 2.1 for an inviscid liquid, ensures that the axial velocity along the radial direction is constant ($\partial u_a/\partial r = 0$). The approximated pressure P inside the atomizer can be defined using the Bernoulli equation for irrotational flow:

$$\frac{|\overrightarrow{V}|^2}{2} + \frac{P}{\rho_l} + gx = constant \tag{2.3}$$

where ρ_l is the liquid density and gx represent the hydrostatic pressure. Usually, the latter term can be neglected, because it is order of magnitude lower than the values of the other terms present in Eq. 2.3. If viscous effects are present, they must balance the left hand side of Eq. 2.3, and lead to decrease the velocity of the liquid and increase the pressure losses. The variation of the velocity, linked to a viscous effect, can be found close to the atomizer wall, due to the presence of the boundary layer, and within the main body of the atomizer due to the presence of the viscous shear stresses. Along the tangential direction, the shear stress can be defined as:

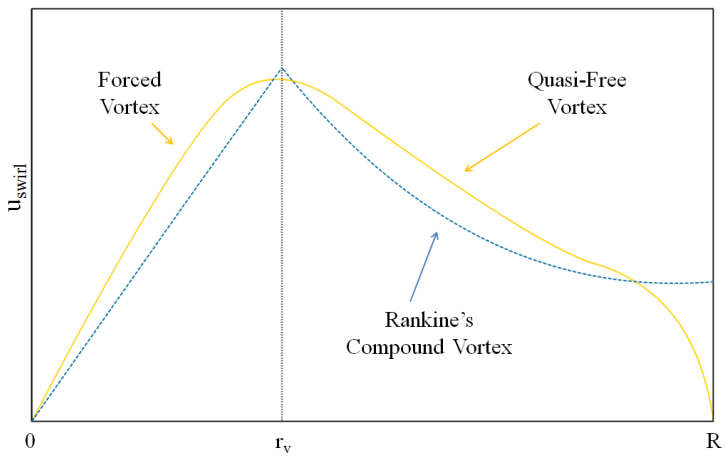

Figure 2.3: Radial distribution of the swirl (u_{swirl}) velocity in a Rankine's vortex.

$$\tau_{r,\theta} = -\mu_l \left(\frac{\partial u_{swirl}}{\partial r} - \frac{u_{swirl}}{r} + \frac{1}{r}\frac{\partial u_r}{\partial \theta} \right) \tag{2.4}$$

where μ_l represents the liquid dynamic viscosity, and u_r is the radial velocity component. Within the body of the atomizer, the latter velocity components are small and therefore they are negligible; with the assumption that the swirl velocity profile follows the relation shown in Eq. 2.2, Eq. 2.4 becomes:

$$\tau_{r,\theta} = C\frac{\mu_l}{r^2} \tag{2.5}$$

where C represent a constant coefficient which depends upon the inlet conditions. This relation indicates that the shear stress are strong near the atomizer axis: this means that the viscous effect induce the flow rotate as a solid body, where the tangential velocity increase with the radial coordinate (see the graph in Figure 2.3 for $r < r_v$).

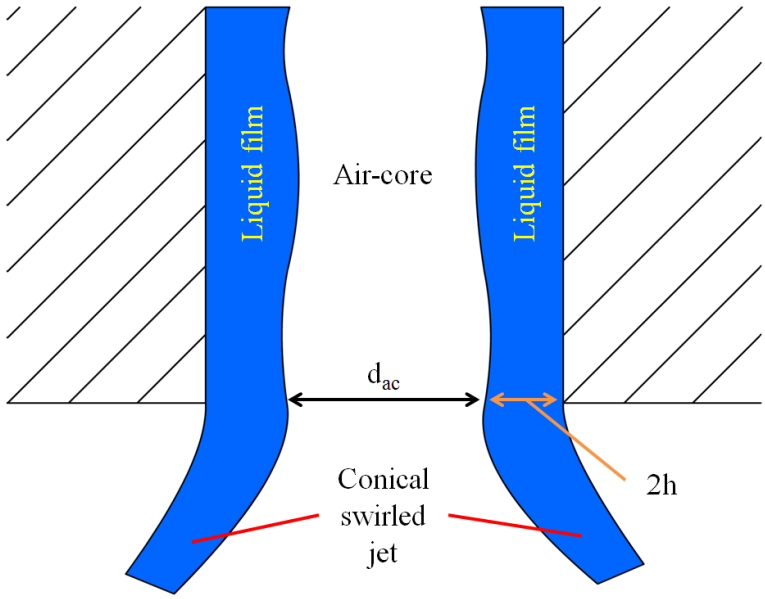

Figure 2.4: Internal and external flow structure produced by PSA.

The value of the pressure changes according to the value of the liquid velocity: considering the axial and the radial profile over the internal radius of the atomizer at different height, it can be found that the first remains almost constant (uniform), while the second it is negligible if compared with the other two velocity components. Therefore, the value of P changes with the swirl velocity (tangential components), in such a way close to the wall the pressure reaches the maximum value, while in correspondence of the main axis of the atomizer it assumes a very low value. Under this condition, from the outlet the environmental gas starts to enter inside the atomizer up to the top wall of the swirl chamber. The gas column formed is called air-core, due to its position over the axis of the atomizer (central part of the atomizer internal flow), as it can be seen in Figure 2.4.

The presence of the air-core ensures that the body of liquid within the nozzle is in the form of an annulus and that the passage of a liquid particle through the nozzle will therefore describe a helical path. From the experiments of De Keukelare [9] it has been found that the air-core diameter d_{ac} doesn't change its value for different operating pressure. When the liquid passes through the convergent section, the axial velocity component increases, to balance the mass continuity. This means that in the last part of the atomizer (nozzle), the pressure close to the atomizer's axis decreases, leading to increase the air-core diameter. The movement of the gas can be approximated to a solid body rotation, with $u_{swirl} \propto r$. A similar behaviour can be found in the liquid close to the liquid-gas interface and it continues up-to the transition with the free vortex region: at high Re a sharp peak on the tangential velocity profile can be found as transitional region (Hsieh and Rajamani [34]), while at low Re the tangential velocity profile displays a smooth, rounded, peak (Horvay and Leuckel [32][33] and Hsieh and Rajamani [34]).
If the low viscosity assumption is released, the axial velocity component is no more constant over the radius $\partial u_a/\partial r \neq 0$ (for example boundary layer effect).
Chinn [6] evaluated the effect of the surface tension on the liquid interface using the same approach used to evaluate the equilibrium of a water droplet. The surface tension per unit length in the $\theta - r$ plane is equal to 2σ, where σ represents the surface tension per unit length. This force must be balanced by the differential pressure force across the surface boundary ΔP_σ, acting on the air-core diameter:

$$2\sigma = \Delta P_\sigma d_{ac} = \Delta P_\sigma 2 r_{ac} \Rightarrow \Delta P_\sigma = \frac{\sigma}{r_{ac}} \tag{2.6}$$

where r_{ac} is the air-core radius. This means that the surface tension has a stronger effect on the air-core size in the smaller atomizer. However, the common operating conditions of small scale PSAs, yield to have a differential pressure on the interface always much higher than the value of ΔP_σ: this means that the surface tension effect becomes minimal, and then it can be neglected.

2.3 Nature of the internal flow field

For the previous simplified analysis, the flow has been considered laminar, but the complexity of this flow does not lead to clearly understand its real nature. The investigation can be simplified considering the inlet channel and then the swirl chamber, with the relative definition of the Reynolds number to investigate it. Some authors like Madsen et al. [50] defined the Reynolds number of the flow within the inlet channels, which is the same of a simple tube and it is equal to:

$$Re_i = \frac{\rho_l d_{Hi} U_i}{\mu_l} \tag{2.7}$$

where d_{Hi} is the hydraulic diameter and U_i the characteristic velocity of the liquid within the inlet channels. If Re_i is lower than 2300 the flow can be considered laminar, while for valuer higher than 3000 the flow is fully turbulent. In the range in between these two values, the transition regime occurs. With a turbulent inflow, the following analysis on the atomizer internal flow must takes into account the turbulence, due to the fact that at least in the inlet region it is present. Moving downstream, the flow can return to be laminar, due to the centrifugal forces acting on it which induce a stabilizing effect. Indeed, the tangential velocity component is the greater velocity components (higher 5 times than the axial velocity component), and therefore it must be considered to evaluate the nature of the internal nozzle flow. The effect of the strong tangential velocity gradient across the radial direction, yields to oppose to the velocity fluctuations induced by turbulence phenomena, and therefore the flow becomes more stable and consequentially laminar.
This phenomenon can be explained considering a liquid particle p with mass m_p, which is moving with a tangential velocity $u_{swirl,p}$ along the circumference with initial radius r_p; the corresponding centrifugal force is equal to $F_c = m_p u_{swirl}^2 / r_p$, which is in equilibrium with the negative differential pressure gradient along the radius F_p. If due to the turbulent fluctuation, the particle p tries to move inward at the position $r_{p,in} = r_p - dr$, the centrifugal force increases, due to the decreasing of the radius ($u_{swirl,p}$ remains

constant); therefore, due to non-equilibrium between the forces acting on the particle ($F_c > F_p$), it is forced outward upto its initial radial position r_p. Conversely, if the turbulent fluctuation leads the particle to move outward at the position $r_{p,out} = r_p + dr$, the centrifugal forces decreases, due to the increment of the radial position. As for the previous case, there is a non-equilibrium condition where $F_c < F_p$ and therefore the liquid particle is forced inward upto its initial radial position r_p, where the equilibrium condition is reached. From this simple analysis, the net effect of these opposing forces is to inhibit turbulent motion and it is likely that for smaller atomizer, the flow within them remains wholly laminar.

The "inhibition" of the turbulence effect explained above is the principal effect that must be considered to properly set up the simulation of the internal nozzle flow to investigate its behaviour and its nature. Radcliffe [61] defined that the emerging jet from a pressure swirl atomizer, can be assumed inviscid, if the Reynolds number Re_o, defined at the exit section of the atomizer, as reported in Eq. 2.8, is higher than 3000.

$$Re_o = \frac{d_o u_o \rho_l}{\mu_l} \tag{2.8}$$

In Eq. 2.8, u_o represents the liquid axial velocity at the exit section of the atomizer, defined as:

$$u_o = \frac{4\dot{m}_l}{\pi d_o^2 \rho_l} \tag{2.9}$$

Walzel [89], in a more recent investigations, defined a Reynolds number based on the potential velocity evaluated considering the pressure drop the PSA, and the outlet section diameter d_o:

$$Re_W = \frac{\sqrt{2\rho_l \Delta P} d_o}{\mu_l} \tag{2.10}$$

As Walzel [89] pointed out, if Re_W is higher than 5000, the flow can be assumed fully turbulent, otherwise the laminar, and the eventually transitional region, can be found within the atomizer.

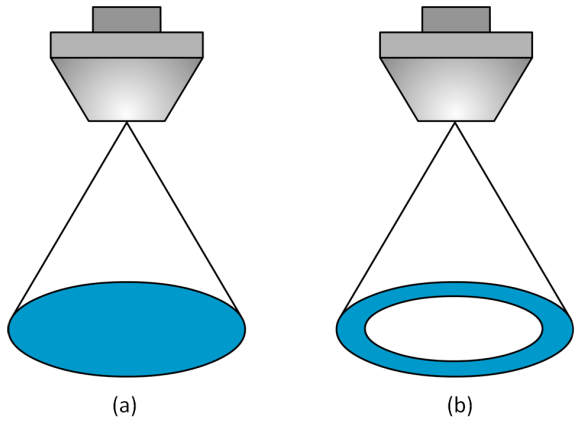

Figure 2.5: Spray produced by PSA: (a) solid cone; (b) hollow cone.

2.4 Jet production

Pressure swirl atomizer can produce a spray which can be a $solid - cone$ or a $hollow - cone$. For the first one, the droplets produced after the break-up of the jet, are distributed fairly uniformly throughout its volume. For the $hollow - cone$ spray the most of the droplets are concentrated at the outer edge of the conical spray pattern (see Figure 2.5). The solid-cone spray has a coarser atomisation if compared with the $hollow - cone$, due to the presence of large droplets in the internal region. Therefore, due to the better atomisation and the radial droplets position, the hollow-cone spray are preferred for many industrial purposes, especially for combustion applications.

The atomizer shown in Figure 2.1 is the simplest form of hollow-cone atomizers, and it is called *simplex*. In this study, only the $hollow - cone$ atomizer are investigated.

PSA has five different stages of work, depending on the injection pressure of the liquid (see Figure 2.6):

1. liquid dribbles from the orifice;
2. liquid leaves as a thin distorted pencil;
3. a cone forms at the orifice but it is contracted by surface tension forces into a closed bubble
4. the bubble opens into a hollow tulip shape terminating in a ragged edge, where the liquid disintegrates into fairly large drops;
5. the curved surface straightens to form a conical sheet; as the sheet expands its thickness diminishes, and it soon becomes unstable and disintegrates into ligaments and then into droplets in the form of a well defined *hollow − cone* spray.

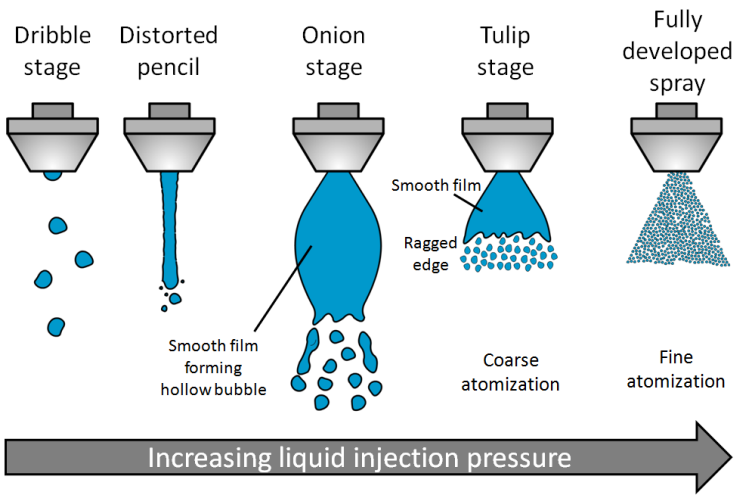

Figure 2.6: Stages in spray development with increase in liquid injection pressure.

The major drawback of the PSA is that the flow rate varies as the square root of the pressure drop across the atomizer: this means that to

doubling the flow rate demands the injection pressure must be increased four times. This link between the mass flow rate and the feeding pressure, limits the operating conditions range. However if the atomizer discharge orifice is made small enough to ensure good atomisation at low fuel flow rates, then the pressure required at high flows becomes excessive (small flow number FN). This means that low energy and flow rates are required to have a good atomization. On the other hand, if the orifice is enlarged, the fuel will not atomize satisfactorily at the low flow rates and low pressures, and consequentially the mass flow rate must be increased to have a fine spray. This condition is commonly researched for the aircraft engines, which operate at high altitudes and require high flow rate to work properly (large flow number). This limit of the simplex atomizer leads to develop various wide-range atomizers, such as duplex which incorporates two swirl chamber: one (the pilot) is located concentrically within the other (the main).

2.5 Break-up of the conical liquid sheet

For a conical swirled jet, three different basic modes of sheet disintegration has been found by Fraser and Eisenklam [20]: rim, wave and perforated sheet.
As reported by Chinn [6], the rim mode has been found for the jet where the liquid has high viscosity and surface tension. The latter one leads the liquid to contract into a thick rim. This further reduces droplets production, which continue to move in their original direction but remain attached to the sheet by thin threads. Both the droplets and the threads continue to break-up under the action of different forces and phenomena (secondary break-up), to the final spray.

With the wave break-up mode, the liquid sheet undergoes oscillations that are likely to be induced by the opposing surface tension and aerodynamic forces. Near the crest, the relative velocity between the liquid and the gas is high, and thus the local pressure is low. Under this condition, the surface of the liquid behaves as an aerofoil and it is drawn away from

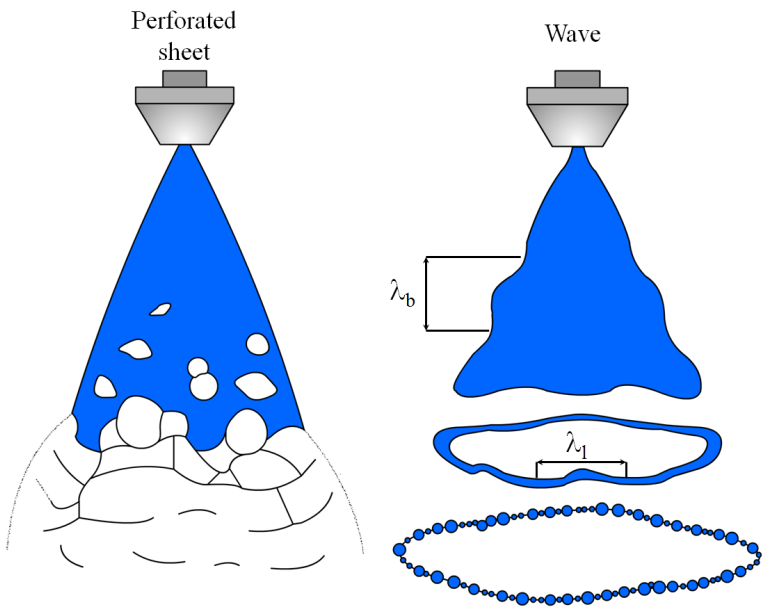

Figure 2.7: Conical swirled jet break-up.

the conical sheet. The surface tension forces are opposed to the aerodynamic ones, and it leads to contract the protuberance, that is the wave (with wavelength λ_b), back into the sheet.

There are two different wave modes that can develop over the sheet surface and they are called symmetric and anti-symmetric mode, as shown in Figure 2.8. The first is also called dilatational or varicose mode, and the wave moving on the top surface is in opposing phase with the bottom wave. Conversely for anti-symmetric mode, or sinuous mode, both the waves moving on the top and the bottom surface are in phase. For the varicose mode, the sheet thickness varies periodically as series of contractions and dilatations. For both the modes, the wavy sheet breaks-up into ligaments and then into droplets.

At least, in the perforated sheet break-up mode, holes appear under

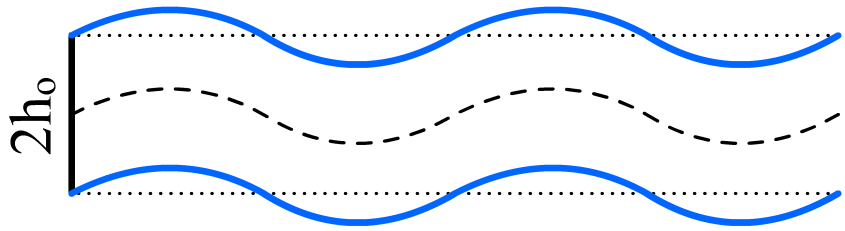

(a) Sinuous mode

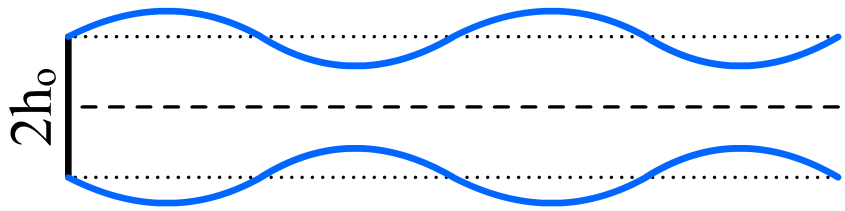

(b) Varicose mode

Figure 2.8: Schematic of (a) antisymmetric or sinuous wave and (b) symmetric of varicose waves.

the action of surface tension. As consequence, the liquid threads around the holes contract, as the holes enlarge, to form a net of irregular liquid ligaments.

According to the Bayvel and Orzechowski [2] the perforated sheet is present at low liquid velocity, conversely the wave mechanism dominates at high velocity. For higher liquid velocity, Bayvel and Orzechowski [2] found a disintegration mechanism: under this operating condition, the short wave lengths have an amplitude that increases rapidly and leads to an earlier break-up of the liquid lamella. Consequentially the break-up length L_b decreases and becomes so small that the liquid sheet cannot be seen. At very high Re, the flow can be turbulent and its effect on the break-up process is still not clearly understood, however according to Widger [91], it may lead to a wider spread of droplets size distribution.

Chapter 3

State of the art

3.1 Internal nozzle flow

The jet and the sub-sequent spray formation depend on the structure of the liquid at the exit section of the atomizer: therefore investigations on the internal nozzle flow help to better understand the jet behaviour.
A simple description of the internal flow can be done using the inviscid theory, adopting correlations depending on the liquid properties, operating conditions and atomizer geometry. Although these correlations can predict the performances of the atomizer in a easy way, the high number of suitable configurations do not allow to have an universal law able to describe the internal nozzle flow and the main parameters for all of them. Therefore, further investigations, made with experiments and/or numerical simulations, must be done for every specific case, in such a way to properly define the behaviour of the PSA. Experiments are very difficult to perform: the atomizer scales can influence its performances, and for the combustion system, PSAs assumes very small dimension. In this case the common experimental techniques (photographic or laser) can't be adopted and limit the investigation cases only for a large scale atomizer. The current computational facilities allow to perform numerical simulation of the internal nozzle flow, able to

track the liquid position, its velocity and pressure field, together with the gas properties (air-core). Although, with this tool, the internal nozzle flow can be investigated, the swirl motion over a concave surface induces a limit to some of the turbulence model that can be adopted.
In this section a review on the main work made in the past on the experiments and numerical investigations within the atomizer will be presented. To get more information about the 1D inviscid model of the internal nozzle behaviour see Chinn [6].
To have a complete overview of the internal nozzle flow, see Yule and Widger [96].

3.1.1 Air-core development

One of the main aspect that characterizes the emerging flow from pressure swirl atomizer is the presence of the air core, and consequentially the opening of the jet. Section 2.4 already reports the jet stages at different injection pressure: the variation from one stage to another strictly depends from the atomizer geometry and the liquid properties. Different authors try to define the atomization stages adopting non-dimensional numbers as the Reynolds number. One of the first investigation on the air-core development has been made by Horvay and Leuckel [32][33], whom investigated the internal nozzle flow with LDA measurements. To allow the optical access for the laser beam, the investigated atomizers is made with transparent plexiglass (perspex). Three different geometries have been used to investigate the influence of the atomizer geometry on the behaviour of the flow within the atomizer: the first has a conical section which links the injection region with the final nozzle of the atomizer (nozzle 1); the second has a trumpet-shaped convergence section (nozzle 2) and the last one has no convergence section (nozzle 3). Four tangential inlets, normal to the main axis of the injector, are adopted with two different configurations: both have apertures of 20 mm along the axial direction while along the radial direction the first is 10 mm wide while the second is 5 mm wide. Thin walls have been adopted to reduce the refraction caused by the perspex. The liquid used in these experiments have been adapted to have the same refractive index

of perspex to not affected the laser beam trajectories, and it is a mixture of tetrahydronaphtaline (tetraline), turpentine and castor oil. By varying the quantities of each components listed before, the experiments have been made over a range of viscosities, and hence a range of Reynolds numbers. A fluid-dynamic similitude made with the adopted mixture leads to use a scaled-up version of these atomizers which are commonly fed with water. Measurements of the axial and tangential velocities were taken along the radius at different cross-sections through the atomizers, at the axial distance of the exit section of 10 (inside the nozzle), 30, 40, 50, 60 and 70 mm (inside the converging section).
The seeding particles, needed to scatter the laser light, were small bubbles which were entrained at the intake pump that supplied the operating liquid inside the experimental rig. Due to the high radial pressure gradient, the bubbles density change along the radius (high close to the wall and low close to the free surface of the air-core). This phenomenon does not allow to perform a correct measurement of the radial velocity, therefore only the axial and the tangential velocity components could be measured using the LDA system.

One mass flow rate has been investigated, while the liquid viscosity has been changed to evaluate different Reynolds number, defined as follows:

$$Re_{HL} = \frac{\overline{w_i}(r_m)\rho_l}{\mu_l} \tag{3.1}$$

where $\overline{w_i}$ represents the normalised inlet velocity, which definition is reported in Eq. 3.3. Three different cases have been investigated over the atomizer with conical convergent section (nozzle 1): two with the larger inlet channel configuration and one with the smaller configuration. Consequentially, for the first two cases, $\overline{w_i} = 0.3125 m/s$, while for the second is equal to 0.625 m/s. The liquid viscosity μ_l has been set equal to 25 kPa for the first case, while for the other two cases it has been set equal to 1.6 kPa. The resulting values of Re_{HL} for the investigated cases are equal to 1125, 18018 and 38037.

Horvay and Leuckel [32] defined the swirl number S_{HL} as follows:

$$S_{HL} = \frac{Q_l \rho_l \overline{w_i} r_m}{Q \rho_l u_o r_o} \tag{3.2}$$

where Q_l represents the volumetric flow rate. The inlet tangential velocity w_i and the axial velocity at the exit section of the atomizer u_o can be replaced with the following relations:

$$u_o = \frac{Q_l}{\pi r_o^2} \quad \overline{w_i} = \frac{Q_l}{A_i} \tag{3.3}$$

therefore, considering the previous relations, the swirl number defined by Horvay and Leuckel in Eq. 3.2 becomes:

$$S_{HL} = \frac{\pi r_m r_o}{A_i} \tag{3.4}$$

For the first two investigated cases with the large inlet channels configurations, the value of S_{HL} is equal to 1.767, while for the last case with the small inlet channels configurations it is equal to 3.737.

From the experiments it was observed that only for the cases with higher Re_{HL} the air-core is present and it reaches the top wall of the swirl chamber, while for the first case with the lowest investigated Reynolds number, the air-core height l_{ac} does not pass the 10 mm ($l_{ac}/l_o = 0.5$). The cases at higher Reynolds number a small increment of the air-core diameter can be seen at all the investigated measurement height: De Keukelaere [9] found that the air-core diameter should asymptote to a finite size for a given atomizer design, as the Reynolds number increase. This is connected to the limit imposed by the volumetric flow rate which must be guarantee at the nozzle exit section.
For the nozzle No. 2 and No. 3 (trumpet-shaped convergence section and no convergence section) the experiments have been made with the large inlet channel configuration, and with $Re_{HL} = 1125$. The results show that the air-core is not present for atomizer with nozzle No. 3, while it is present

over the total height of the atomizer for the atomizer configuration with nozzle No. 2. Horvay and Leuckel [32] comment that since the formation of the air-core need a certain minimum local swirl intensity, which cannot be reached with nozzle No. 3 where the strong cross-sectional variation over the atomizer axis induce a strong decrement of the swirl strength. The authors conclude that the convex convergence atomizer geometry causes the lowest swirl losses and it may represents the optimum atomizer configuration (nozzle No. 1).

Lee et al. [47] performed experiment on a large scale PSA made by transparent acrylic-based material to evaluate the formation of the air-core for different values of Re_{WL} (see Eq. 2.10). The investigated atomizer is composed by a single tangential inlet, which leads to have less strength of the swirl motion if compared with a similar multi-port swirl atomizer. Diesel and Bunker-A fuels have been adopted to evaluate the effect of the liquid viscosity and surface tension on the air-core development. The injection pressure has been increased from the initial value of 3 bar up to 9 bar. At low injection pressure the presence of the air-core has not been observed and a solid cone jet is produced. In this unstable regime, turbulence likely interrupts the helical flow in the swirl chamber. The air-core starts to be present at $\Delta P = 5$ bar, where the air-core diameter and height are not stable (unstable regime), together with the static pressure measurement at the internal atomizer wall. At the injection pressure of 9 bar, the air-core reaches the top wall of the swirl chamber, and the atomization quality is optimal. Considering the Reynolds number (Re_{WL}), five different operating stages have been identified for diesel fuel, considering the normalized air-core height l_{ac}/l_c (where $l_c = ls + l_{s,c} + l_o$ as shown in Figure 2.1) :

(A) $Re_{WL} < 2450$ the flow is unstable and there is no presence of the air-core inside the atomizer;

(B) $2450 \leq Re_{WL} < 3000$ the air-core starts to be present from Re_{WL} equal to 2550, and in this transitional regime l_a/l_c varying between 0.10 and 0.35;

(C) $3000 \leq Re_{WL} < 3300$ in this region the flow reach a relatively stable

state where l_a/l_c is close to 0.38;

(D) $3300 \leq Re_{WL} < 3450$ a minor fluctuations have been observed, where l_{ac}/l_c changes from 0.38 to 0.42;

(E) $Re_{WL} \geq 3450$ the normalized height jump directly from 0.42 to 1.00, and a completely stability region is reached.

Lee et al. [47] pointed out that the stable region is reached when the normalized eight l_{ac}/l_c of the air-core exceeds the the normalized height of the nozzle exit l_o/l_c. In the swirl chamber, the air-core is more stable than in the contracted/laminarized region, due to a strong swirl motion linked to the larger chamber diameter. No data are available for the Bunker-A fuel due to its opacity which does not allow to properly evaluate the air-core development.

3.1.2 Liquid lamella thickness $2h$ and discharge coefficient C_d

Other important parameters adopted to characterize the pressure swirl performances are the liquid film thickness evaluated at the exit section of the atomizer $2h$, and the discharge coefficient C_d, which both depend on the air-core size. In literature several works aimed to define these two parameters changing the operating conditions and the atomizer geometries can be found, and here a small group of them will be presented.
In Appendix A, a collection of the semi empirical correlations for the prediction of the liquid lamella thickness $2h$ and the discharge coefficient C_d have been reported.

Lamella thickness $2h$

One of the first experimental investigation on the evaluation of the liquid film thickness has been made by Kutty et al. [43], whom measured the air-core diameter by CCD camera located under the atomizer in such a

way to see what happens inside the atomizers. Their experimental data have been adopted from other authors to developed their analysis. The subsequent important work has been made by Horvay and Leuckel [32], which experimental setup has been explained in the previous section (section 3.1.1). The air-core radius evaluated at the exit section $r_{o,ac}$ has been measured, and consequentially the liquid film thickness can be defined as $2h = r_o - r_{o,ac}$, and the results are reported in Table 3.1: as it can be seen, if Re_{HL} is increased (together with S_0), the value of the normalized liquid lamella thickness decrease (up to 29%), although from LDA measurements both the cases seem to be fully developed and with similar velocity flow field. From the photographic and LDA experiments, a correlation to predict the air-core diameter $2r_{o,ac}$ has been developed:

$$\frac{X^*}{X} = 1 - e^{(-0.04 Re_{HL}^{0.35})} \tag{3.5}$$

where X^* is the corrected value of the normalized air-radius equal to $r_{o,ac}^{*2}/r_o^2$, while X is the theoretical inviscid normalised air-core radius shown in Eq. 3.8, which is obtained from the value of the swirl number defined in Eq. 3.4:

$$S_0 = \sqrt{\frac{2X^2}{(1-X)^3}} \tag{3.6}$$

Horvay and Leuckel [33] accredit this formulation to Söhngen and Grigull [78], and it is similar to equation A.14 of Giffen and Muraszew [24], reported in Appendix A, where the value of S_0 is replaced with another atomizer constant.

Another important contribute on the prediction of the liquid lamella thickness has been done by Lefebvre, in several works and in collaboration with Rizk N. K. [68][66][70] and Suyari M. [82]. Rizk and Lefebvre [68][66][70] adopted the experimental data provided by Kutty et al. [43] in a precedent work. In the works of Rizk and Lefebvre [68] it is shown the effect of the individual swirl atomizer geometrical dimensions (r_o, r_i, r_s, l_o

Convergent geometry	S_0	Re_{HL}	$2h/r_o$
Conical (nozzle 1)	1.767	18018	0.42
	3.737	38037	0.30
Trumpet-shaped (nozzle 3)	1.767	1125	0.58

Table 3.1: Inlet velocity components for each phase.

and l_s) and the variation of the liquid fluid properties (μ_l and ρ_l) on the atomizer performances, obtaining the following simplified formula:

$$2h = \frac{1560\dot{m}_l\mu_l}{\rho_l d_o \Delta P}\frac{(1+X)}{(1-X)^2} = \frac{1560FN\mu_l}{\rho_l^{0.5} d_o \Delta P^{0.5}}\frac{(1+X)}{(1-X)^2} \tag{3.7}$$

where FN is the flow number and X is the ratio of the air-core area over the total outlet area:

$$X = \frac{A_{o,ac}}{A_o} = \frac{r_{o,ac}^2}{r_o^2} = \frac{(d_o - 4h)^2}{d_o^2} \tag{3.8}$$

As it can be seen in Eq. 3.7, the value of the lamella thickness depends on the atomizer dimension (d_o), the operating conditions (ΔP and $\dot{m}_l$) and the liquid properties ρ_l and μ_l). The importance of the viscosity is clear in this equation, and it shows the effect of the frictional forces present inside the atomizer. In a subsequent publication, Rizk and Lefebvre[70] simplified the previous correlation, only if $2h/d_o << 1$, obtaining the following expression:

$$2h = 3.66\left[\frac{d_o FN\mu_l}{\Delta P \rho_l}\right]^{0.25} \tag{3.9}$$

For both these correlations, it can be found that:

- for a given atomizer, increasing the inlet pressure (increasing the ΔP) the value of $2h$ decreases up to reach a constant value for a very high injection pressure;
- $2h$ increases with atomizer outlet diameter d_o;

- $2h$ increases with atomizer inlet diameter d_i, because an increment of the inlet area yields to increase the flow rate, and therefore, for a given outlet cross-sectional area, the film thickness must increase;
- $2h$ increases when the swirl chamber diameter d_s decreases, because the connected strength of the swirling action decreases, producing a smaller air-core;
- $2h$ slightly decreases when l_o increases (approximately 7% for the tested length);
- $2h$ slightly increases with l_s (approximately 8% for the tested length);
- for a given atomizer, $2h$ slightly increases with the liquid kinematic viscosity μ_l;
- for a given atomizer, $2h$ slightly decreases with the liquid density ρ_l.

In a subsequent work of Suyari and Lefebvre [82], Eq. 3.9 has been modified to better fit the performed experimental data. Indeed, from the Kutty et al. [43] experiments, the maximum values of $2h$ have been extracted at the exit section, as consequence of the photographic measurements. In their experiments, Suyari and Lefebvre [82] defined the value of the liquid lamella thickness at the exit section of the atomizer by using a conductance method, able to measure all the ripples and to provide at the end the averaged value. With this correction, only the constant coefficient of Eq. 3.10 is changed from 3.66 to 2.7, obtaining the following expression:

$$2h = 2.7 \left[\frac{d_o F N \mu_l}{\Delta P \rho_l} \right]^{0.25} \tag{3.10}$$

Discharge coefficient C_d

The discharge coefficient allows to define the conversion of the potential flow energy, with the effective axial kinetic energy at the atomizer outlet section, ad it can be defined as follows:

$$C_d = \frac{\dot{m}_l}{A_o\sqrt{2\rho_l \Delta P}} \tag{3.11}$$

When the atomization regime is reached, the mass flow rate is proportional to the square root of the injection flow rate ($\dot{m}_l \propto \sqrt{\Delta P}$), therefore the discharge coefficient must remain almost constant. This result has been proved by Radcliffe [61], who defined that for values of $Re_o > 3000$, the flow can be considered inviscid, and under this condition the value of C_d becomes constant and does not depend on Re_o.

Dombrowsky and Hasson [11] performed experiments to define the atomizer geometry effect on C_d. The effects of the variations in the dimensions of the atomizer have been correlated using three dimensionless groups; the atomizer constant K (see Eq. A.3), the length to diameter ratio at the outlet section l_o/d_o and the ratio of the distance between the center inlet area with the main axis (r_m) to the outlet radius r_m/r_o. The final results show that:

- C_d increases with K;
- C_d increases with r_m/r_o;
- C_d decrease when l_o/r_o increase.

The latter point shows the importance of the viscous losses present in the last part of the atomizer.

The liquid viscosity effect on the discharge coefficient has been investigated by Rizk and Lefebvre [68], whom stated that increasing the liquid viscosity, for a fixed geometry and operating condition, increases the frictional losses for the swirl velocity component, and not for the axial one, which is maintained constant by continuity. The swirl strength reduction yields to have an increment of the liquid lamella thickness, and consequentially to increase C_d. The discharge coefficient reaches the maximum value when the swirl strength is not enough to ensure the presence of the air-core, and therefore the outlet section of the atomizer is fully occupied by the liquid. Further increasing of the liquid viscosity yields to increase the frictional

losses along all the atomizer, considering also the axial velocity component that induces C_d to decrease. Rizk and Lefebvre [68] also pointed out that if the value of the atomizer constant K is kept fixed, while the atomizer scale is reduced, the peak of C_d occurs at lower viscosity.

Lee et al. [47] defined the variation of the discharge coefficient with Re_{WL}, as they have been done for the air-core investigation, reported here in section 3.1.1. Due to the higher viscosity of the Bunker-A fuel, the values of C_d is lower than the results obtained with the Diesel fuel. However, for both fuels the discharge coefficient changes as follows:

(A) the liquid is present in the whole outlet section, increasing the mass flow rate, and obtaining at the end an high value of C_d;

(B)-(D) the air-core starts to be present and then the discharge coefficient decreases ($2450 < Re_{WL} < 3450$ for Diesel and $2400 < Re_{WL} < 3300$ for Bunker-A);

(E) when the flow reaches the stable regime, C_d becomes insensitive to Re_{WL} variation.

A similar discharge coefficient variation has been observed by Park et al. [59] on kerosene experiments.

3.1.3 Internal flow field

The internal flow field investigation can be conducted with both experiments and numerical simulation. The first commonly can be done over a large scale atomizer, to allow the optical access for the laser velocity measures, or to evaluate the turbulence level and air-core shape; the numerical simulations require a correct set-up which must take into account the effect of the swirl motion: indeed the turbulence model adopted can yield to different results in terms of internal nozzle flow and also in terms of macroscopic parameter as the air-core and the liquid lamella thickness, and consequentially on the C_d. A small discussion on the turbulence model is reported in section 3.1.6.

One of the first internal nozzle flow investigation has been made by Horvay and Leuckel [32], for different atomizer geometry (different K and S_0) and different Re_{HL} as shown in Eq. 3.1 (more details are reported in section 3.1.1). Horvay and Leuckel [32] found that for the case with the lowest Re_{HL}, the tangential velocity profiles are similar to a Rankine combined vortex with a solid body behaviour in the center of a potential vortex distribution ($w_i \propto r$) and a vortex distribution in the outer region ($w_i \propto 1/r$). This behaviour has not been observed in the other two cases with higher Re_{HL}, where the solid body region is close to the air-core, and therefore it has not been detected by LDA measurements (high level of signal noise). The boundary layer can be observed in the velocity profiles extracted for the first case ($Re_{HL} = 1125$), while for the other cases it becomes too small to be measured with the LDA techniques.
The axial velocity profile over the radius for the case at low Re_{HL} has lower values in the wall proximity than close to the main flow body, where it appears to be negligible. Consequentially the greatest volume flow takes place near to the central axis. The latter result is not in accord with the theory of Taylor [83], who found by a mathematical boundary layer analysis within a conical convergence section that the axial flow must be localized within the boundary layer adjacent to the atomizer wall. Horvay and Leuckel [33] performed numerical simulations with which they compare their experimental results with the Taylor theory [83], showing that in correspondence of the inlet, the entering liquid is divided into two different flows: one continue adjacent to the wall of the swirl chamber (as suggested by Taylor), while the second one moves radially inward along the top wall of the swirl chamber and then forced in the axial direction once it reached the atomizer axis (or the air-core interface if it is present). The same behaviour has been also observed experimentally by Donjat et al. [13] by LDV and PIV measurements on another PSA.
For the cases at the $Re_{HL} = 18018$ and $Re_{HL} = 38037$ no high values of axial velocity have been found close to wall and Horvay and Leuckel [32] suggested that is connected to the thinning of the boundary layer due to higher liquid swirl strength motion.
Measurements made by Horvay and Leuckel [32] report the velocity pro-

files through the rectangular inlets for different Reynolds numbers: for all the investigated cases, the normalized tangential velocity $w_i/\overline{w_i}$ reaches the same maximum value equals to 1.3. This increment of the velocity at the inlet proximity is connected to the development of the boundary layer at the external wall of the atomizer, which yields to decrease the effective inlet cross sectional area; moreover, the inlet flow is influenced by the swirling flow already present within the swirl chamber, and this can justify the different flow behaviour by changing the Re_{HL} within the atomizer (close to the atomizer axis). For the case with lowest investigated Re_{HL}, the parabolic profile has been identified at the inlet proximity; then the tangential velocity assumes values below the average inlet tangential velocity $\overline{w_i}$, prior to taking up the free vortex profile. For the higher Re_{HL}, the classical Rankine combined vortex has been observed: a free vortex leading, linked through a transition zone, to a solid body rotation.

De Keukelaere et al. [9] conducted an experimental analysis on a large perspex atomizer. The static pressure at the wall has been measure over the atomizer wall along the axial direction; in addition, a video system has been adopted to record the air-core developments within the atomizer and then measure it in the subsequent post-process stage. The gauge injection pressure has been changed between 15 kPa, which is the first operating condition at which the air-core was almost fully formed, and 60 kPa. The temperature of the liquid (water) has been controlled to keep constant all the properties of the liquid ($T_l = 18.7 \pm 0.4C$). The resulting flow rate at the pressure drop indicated before are $0.205 \times 10^{-3} m^3/s$ and $0.389 \times 10^{-3} m^3/s$, and the corresponding value of the Reynolds numbers, defined in Eq. 3.1 are 27400 and 51900.

The measurements of the static pressure at the atomizer walls, shows that the pressure changes accordingly with the different atomizer shape:

Swirl chamber in this region, the values of the static pressure remain stable and constant over the all length (high pressure);

Convergent section due to the area contraction, the axial velocity increases to respect the mass conservation, and consequentially the static pressure decreases (pressure drop);

Nozzle in the last part the pressure reaches a new stable and constant values, which decreases rapidly to ambient gas pressure in correspondence of the outlet section (low value).

Combining the Bernoulli equation with the pressure measurements and the video of the internal flow field, the air-core development has been characterized. Into the swirl chamber, which has a constant geometry (constant diameter d_s), the pressure remains also constant as the air-core diameter, which can be measured from the video. In the conical convergent section the flow accelerates to balance the mass flow rate, inducing the pressure to decrease: in this atomizer section the radial position where the gauge pressure inside the liquid reach the ambient value, i.e. zero, moves outward and consequentially the air-core increases in diameter. Close to the outlet section, the gauge pressure decreases rapidly to zero (the liquid pressure is equal to the ambient value): this result leads to a rapid increment of the air-core diameter. De Keukelaere [9] reported that the same behaviour has been observed from different authors in the past as by Ebbesen [17], Giffen and Massey[23], Mani et. al.[52] and Lawrence[46]. Ebbesen[17] also suggested that the air-core size rises linearly with increasing pressure.

Donjat et al. [13] performed LDA and PIV measurements on a perispex atomizer with a classical geometry and four tangential inlet channels. Together with these kinds of experiments, LIF images have been taken to better understand what happens inside the large scale prototype PSA. The liquid adopted was water. From LIF images of lateral view of the swirl chamber zone, large turbulent structure can be found, which is produced from the interaction of the liquid entering inside the swirl chamber and the swirl chamber walls; these structures are then diffused towards the air-core. These vortices show a strong diffusion of the jet momentum coming from the inlet channels, and their frequency depends on the inlet Weber number We_i and the local velocity gradients. Far from the wall boundary layer region, these turbulent structures are captured and then broken up by the intense tangential velocity field. At the air-core proximity, the LIF images show an increment of the swirl velocity, which evidences the second main stream in this region.

For the axial velocity measurements, the same behaviour obtained from Horvay and Leuckel [33] numerical simulations, and the radial velocity component measurements at the top wall of the swirl chamber confirm that a flow which feeds the air-core streams is present: due to the inlet channels, the liquid is forced to move along the radial direction to the air-core where it is then forced axially, assuming the classical structure of a confined vortex as described by Escudier et al. [18]. PIV measurements confirmed the previous LDA data and reveals a complex secondary flow between the swirl chamber walls and the air-core: here a large number of small scale vortices transfer the flow rate from the wall to the air-core and dissipate the kinetic energy of the inlet flow.
Donjat et al. [13] evaluated the Re_{WL} as defined in Eq. 2.10, and for all the investigated cases it covers the range between 13000 to 150000, which yields to consider the flow turbulent: this result is confirmed from LDA measurements, where fairly large oscillation has been detected and linked to a turbulent source, confirming the turbulent nature of the flow.

3.1.4 Air-core fluctuations

Different waves over the air-core interface have been detected, which propagate over the initial conical jet after its injection. From the photographic experiments, De Keukelaere et al.[9] observed a fluctuations of the air-core (also reported by Rajamani[34] for similar case of hydrocyclone separator) which are not linked to turbulence fluctuations, due to the fact that no experimental measurements of the liquid velocity have been performed and the flow has been considered laminar. Small sinuous wave-like osculation has been observed over the air-core surface by De Keukelaere et al.[9] (also observed by Kong[40]) as "travelling ripples". The same fluctuation has been observed from the pressure measurements in this section of the atomizer, but not in the other region, where the flow appears steady.

From the high speed camera visualization performed by Donjat et al. [13], the air core instabilities can be investigated. Precession and helical modes have been identified which movement extended to the conical jet. On the latter one, capillary waves have been detected. The first mode has

a frequency of 10 Hz, while the second has a frequency of 300 Hz. These frequencies increase linearly with the flow rate. Inside the convergent and exit part of PSA, these frequencies increase due to the acceleration of the liquid. However, the same spectrum has been found in the air-core within the swirl chamber, and on the final conical swirled jet. In a subsequent work, Donjat et al. [14] defined a Strouhal number (see Eq. 3.12) as a function of the atomizer characteristics, for both the identified frequencies:

$$St = \frac{f\,(d_s - d_i)}{\overline{w_i}} \tag{3.12}$$

From Donjat et al.[14] experiments made on different values of K (see Eq. A.3) and d_o/d_s, they found the following relation for the lower frequency (precession mode):

$$St_1 = 2.1K^{0.48}\left(\frac{d_o}{d_s - d_i}\right)^{0.5}\left(\frac{d_s}{d_s - d_i}\right)^{-2.63} \tag{3.13}$$

Eq. 3.13 shows that the frequency of the precession mode increases with K and it reaches a constant value; St_1 also depends from the inlet slots dimension and of their position in relation with the swirl chamber. In Eq. 3.14 the Strouhal number of the higher frequency (helical mode) is reported, which still depends on the value of K and especially the exit orifice dimension, since d_o/d_s leads the swirl velocity of the internal flow.

$$St_2 = 1.14K^{0.72}\left(\frac{d_o}{d_s - d_i}\right)^{-1.82} \tag{3.14}$$

3.1.5 PSA design

The geometry of the atomizer must be generated such as to increase the atomization performance and to minimize the pressure losses. Dombrowsky and Hasson [11] are the first who try to define the properly atomizer dimension to reach this goal, starting from the inlet channels, which ratio

l_i/r_i must be sufficiently large to ensure that the liquid enters into the swirl chamber with the desired tangential velocity, but not so large to not introduce excessive frictional losses, as also pointed out by De Keukelaere et al. [9]. Therefore, an optimum value of this ratio has been found by Dombrowsky and Hasson [11], which corresponds to $l_i/r_i = 3$.
In a successive work, De Keukelaere et al. [9] showed the importance of the axial distance between the inlets from and the top wall of the swirl chamber. Indeed it influences the energy losses of the inlet flow: if the top walls of the inlet channels coincide with the top wall of the swirl chamber (as for the Horvay and Leuckel[32][33] and for De Keukelaere [9] experiments), the top boundary layer must be taken into account, which decreases further the real inlet cross-section area and then increases the pressure drop; if the inlet channels are positioned far from the top wall of the swirl chamber, there is a recirculating region which reduces the pressure energy available for atomization. Therefore De Keukelaere[9] concluded that for an optimum design of PSA, a correct distance of the inlet channels to the top wall of the pressure swirl must defined to reduce the energy losses.

Further recent investigation on the atomizer design has been developed by Yule and Widger [96], Jeng et al. [38], Halder et al. [26] and Sakman et al. [72], .

3.1.6 Turbulence model investigation

The internal nozzle flow can be investigated with numerical tools, as it has been done by several authors like Horvay and Leuckel[33], Yule and Chinn[95][7], Nonnenmacher and Piesche[57], Datta and Som [8], Hansen et al. [28], Madsen et al. [50] and Sumer et al. [81]. The main issue that must be solved is connected to the turbulence model adopted to describe the flow. In several works the internal flow has been considered laminar [95][7][57][8], but often this condition is not reached. Indeed if the flow has been expected to be turbulent, a correct turbulence model must be chosen to properly follow the real internal flow. The main problem is linked to the high swirl motion over walls with high curvature, which limits the use of

some turbulence models (see [74] for more details). The work of Madsen et al.[50] and Yeh [94] show the effect of some turbulence models able to work with this specific flow and compare the final numerical results with experimental data. Madsen et al.[50] investigated the internal nozzle flow on a large scale Danfoss atomizer, which has been experimentally investigated by Hansen et al. [28]. In addition to the turbulence models analysis, a sensitivity analysis on the multi-phase model has been carried out. Two grids have been generated on different geometries: one takes into account only the atomizer body, together with the three inlet channels; the second one takes also into account the first injection region after the nozzle exit. In this way, the influence of the outlet boundary has been investigated. The case analysed by Madsen et al.[50] has an inlet Reynolds number of the order of 12000 to 41000, therefore the flow within the inlet channels and the swirl chamber has been considered turbulent. Laminar and LES simulations have been performed with the Volume of Fluid (VOF)[31] model to describe the two-fluid interaction. A two fluid Euler/Euler simulation has been also performed to see the influence of the multi-phase model on the prediction of the atomizer performances. All these results are then compared with the experimental measurements of the tangential and axial velocity found by Hansen et al.[28], together with the numerical results predicted from the simple laminar case.
Both the multi-phase models display waves of small magnitude moving along the liquid interface and helical disturbance can be clearly identified. The air-core remains almost constant trough the conical swirl chamber and a similar behaviour can be found in the cylindrical part, with an higher diameter.
The geometry analysis shows that no differences can be detected in the whole domain, and it is also true for the outlet section of the nozzle. The tangential and axial velocities extracted at 10 mm below the top swirl chamber from experiments and simulations are in rather good agreement. The static wall pressure extracted from the VOF laminar and the two-fluid simulations are also in rather good agreement with the experimental data, while the VOF LES results under-predict the wall pressure. The latter result can be connected to the high level of viscosity introduced by the model.

Yeh [94] investigated four different turbulent models, which are three Linear Eddy Viscosity Models (LEVM) and one Algebraic Reynolds Stress Model (ARSM). They included the standard $k-\epsilon$ model [45], Launder-Sharmas's LRN $k-\epsilon$ model [44], Naganon-Hishida's LRN $k-\epsilon$ model [56] and Gastsky-Speziale's ARSM model [22]. The VOF method [31] has been adopted to track the liquid and gas position inside the numerical domain, while the surface tension between the two fluids has been modelled by the continuous surface force (CSF) method [4] in which the surface tension effect is modelled as a continuous volume force in a narrow region across the liquid-gas interface, rather than as a boundary value condition on the interface. The outlet Reynolds number evaluated at the exit section is equal to $Re_o = 2.7 \times 10^5$; at the inlet the turbulent kinetic energy and length scale are equal to $k_{in} = 0.01\left(u_{in}^2 + v_{in}^2 + w_{in}^2\right)$ and $l_{in} = 0.1 \times k_{in}^{1.5}/\epsilon_{in}$ [41], respectively. The value of the inlet turbulent dissipation rate can be defined as $\epsilon_{in} = k_{in}^{1.5}/0.005d_i$. The results obtained from all the turbulent models adopted, in terms of the liquid lamella thickness inside the atomizer, and radial distance of the external jet surface with the atomizer axis, are compared with the corresponding experimental data: the results show that all the turbulence models predict similar results as the measurements. The Gatski-Speziale's ARSM [22] model gives the best agreement with the experimental data of Jeng et al. [38]. Observing the turbulence intensity profiles at the atomizer exit, two peaks can be noticed, which occur in the near wall region and the liquid/gas interface region due to the high shear strain rates generated there. The standard $k-\epsilon$ model predicts the highest turbulence intensity, and therefore the highest diffusion rate, which yields to have the higher difference between the numerical results and experiments in terms of liquid lamella thickness $2h$ evaluated at the outlet section of the atomizer. Yeh [93] demonstrated that the this initial turbulent characteristics of the conical swirled jet lead to have a better atomization of the liquid film, and therefore to a different spray characteristics. This information shows that the internal nozzle flow must be characterized with the highest accuracy as possible. Yeh [94] concluded that the standard $k-\epsilon$ model predicts, under a qualitatively point of view, a reasonable results, although under the quantitative point of view is the most distant from the

experimental data; the ARSM shows both qualitatively and quantitatively agreement with the experimental data, as expected from the theory of the investigated model.

3.2 Jet development

Once the liquid exits the atomizer, a conical swirled jet is formed. Before it starts to break-up, the main jet characteristics are the jet angle, which influence the successive spray angle, and the break-up length. The latter parameter is really important to characterize the jet break-up. Connected to the air-core developments (section 3.1.1), Ramamurthi and Tharakan [62] investigated the flow transition in a conical swirled jet: the transition between the tulip stage and the fully developed cone shape has been investigated. An experimental campaign on helical pressure swirl atomizer has been performed: the ratio d_s/d_o has been changed, together with the swirl number ($1.1 \leq SN \leq 14.5$), to show the influence of these parameters on the produced jet. Cold tests have been performed with distilled water, with an injection pressure equal to 16 bar. Ramamurthi and Tharakan [62] defined the Weber number for the liquid phase as follows:

$$We_l = \frac{\rho_l h u_o^2}{\sigma} \tag{3.15}$$

where the half of the lamella thickness (h) has been considered as characteristic length scale while u_o represents the axial velocity components of the liquid evaluated at the exit section. The value of the liquid lamella thickness has been estimated measuring the value of the discharge coefficient of the nozzle (see Rizk and Lefebvre [68] for more details). The experiments show that the value of the spray cone angle increases together with the value of We_l: this is due to the increased inertia forces (which are proportional to the centrifugal ones) that arrest the collapse of the sheet induced by surface tension and yields the spray cone angle to increase. The tulip-shape jet can be observed for $We_l < 140$, while for $We_l > 170$ the jet assumes a cone-shape. The region $140 < We_l < 170$ represents the transition zone from

the two different shapes. A limit of 150 has been considered as demarcation point between the two different jet stages. For the cone-shape regime, the spray cone angle remains almost stable for all the investigated cases.

Jedelesnký and Jícha [36] investigated the hollow cone spray generated from a pressure swirl atomizer with and without the spill return. Light heating oil has been adopted, which has similar properties of real hydrocarbon fuel. All the tests have been made injecting the liquid into a chamber at ambient pressure (cold test). Different operating condition have been investigated, and therefore different jet stages have been recognized: changing the ΔP across the nozzle from 2 bar to 20 bar, the jet shape changes from the onion stage to the fully developed spray. At low values of ΔP, the surface tension forces have been observed to be dominant and overcome the radial momentum, which causes the film to collapse (poorly atomization with dripping character of the break-up process). Primary atomization of the entire liquid volume completes at $\Delta P > 4bar$, while a complete atomization is reached for $\Delta P > 10bar$.
The spray cone angle remains almost constant for all the cases where the hollow cone spray is formed, and it seems to not be dependent on the operating conditions: Jedelesnký and Jícha [36] pointed out that this value is practically given from the internal nozzle geometry, as also reported by Mandal et al. [51].

In literature several analytical models can be found, provided by Nonnenmacher and Piesche[57] and Moon and Bae [54] able to follow the jet development before it starts to break-up in ligaments and then into droplets. The development of the jet is really important to properly define the jet characteristics at the break-up point, from which the liquid structures produced after the break-up depend. Both of these two reported models have been validated with experimental data, showing their reliability for successive analysis.

3.3 Jet break-up

Ramamurthi and Tharakan [62] investigated the effect of turbulence on the jet break-up: the average surface roughness of the internal walls of the atomizer Ra have been changed between 0.5 and $12\mu m$. The results show that for high value of Ra the jet surface appears more frothy if compared with the same operating conditions at low value of roughness: this difference is linked to a different turbulent nature of the liquid emerging from the atomizer. Although the turbulent effect is visible form the pictures of the jet liquid surface, it does not influence the shape and the wave-growth pattern. Therefore, the turbulence of the flow does not accelerate or delay the formation of wave motion nor they bring about a change in the Weber number at which the transition of the jet shape takes place.

From the experiments, the frequency of the wave moving over the liquid surface has been measured by Ramamurthi and Tharakan [62]: only antis-symmetric waves have been recognized along the axial direction, while symmetric waves can be found only at low injection velocity (low We_l) where the surface tension induces this kind of instability. The authors pointed out that the tangential waves are present only for high values of the liquid Weber number. The measured frequency for the sinusoidal waves is close to 200 Hz for low We_l (~ 20) and it reaches 800 Hz at high We_l (> 150).

From spray photography, surface wave instabilities have been found by Jedelesnký and Jícha [36] to be the only responsible of the lamella break-up, contrary to Santolaya et al. [73] results, where two sheet atomization regimes were documented (perforations and surface waves). The mean measured break-up length is higher for the first atomization stages, while when the spray is formed ($\Delta P > 4bar$), the break-up point approaches the exit orifice due the relative high gas-to-liquid velocity; for the fully developed spray, the break-up length remains stable.

The instabilities moving within the liquid as well as over the liquid surface, caused by the high slip velocity between the liquid film and the ambient gas (Kelvin-Helmoltz type of instabilities), leads the jet to break-up into ligaments, filaments and finally into droplets in the form of a hollow cone spray. In a consecutive work of Jedelský et al. [37], the sheet has been observed to

deform due to the aerodynamic perturbations together with turbulence fluctuations imposed during the internal flow. In this work, Jedelsky et al. [37] compared the measured break-up information, as the break-up length, with the data coming from the analytical model developed by Senecal et al. [75] (see the following section 3.3.1). The investigated cases have a gas Weber number close to the critical one $We_{gc} = 27/16$: below this value the long wave growth dominates over the short waves and vice-versa. For the long wave instability, the sinuous (anti-symmetric) mode can be recognized from the photographic campaign. The dilatational or varicose (symmetric) mode, typical of the density ratio $\rho_g/\rho_l \sim 1$, is not present in the measurements as expected from the theory. For the three tested operating conditions, only the first one with $\Delta P = 5bar$ the long wave growth dominates, while for the other two with ΔP equals to 10 and 15 bar, short waves are also present and support the sheet break-up.
The liquid film starts to break into fragments at the axial distance equals to 6.7-8.9 nozzle diameters after the injection point, with a value of lamella thickness $2h_b/2h_o \approx 0.37$. The break-up length measured of 8.9-11.1 diameters is much lower than the theoretical values predicted from the linear model of Senecal et al. [75] equal to 30.0-49.8 diameters. The model assumes a spectrum of infinitesimal disturbances imposed on the initially steady motion of the liquid film, which leads to have fluctuations in velocity and pressure. Jedelský et al. [37] pointed out that in the real case, these disturbances have a finite value (for example the helical and the precession wave moving over the air-core interface) and if they are in resonance with the most unstable wave, the break-up length will reduce significantly. From the experiments, the jet break-up produces a irregular shaped ligaments as thin longitudinal threads in the primary zone and then these ligaments break-up in single droplet due to capillary instability.

The liquid viscosity has been found to damp the waves moving over the jet surface, and then it yields to have a coarser atomization. In particular, Rizk and Lefebvre [68] stated that:

- the viscosity yields to increase the initial film thickness;

- the viscosity yields the jet to resisting to the disintegration of the sheet into droplets;

- the viscosity yields to suppressing the formation of surface waves responsible of the jet break-up.

3.3.1 Analytical models

Different analytical model able to estimate the break-up of the liquid lamella and the droplet size after the primary break-up. Most of them are based on the model developed by Dombrowsky and Jhons [12] for a liquid sheet. This section reports one of the most recent development on these previous works, made by Senecal et al. [75] and Panchangula et al. [58]. To get a complete overview on the jet break-up, see Sirignango and Mehering [76].

One of the most used and simple atomization model for conical swirled jet has been developed by Senecal et al. [75], which is based on the Dombrowsky and Jhons [12] model. In this previous work only long growth waves have been taken into account, but this simplification has been demonstrated that yields to have inaccuracies on the predicted sheet stability. Moreover, this assumption cannot be used to predict the break-up of a conical swirled jet for the modern atomizer with very small dimension. With their novel break-up model, Senecal et al. [75] wanted to take into account the effect of viscosity, surface tension and the surrounding gas which can be readily implemented in multi-dimensional simulations of transient sprays. The model must be able also to take into account the effect of both the long and short wave effect.
The stability analysis of the liquid sheet follows the approach of Sleicher and Sterling [77], Levich [49] and Reitz and Bracco [63] for the analysis of stability of cylindrical liquid jets. The model is 2D and takes into account a viscous and incompressible liquid sheet of the thickness $2h$, moving with a velocity U through a quiescent, inviscid and incompressible gas medium. To follow all the perturbations, the reference system moves together with the liquid sheet; a spectrum of infinitesimal perturbations are imposed on the

initial steady motion, and growth as expressed from the following relation:

$$\eta = \Re\left[\eta_0 e^{(ikx+\omega t)}\right] \tag{3.16}$$

where η_0 represents the initial wave amplitude; $k = 2\pi/\lambda$ is the wave number and $\omega = \omega_r + i\omega_i$ is the complex growth rate. All these perturbations induce a fluctuations on the axial (u) and radial v velocity components and pressure (P) flow field for both the liquid and the gas. The wave that lead to the break-up has the highest value of ω_r, denoted Ω_s; the ligament and the subsequent droplet size can be evaluated considering the characteristic wave length $\Lambda_s = 2\pi/K_s$, where K_s is the wave number corresponding to the maximum growth rate Ω_s. With this assumptions, the velocity and pressure field can be evaluated in space and in time, which at the end lead to define the following dispersion equation for the sinuous mode:

$$\begin{aligned}\omega^2\left[\tanh(kh)+Q\right]+\omega\left[4v_l k^2\tanh(kh)+2iQkU\right]\\ +4v_l^2k^4\tanh(kh)-4v_g^2k^3\mathscr{L}\tanh(\mathscr{L}h)-QU^2k^2+\frac{\sigma k^3}{\rho_l}=0\end{aligned} \tag{3.17}$$

where $Q = \rho_g/\rho_l$ and $\mathscr{L} = k^2 + \omega/v_l$. For the varicose mode, a similar dispersion equation can be found just replacing the $\tan(kh)$ and $\tanh(\mathscr{L}h)$ with $\coth(kh)$ and $\coth(\mathscr{L}h)$ respectively.
Inviscid and viscid analysis have been performed by Senecal et al. [75] with this dispersion relation. Starting with the inviscid assumption, the dispersion equation for both modes becomes:

$$\omega^2\left[\tanh(kh)+Q\right]+\omega 2iQkU-QU^2k^2+\frac{\sigma k^3}{\rho_l} \quad \text{for sinuous mode} \tag{3.18}$$

$$\omega^2\left[\coth(kh)+Q\right]+\omega 2iQkU-QU^2k^2+\frac{\sigma k^3}{\rho_l} \quad \text{for varicose mode} \tag{3.19}$$

The solution for the growth rate ω_r are equal to:

$$\omega_r = \frac{\sqrt{\tanh(kh)QU^2k^2 - [\tanh(kh) + Q]\,\sigma k^3/\rho_l}}{\tanh(kh) + Q} \quad \text{for sinuous mode} \tag{3.20}$$

$$\omega_r = \frac{\sqrt{\coth(kh)QU^2k^2 - [\coth(kh) + Q]\,\sigma k^3/\rho_l}}{\coth(kh) + Q} \quad \text{for varicose mode} \tag{3.21}$$

For a long wave assumption $\tanh(kh) \approx kh$ and for $Q \ll 1$ (sinuous wave growth dominates), the solution of dispersion equation can be written as follows:

$$\omega_r = \frac{\sqrt{QU^2k^2h - (kh + Q)\sigma k^3/\rho_l}}{kh + Q} \tag{3.22}$$

which can be simplified if $Q \ll kh$ obtaining the identical Squire's results [80]:

$$\omega_r = \sqrt{\frac{QU^2k^2h - \sigma k^3/\rho_l}{kh}} \tag{3.23}$$

The long wave growth has been found in experiments with low liquid velocity, and in the opposite situation Senecal et al. [75] pointed out that short wave growth can dominates. In this case the value of k assumes very high value, which yields to have $\tanh(kh) = \coth(kh) = 1$, and then Eq. 3.20 and 3.21 reduce to:

$$\omega_r = \frac{\sqrt{QU^2k^2 - (1 + Q)\sigma k^3/\rho_l}}{1 + Q} \tag{3.24}$$

which can be further simplified with the assumption of $Q \ll 1$:

$$\omega_r = \sqrt{QU^2k^2 - \sigma k^3/\rho_l} \tag{3.25}$$

If Eq. 3.23 is compared with Eq. 3.25, can be found that $\omega_{r,short} = \sqrt{kh}\omega_{r,long}$: this means that short waves growth dominate over the long

wave growth only if $kh > 1$. From a comparison with the analytical data explained above and the experiments, Senecal et al. [75] proved that at low We_g, the long wave growth dominates, and vice-versa for high We_g. Therefore, the authors defined a critical gas Weber number $We_{g,critical} = 27/16$ as the Weber number at which the dimensional break-up length L_b/h assumes the same value for both long and short analysis. The effect of the viscosity has been taken into account in the Dombrowski and Jhons [12] simplified model for long waves. However, the effect of the viscosity is underpredicted due to the assumption that the model is 1D and not takes into account the variation of the film in the y direction (normal to the jet development i.e. along the radial direction in the 3D real jet). Senecal et al. [75] defined a solution for the sinuous waves able to takes into account the viscosity effect. Starting from the inviscid solution, all the terms of second order in viscosity can be neglected, and the resulting growth rate can be written as follows:

$$\omega_r = -\frac{2v_l k^2 \tanh(kh)}{\tanh(kh)} + \frac{\sqrt{4v_l^2 k^4 \tanh(kh) - Q^2U^2k^2 - [\tanh(kh) + Q](-QU^2k^2 + \sigma k^3/\rho_l)}}{\tanh(kh) + Q} \tag{3.26}$$

Then, for the long waves analysis, in the limit of $Q \ll kh$, Eq. 3.26 can be simplified:

$$\omega_r = -2v_l k^2 + \sqrt{4v_l^2 k^4 + \frac{QU^2 k}{h} + \frac{\sigma k^2}{\rho_l h}} \tag{3.27}$$

While for the short waves in the limit of $Q \ll 1$, Eq. 3.26 can be simplified as follows:

$$\omega_r = -2v_l k^2 + \sqrt{4v_l^2 k^4 + QU^2 k^2 + \frac{\sigma k^2}{\rho_l}} \tag{3.28}$$

At the end of this analysis, Senecal et al. [75] found out that for low value of the gas Weber number ($We_g < We_{g,critical}$), the effect of the viscosity is not visible, while for higher values of $We_g > We_{g,critical}$ its presence yields to have a different value of ω_r and show the importance to consider the liquid viscous for these case.
With the information of the most unstable perturbation which is moving over the liquid surface, the jet break-up can be defined. The physical mechanism of the sheet atomization follows the theory proposed by Dombrowski and Jhons [12]: when the amplitude of the perturbation reach the critical value $\eta_b = h$, the liquid film starts to break-up to form cylindrical ligaments; subsequent break-up of these ligaments lead to produce the droplets which compose the primary spray. Then with Eq. 3.16, the break-up time τ can be estimated:

$$\eta_b = \eta_0 e^{\Omega_s \tau} \Rightarrow \tau = \frac{1}{\Omega_s} \ln\left(\frac{\eta_b}{\eta_0}\right) \tag{3.29}$$

With the break-up time, the break-up length can be defined as:

$$L_b = V\tau = \frac{V}{\Omega_s} \ln\left(\frac{\eta_b}{\eta_0}\right) \tag{3.30}$$

where the quantity $\ln(\eta_b/\eta_0)$ is set constant ad equal to 12 (Dombrowski and Hooper [10]); V is the absolute liquid jet velocity, while U represents the relative velocity between the liquid and the gas. The above expression is valid for annular liquid jet, which the value of the half of lamella thickness h does not change along the radial direction. Therefore to take into account also the attenuation of the liquid film for the short waves, the growth rate must be integrated over time so that the total growth is used to predict the break-up length for the long waves. The final definition of the break-up length can be written as follows:

$$L_b = V\left[3\ln\left(\frac{\eta_b}{\eta_0}\right)\right]^{2/3}\left(\frac{J\sigma}{Q^2U^4\rho_l}\right)^{1/3} \tag{3.31}$$

where $J = ht$ and it is a constant value. Always for the long waves, the most unstable wave number can be defined as:

$$K_s = \rho_g U^2 / 2\sigma \tag{3.32}$$

and the ligament size can be defined with the following relation:

$$d_L = \sqrt{\frac{16h}{K_s}} \tag{3.33}$$

.

For the short waves, the ligament size can be defined as:

$$d_L = \sqrt{\frac{8h}{K_s}} \tag{3.34}$$

where K_s is defined adopting Eq. 3.28. For both long and short waves, the final droplet size d_D after the primary break-up can be defined using the Weber's theory for a break-up of a cylindrical, viscous liquid columns [90]. The droplet diameter can be written as a function of d_L and the Ohnesorge number $Oh = \mu_l / \sqrt{\rho_l \sigma d_l}$ as :

$$d_D = 1.88 d_L \left(1 + 3Oh\right)^{1/6} \tag{3.35}$$

With the information of the ligament and droplet size, the drop size spectrum of the primary spray can be represented by a Probability Density Functions (PDF), as shown from different authors like Villermaux et al. [88], Dumochel [15] and Tratnig and Brenn [86].

A 3D model on the conical swirled jet break-up has been developed by Panchangula et al. [58] (Senecal et al. developed a 2D model), able to take into account the swirl effect on the development of the conical swirled jet. A linear stability analysis of an inviscid, swirling, annular sheet has been performed: the model is similar to Senecal et al. [75] model, but due to the three dimensional assumption, all the velocity components have been taken to account, and not only the velocity along the radial and axial

directions. Moreover, the model of Panchangula et al. [58] is able to take into account the motion effect of the surrounding gas (inside and outside the liquid cone). A dispersion equation have defined, and its resolution in terms of instability region is defined for different configurations: the initial internal and external radius of the annular jet, the liquid motion (swirled or not), and the internal and the external gas motion. The results show that the swirl motion has a stabilizing effect for Weber swirl number (Eq. 3.36) lower than 2.

$$We_s = \rho_l U W_s^2 / \sigma r_b \tag{3.36}$$

In Eq. 3.36 W_s represents the swirl strength and r_b the external radius of the jet. The stabilizing effect is more prominent for a high ratio between the internal and the external radius of the liquid annular jet.
For low value of We_s, the most unstable wave has only an axial mode, and therefore the circumferential wave number is equal to 0, while increasing the swirl strength W_s, the region of instability increases and then the most unstable wave has a non-zero circumferential wave number but zero axial wave number. This yields to conclude that the swirl effect induces to shift of the most unstable wave from the axial to the circumferential mode.

Chapter 4

Internal nozzle flow investigations

4.1 Introduction

Experimental measurements of the internal nozzle flow have been presented in Chapter 3: most of the experiments have been made on a large scale atomizer to provide an optical access for the internal nozzle flow visualizations and measurements. However the atomizer scale effects on the internal nozzle flow is not clear. To current numarical tools allow to simulate the internal nozzle flow: as already shown in section 3.1.6, the comparison of the simulated internal nozzle flow adopting different multiphase models and the experimental data shows a good agreement between the two investigation way ([33][7][50][94]. In this chapter, the atomizer internal flow has been investigated numerically. The atomizer performances and the liquid film characteristics at the exit section of the atomizer have been extracted, as the liquid lamella thickness or the velocity profile for each component over the radius.

4.2 Injector geometry and boundary conditions

Figure 4.1 shows the view of the investigated aeronautical injector. It is divided into three different parts: the first at the top represents the connection between the feeding line with the main body of the atomizer (colored in yellow); the second part represents the pressure swirl atomizer (colored in cyan) while the last part represents the injection chamber (colored in green). The PSA is composed by 4 inlet channels that are connected to a pressure swirl chamber composed by only a convergent section. These two characteristics of the atomizer represent the critical points that limit the investigation on it. Indeed all the previous investigations made on the PSA are commonly made on an classical atomizer, where the inlet channels are normal to the main axis of the atomizer, and therefore the inlet flow has only a tangential components; in the investigated case, the inlet channels yields the flow to have not only a tangential velocity component, but also axial and radial components. Moreover, the common pressure swirl atomizer is composed by a cylindrical swirl chamber part where the flow becomes uniform (fully swirled and no inflow effects are presents), which is connected to a convergent section (typically conical, but can assume different shape, as trumpet shape for example): here the cylindrical part of the swirl chamber is not present and the uniform flow is not guarantee for all the operating conditions. All these differences, yields to not have a clear view of the real behaviour of the atomizer under investigation with the theory or with the simplified semi-empirical correlation adopted to describe a PSA with classical geometry. Some general information on similar geometry investigated in this work can be found in literature from the works of Hansen et al. [28] and Madsen et al. [50] (see section **??**), on a large scale Danfoss atomizer.

All the main PSA dimensions are reported in Figure 4.2.

To evaluate the atomizer performance with the numerical simulations, all the boundary conditions must set in such a way to have a single physic solution. For the investigated case, the whole external surface of the atomizer has been considered as wall with no-slip condition; at the inlet the mass flow is set, while at the outlet the pressure (gauge or absolute) of the injection chamber has been imposed. From the geometry shown in Fig-

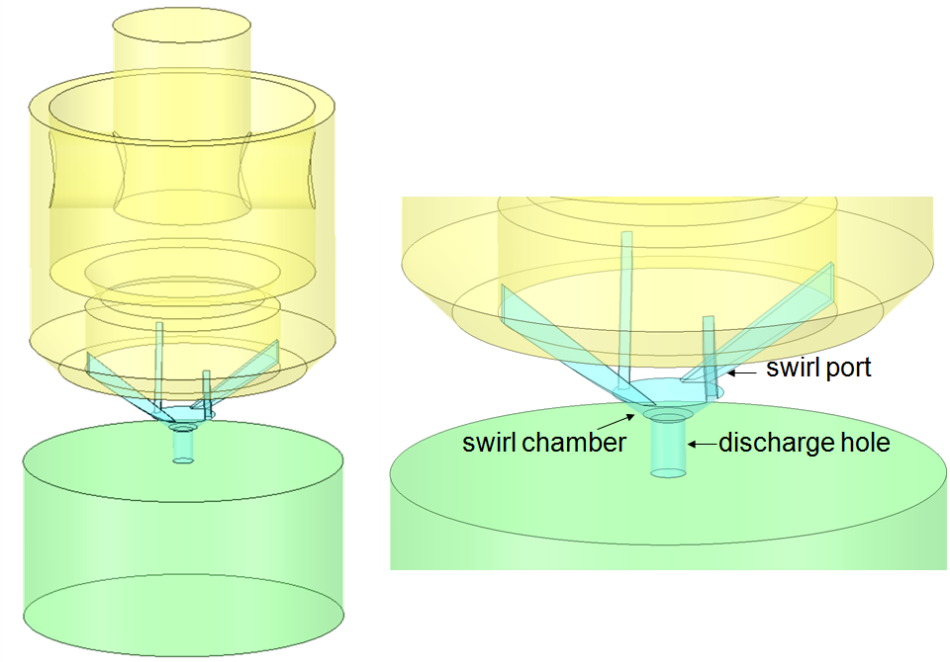

Figure 4.1: Total geometry adopted for the simulations.

ure 4.1 it is clear that the inlet boundary condition will not influence the solution within the PSA, but this is not true for the outlet condition: it is too close to the region of interest and its influence cannot be excluded. Different authors, as Chinn [6] or Madsen et al. [50] adopted different strategies to set-up correctly their simulations: the first imposed a pressure-inlet boundary condition, where the total pressure is fixed and therefore the exit velocity and static pressure depend only from the solution defined within the atomizer and not vice versa. The second tested two different geometries which differ for the presence of an additional volume present after the exit section of the atomizer, which represents the injection chamber; the static pressure has been imposed in both the cases, and the final results show

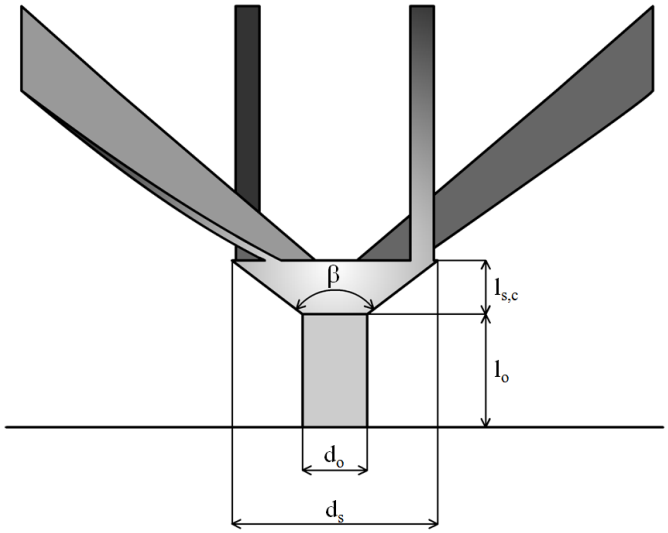

$\beta[deg]$	$d_o[mm]$	$d_s[mm]$	$l_o[mm]$	$l_{s,c}[mm]$	$A_i[mm^2]$	$d_{Hi}[mm]$
116	0.625	2.000	1.072	0.428	0.288	0.230

Figure 4.2: View of the atomizer witht its main lenght value; the value of A_i and d_{Hi} represents the total inlet area and the hydraulic dimater of each inlet channels respectively.

that there is any visible effect on it. Although different solutions have been tested in the past to evaluate the internal nozzle flow, in this work an additional volume has been added to evaluate correctly the entrainment of the environmental gas with the liquid emerging from the nozzle. It is modelled as cylindrical body, centred with the atomizer axis, with length equals to $l_c = 8 \times d_o$ and with a diameter $d_c = 16 \times d_o$.

4.3 Operating conditions

For the considered PSA, 8 operating conditions are evaluated and resumed in Table 4.1. In this table are also reported the inlet (Eq. 2.7) and the outlet (Eq. 2.8) Reynolds number. This two values show the nature of the

No.	Case	$\dot{m}_l[g/s]$	$P_c[bar]$	$\rho_g[kg/m^3]$	Re_i	Re_o
1	Take off (50%)	2.8	32.0	13.3	1728	4414
2	Take off (100%)	5.6	32.0	13.3	3430	8762
3	Approach (30%)	3.0	12.8	6.8	1872	4781
4	Cruise	6.2	11.4	5.5	3837	9801
5	Idle (7%)	3.4	5.1	3.4	2115	5402
6	Descendent Idle	2.8	3.1	1.9	1736	4434
7	Low Idle	3.3	3.1	2.4	2042	5216
8	Type test	3.4	31.3	12.4	2097	5356

Table 4.1: Operating conditions investigated.

$\rho_l[kg/m^3]$	$\mu_l[sPa]$	$\sigma[N/m]$
801	0.0013	0.022

Table 4.2: Properties of Kerosene Jet A-1.

flow at the inlet and at the outlet, and consequentially they allow to define if the flow within the atomizer can be considered laminar or turbulent.

The liquid adopted is the fuel Kerosene Jet A-1, while the environmental gas is air. The liquid properties remain always constant for all the cases and their value can be found in Table 4.2; the gas properties change according to the injection chamber pressure and temperature, and the value of density can be found in Table 4.1. The simulations have been considered isotermal and not reacting, and therefore only the fluid-dynamic effects are taken into account.

4.4 Mathematical modelling and Grid generation

The flow development inside the injector and at the nozzle exit proximity is predicted implementing the two-phase flow VOF (Volume of Fluid)

methodology [31]. The model numerically solves the fully 3D Navier-Stokes equations describing the fluid motion, with the time averaged forms of the continuity, momentum and conservation equations for the scalar variables using collocated Cartesian velocity components on structured and unstructured numerical grids. The discretization method is based on the finite volume approach and the pressure correction method is according to the Semi-Implicit Method for Pressure-Linked Equations (SIMPLE) algorithm [60]; high resolution hybrid and CICSAM (Compressive Interface Capturing Scheme for Arbitrary Meshes) [87] schemes are adopted for the spatial discretization, while the time discretization is based on a fully implicit Crank-Nicolson scheme.
Hybrid 3D grids were created, made by tetrahedral, hexahedral and prismatic cells; the tetrahedral elements were used to mesh the inclined channels of the PSA and the subsequent insertion into the swirling chamber; the remaining part of the domain was meshed with hexahedral or prismatic cells. Picture (a) in Figure 4.3 shows the grid structure adopted for the simulation; picture (b) shows the zoom of the grid in the upper body of the atomizer, while in picture (c) and (d) can be seen respectively the view of the grid adopted to discretize the PSA and a zoom on the transition zone between the hexahedral core and the tetrahedral grid in the pressure swirl chamber.

Figure 4.4 shows a view of the internal flow field obtained with the Large Eddies Simulations for the case 1: the red and the blue colors represent the liquid and the gas respectively . The whole internal nozzle flow domain can be described and all the initial jet characteristics can be easily extracted. These informations are then used in following jet break-up investigations.

4.4.1 Grid dependence analysis

To take into account the grid size on the atomizer performances predicted with the internal nozzle flow simulations, a grid dependence analysis has been performed. The grid structure explained previously remains constant, while the total number of cells is changed. The analysis has been performed on case 1 listed in Table 4.1, where the RNG $k-\epsilon$ turbulent model has been

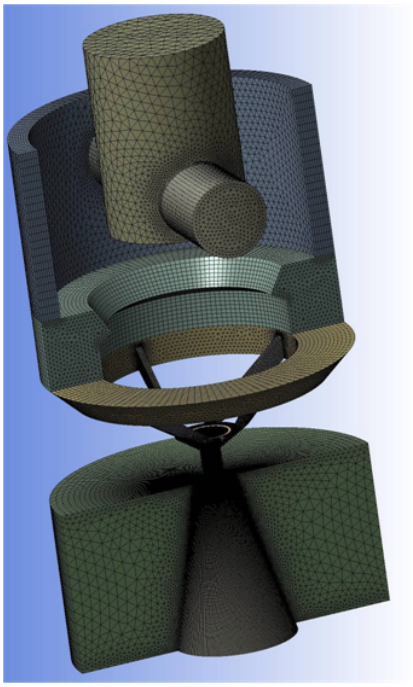

(a) Grid lateral view

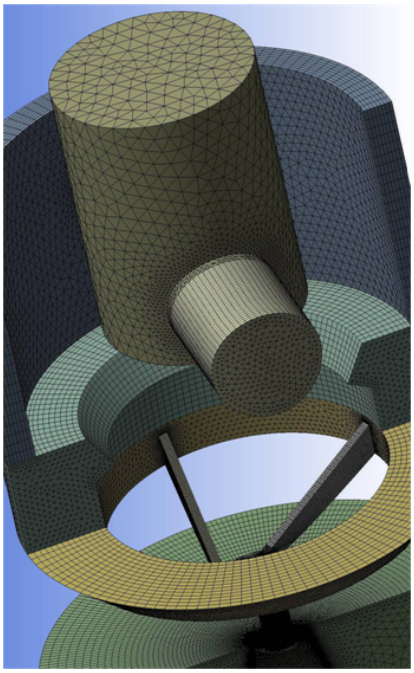

(b) Grid lateral view - zoom in

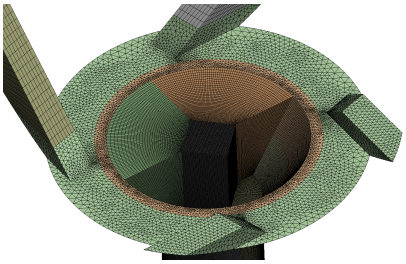

(c) PSA grid

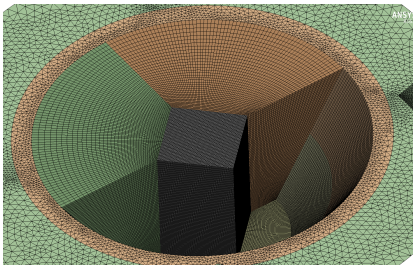

(d) PSA grid - detail of swirl chamber grid

Figure 4.3: View of the grid structure adopted for the simulations.

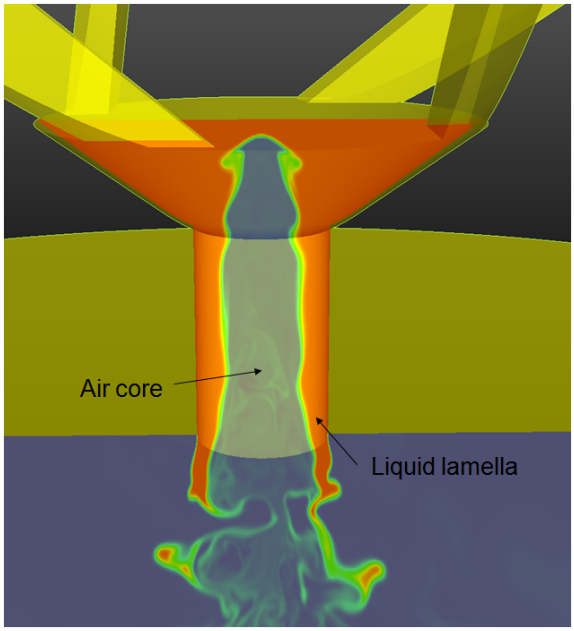

Figure 4.4: View of the volume of fraction field within the pressure swirl atomizer for the case No. 1 of Table 4.1.

adopted.
The grid influence has been defined on the prediction of three different macroscopic parameter: the liquid pressure drop the discharge hole ΔP_{hole}, the liquid lamella thickness $2h$ and swirl velocity u_{swirl} at the exit section of the atomizer.
The VOF method is able to distinguish if in one cell the liquid or the gas is present: when the phase variable α is equal to 1, the cell is fully occupied by the liquid, while if $\alpha = 0$ the cell is fully occupied by the gas (see Eq. 4.1). For the value of the phase variable in between 0 and 1, the liquid interface can be identified. In the reality the interface has infinitesimal thickness (ideally is a surface without thickness), but for the VOF method a region

of possible location of the interface can be identified.

$$\alpha(\mathbf{x}, t) = \begin{cases} 0 & \text{outside the liquid phase,} \\ ]0, 1[& \text{at the interface,} \\ 1 & \text{inside the liquid phase.} \end{cases} \tag{4.1}$$

To take into account this aspects, the value of the lamella thickness at the exit section of the atomizer has been evaluates considering 5 different levels of threshold of the phase variable to define where the liquid is present. These values have been set equal to 0.10, 0.25, 0.50, 0.75 and 0.90. For every time step, the mean value of $2h$ and the corresponding variation range have been extracted. This procedure has been done for several time steps, and a final value of the liquid lamella thickness and RMS have been defined.
Figure 4.5 shows the variation of three parameter under investigation for six different grids with a total number of cells equal to 1.2, 2.6, 3.2, 4.6, 8.0 and 12.0 millions. It can be noticed that for a total number of cells higher than 8.0 millions, there is no effective variation of the results for all the parameters; this result is also confirmed from the uncertainty on the liquid lamella thickness which remains almost constant for the selected number of cells range.

4.5 Results

4.5.1 PSA performances

In absence of experimental data, the atomizer performances can be extracted from numerical simulation or predicted by the semi-empirical correlations. Even if the latter way not yields to have the estimation of the real atomizer behaviour, due to the fact that they are validated over a different atomizer geometry, they provide the trend of variation of the atomizer performance parameters and the possible realistic variation range, by changing the operating condition (the geometry and the liquid properties are fixed for all the cases).

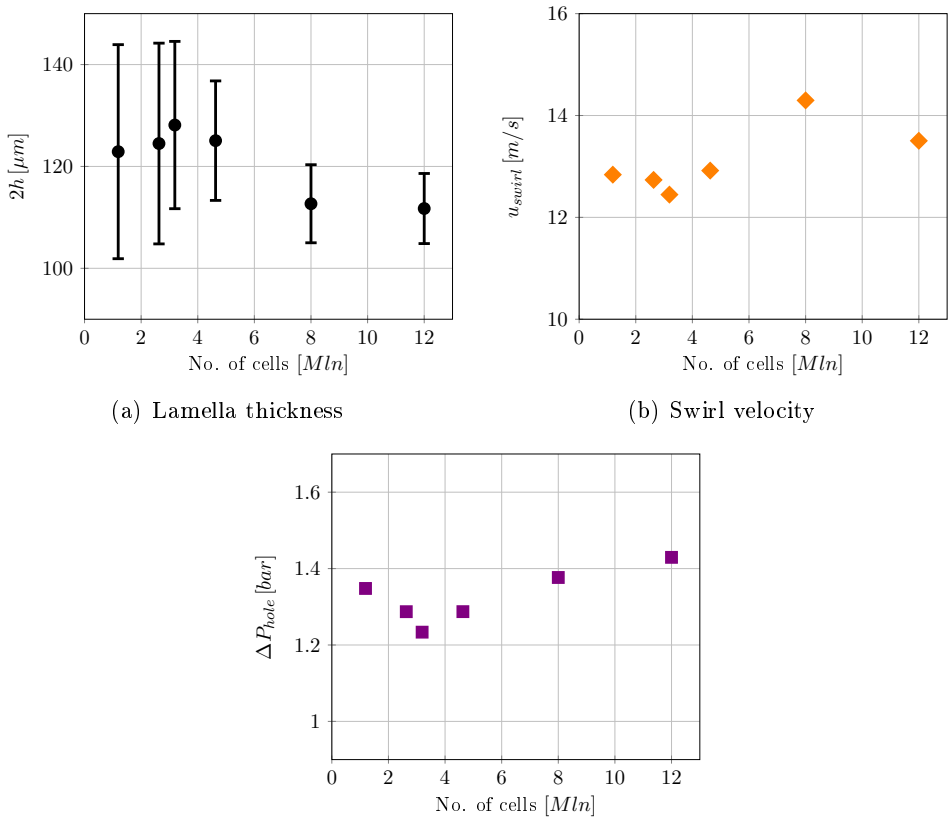

(a) Lamella thickness

(b) Swirl velocity

(c) ΔP

Figure 4.5: Variation of liquid lamella thickness (a) and swirl velocity (b) at the exit section of the atomizer, and the pressure drop the discharge region of the atomizer (c) for RNG $k-\epsilon$ simulations of test case No. 1 of Table 4.1.

In Table 4.1 the value of Reynolds number, following different definition, are reported. Re_i can be used to define if the flow entering into the swirl chamber is already turbulent or not: in the present study, this undimensional parameter is not always higher than 3000 for the investigated cases.

This preliminary result suggests that not all the cases the flow can be turbulent within the PSA. However, within the atomizer the swirl motion can induce the flow to become turbulent, or vice-versa. Therefore, to take into account also the possible change on the flow nature, turbulent simulations have been performed.
From the literature the VOF LES has been found to be able to correctly predict the internal nozzle flow (see Madsen et al. [50], where the LDA measurements of the internal nozzle flow are compared with the numerical results on a large scale Danfoss atomizer). For this reason, the following analysis has been carried out performing LES.
The atomizer performances are investigated considering two important macroscopic parameters: the liquid lamella thickness at the exit section $2h$ and the discharge coefficient C_d. Another important parameter to investigate is the spray cone angle θ, but in all the performed simulations, the value of this parameter can be defined only for the initial injection region, while the correct estimation of the spray cone angle must be defined further downstream, where the jet is fully developed. For this reason, the estimation of θ has not been taken into account in this analysis.

Evaluation of $2h$

This parameter is influenced from many parameter of different nature: atomizer geometry, liquid properties and operating conditions. In this analysis, the firsts two are fixed, and only the influence of the operating conditions are considered. From the simulations, the value of $2h$ can be estimated in two ways: the first it is represented by the direct measurement of the liquid film thickness considering the phase variable α ($2h_\alpha$), as already explained in section 4.4.1; the second way is represented considering the point where the pressure reaches the external value, i.e. the zero gauge pressure at the exit section $P_{Go} = 0$ ($2h_{P_{Go}=0}$) as explained in the work of Chinn [6] and Yule and Chinn[7].

Figure 4.6 shows the numerical values of $2h$ extracted following the pre-

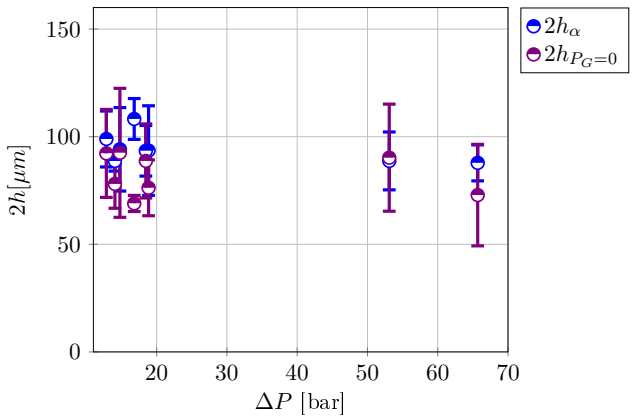

Figure 4.6: Comparison of the liquid lamella thickness extracted from the simulation data and predicted by the simulations, for different operating conditions.

vious definitions. Both the measurements are in good agreement, and predict similar values of liquid lamella thickness for the investigated operating conditions.

In Figure 4.7 the value of $2h$ from the common used semi-empirical correlations (reported in Appendix A.1) are reported together with the value of liquid lamella thickness extracted directly from the simulations and evaluated considering different information of the internal flow field, as defined by Jedelský and Jícha [36]:

$$2h_{K_v} = \frac{\dot{m}_l}{\pi d_o K_v^2 \sqrt{2\rho_l \Delta P}} \tag{4.2}$$

where K_v is the velocity coefficient defined at the exit section of the atomizer, while ΔP represents the pressure drop across the inlet of the entire geometry and the exit section of the atomizer. Both K_v and ΔP are estimated considering the predicted flow field form the simulations. The ΔP fluctuations over the simulation time is lower than 1%, while the velocity fluctuations are always lower than 6%: these informations are used to evaluate the uncertainty on the estimation of the liquid lamella thickness

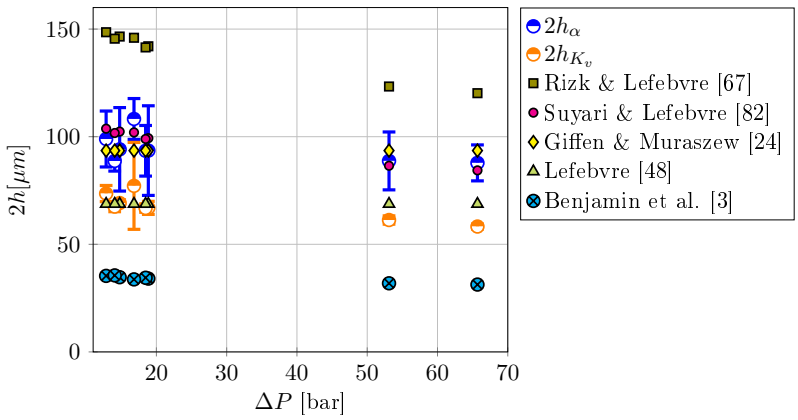

Figure 4.7: Comparison of the liquid lamella thickness extracted from the simulation data and predicted by the simulations, for different operating conditions.

using the formula 4.2.

The measured values of $2h$ are always within the predicted values from semi-empirical correlations: this result yields to consider the numerical estimation of the liquid development within the atomizer representative of a realistic atomizer behaviour. Moreover, from the graph shows in Figure 4.7 it can be noticed that the the correlations of Suyari and Lefebvre [82] and Giffen and Muraszew [24] are in good agreement with the numerical data for the selected operating conditions, while the value of $2h_{K_v}$ is in good agreement with the Lefebvre [48] correlation. The correlation of Benjamin et al. [3] has been defined for a very large scale atomizer, and the big gap between the predicted values with the other correlations and the measured one, shows that the scale can be an important aspect to take into account to investigate the PSA behaviour.

Discharge coefficient C_d

Another important parameter used to evaluate the atomizer performance is the discharge coefficient C_d. In Appendix A.2 are reported the common

used semi-empirical correlation adopted by the industries to define this parameter by changing the atomizer geometry, liquid properties and operating conditions. As for the liquid lamella thickness, all these correlations are validated on different atomizers.

In Figure 4.8 the estimated value C_d from the simulations are reported and the predicted value from 5 semi-empirical correlations. In this graph it can be noticed that the value of the discharge coefficient extracted from the simulations remains almost stable, as expected from the theory [61]. This result confirm that the reaching of the inviscid regime for all the investigated operating conditions, i.e. $Re_o > 3000$, yields the C_d to not change with the Re_o (variation lower than 1%). Therefore, for all the cases, the atomizer geometry characteristics are the only parameters which influence the discharge coefficient.

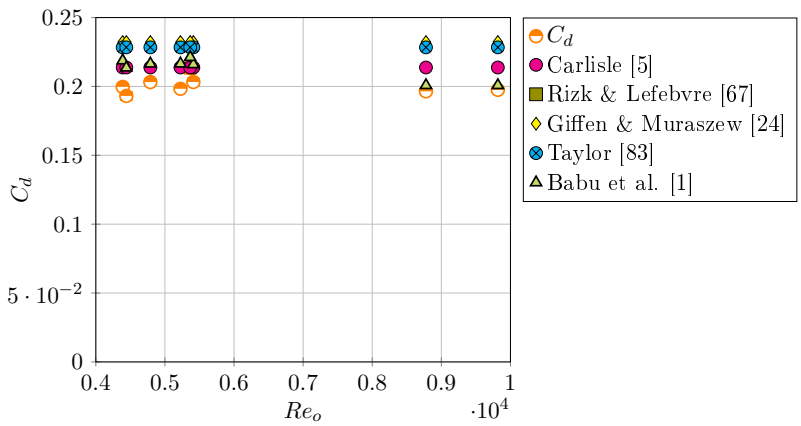

Figure 4.8: Comparison of the liquid lamella thickness extracted from the simulation data and predicted by the simulations, for different operating conditions.

Always in Figure 4.8 it can be noticed that the estimated values from the simulations agree reasonably well with all the semi-empirical correlations: the Giffen and Muraszew [24] correlation over-estimates the prediction of the discharge coefficient by 20% respect the value extracted from the sim-

ulations, while the other semi-empirical correlation predict a C_d with a difference even lower than the Giffen and Muraszew correlation. Moreover, it can be seen that the averaged C_d is low, as expected for this kind of atomizer, due to the presence of the air-core at the exit section.

4.5.2 Turbulence model investigations

The turbulence phenomena is a critical issue that must be consider to evaluate the internal nozzle flow. With the data obtained from the previous Large Eddies Simulations, the nature of the flow can be now evaluated considering the Walzel [89] theory which assumes that the flow can be considered turbulent if Re_W (see Eq. 2.10) is higher than 5000. This assumption is verified for all the investigated cases, and it retroactive justify the previous turbulent simulations.

In literature different comparison between numerical turbulent simulation results and experimental measurements of the internal flow field can be found (see 3.1.6). On the investigated atomizer, a turbulent simulation analysis is performed, with the aim to show the differences on the estimation of the atomizer performances. Therefore, for case 1 listed in Table [**?**], three turbulent simulations are performed: the first is the LES, which results are partially shown in the previous section; for the second and the third simulation the Reynolds Stress Model (RSM)[27] and RNG $k-\epsilon$ model [92] are used respectively. The latter two RANS method are able to properly follow the swirl motion of the flow over a concave curvature. To perform faster 3D VOF simulations with these two turbulent models, the grid with 8 millions of cells has been adopted (see section 4.4.1).

Estimation of $2h$ and C_d

The first analysis carried out considers the macro structure of the flow, considering the influence of the turbulence model on the liquid lamella thickness $2h$ and the discharge coefficient C_d.

In Table 4.3 the value of $2h$ extracted directly from the simulations are reported considering the phase variable α, the radial position where the gauge pressure is zero $P_{Go} = 0$, the value extracted from Eq. 4.2 and the value predicted by the common semi-empirical correlations (reported in Appendix A.1) with the informations coming from the simulations. In this table the values of ΔP for all the simulations are reported, to show the effect of the turbulent model on the pressure drop along the atomizer.
Starting from the values extracted from the simulations, it can be noticed that the values extracted from the simulations for $2h_{P_{Go}=0}$ is in rather good agreement with the three performed simulations; the values of $2h_\alpha$ for LES and the RNG $k-\epsilon$ simulation are in rather good agreement one to each other, as well with the values of $2h_{P_{Go}=0}$; the value of $2h_\alpha$ extracted from the RSM simulation is the only one that differ from the others, which is $\approx 35\%$ higher than the corresponding value extracted from LES. The results predicted with the semi-empirical correlations not change for the three investigated turbulent models: this is connected to the fact that most of them depend on the geometric parameters, which are constant for all the cases, and mainly from the total pressure drop across the atomizer ΔP. Looking at Table 4.3, it can be noticed that this value does not effectively change with the turbulence model ($\Delta P \approx 13.68$), and this result justifies the constant value of $2h$ predicted by the semi-empirical correlations.

From this analysis can be concluded that the different turbulent models adopted do not influence the fluid-dynamic within the atomizer, due to the fact that $2h_{P_{Go}=0}$ evaluated with the three investigated turbulent models are in good agreement. The values of $2h_\alpha$ are in good agreement with between the RNG $k-\epsilon$ and LES, but for the RSM simulation, this parameter assumes an higher value. From this analysis it can be concluded that RSM simulation can be used to evaluate a realistic behaviour of the atomizer (similar flow characteristics within the atomizer), but this turbulence model introduce an additional diffusivity on the phase variable α which reduces its accuracy.

Table 4.4 shows the value of C_d calculated adopting the numerical simulations results and the predicted values obtained using the semi-empirical correlations reported in Appendix A.2. As it can be observed the results are all in good agreement with a small variation of the discharge coefficient.

	LES	RNG $k-\epsilon$	RSM
ΔP [bar]	12.85	14.95	13.26
$2h_{\alpha}$	101.99 ± 15.14	112.68 ± 6.88	135.57 ± 5.47
$2h_{P_{Go}=0}$	101.60 ± 9.95	106.15 ± 15.04	97.88 ± 0.45
$2h_{K_v}$	73.58 ± 3.76	70.62 ± 38.03	83.37 ± 16.44
Rizk & Lefebvre [67]	148.54	143.68	147.35
Suyari & Lefebvre [82]	103.72	100.42	102.92
Giffen & Muraszew [24]	93.54	93.54	93.54
Lefebvre[48]	68.74	68.74	68.74
Benjamin et al. [3]	35.33	35.93	35.47

Table 4.3: Value of liquid lamella thickness $2h$ at the exit section of the atomizer obtained with the investigated turbulent models; all the values are expressed in μm.

	LES	RNG $k-\epsilon$	RSM
ΔP [bar]	12.85	14.95	13.26
C_d	0.20 ± 0.00	0.19 ± 0.02	0.20 ± 0.00
Carlisle [5]	0.21	0.21	0.21
Rizk & Lefebvre [67]	0.23	0.23	0.23
Taylor [83]	0.23	0.23	0.23
Babu et al. [1]	0.22	0.22	0.22
Giffen & Muraszew [24]	0.32	0.32	0.32

Table 4.4: Value of discharge coefficient C_d obtained with the investigated turbulent models.

Comparison of the internal flow field

Another interesting aspects to evaluate is the difference of the internal velocity flow field. In Figure 4.10 the values of the liquid axial and swirl velocity components are reported, which are taken at different planes along

the atomizer axis, as shown in Figure 4.9.

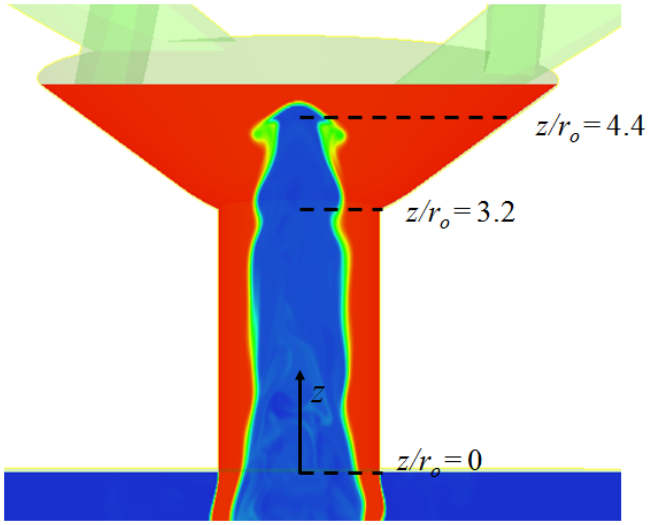

Figure 4.9: VOF distribution on a plane along the nozzle axis within the swirl chamber and the discharge hole and schematic of planes perpendicular to the injector axis where the velocity profiles were extracted for case 1 listed in Table 4.1.

The axial velocity profile at $z/r_o = 4.4$ presents two velocity peaks revealing a recirculation field. The first flow stream is located close to the air-core and it has a higher value than the second one, located near the wall. From the observation of the flow field and the streamlines plotted in Fig. 8 it can be inferred that the latter peak (the one close to the wall) is associated to the jet flow coming from the inlet swirling channels, while the peak located close to the air-core is connected to the presence of a top wall flow, which feeds the air-core streams, meaning that a part of the liquid entering in the swirl chamber is forced radially inward due to the presence of the swirl chamber top wall.
This can be better understood observing the vector map on a cross sectional plane shown in Figure 4.11: at the swirl chamber top the stream parallel to

the wall moves towards the chamber axis, at the interface with the air core the flow is forced to move down, increasing consequentially the axial velocity component. Also the characteristic mushroom shape of the air core close to the top wall is caused by the interaction with the flow moving downward with the recirculation of the jet from the inlet channels, which indicates a radial inward fluid motion.

The two above described axial velocity peaks remain visible up to the entrance into the cylindrical exit hole (section at $z/r_o = 3.2$), where the flow tends to acquire the classical structure of a confined vortex as described by Escudier [18], as show for the axial velocity profile at the exit section ($z/r_o = 0.0$). The same results for the axial velocity profile have been found by Donjat and Estivalezes [13], in their experiment made with LDA and PIV techniques on a large scale pressure swirl atomizer with a classical geometry, and also by Madsen et al. [50] with experiments and simulation made on a large scale pressure swirl atomizer with a geometry similar to that investigated in this work. The swirl velocity profile at $z/r_o = 4.4$ shows the presence of the Rankine combined vortex structure (as found by Donjat and Estivalezes [4]), with one significant peak close to the wall, which is connected to the inlet configuration investigated here. This phenomenon disappears in the velocity profiles extracted in the other two planes, confirming the strong influence of the inlet flow in the first part of the swirl chamber, with an intense dissipation as the flow moves downward along the injector due to combined effect of frictional losses and change of section. The comparison of the results obtained with different turbulence models reveals that the LES and the RNG $k-\epsilon$ models predict similar flow fields, with respect to the RSM model, and this observation is also confirmed from the average value of the fuel velocity components at the three sections under investigation, as reported in Table 4.5. At the discharge hole exit ($z/r_o = 0.0$) the difference among the LES and RNG results reaches 20% only for the radial velocity, that has a rather small magnitude, while for the axial and the swirl velocities the difference is always less than 10%.

z/r_o		4.4	3.2	0.0
u_{axial}/u_o	LES	0.203	0.546	1.713
	RNG $k-\epsilon$	0.164	0.507	1.745
	RSM	0.184	0.508	1.541
u_{radial}/u_o	LES	0.141	-0.032	-0.194
	RNG $k-\epsilon$	-0.114	-0.186	0.241
	RSM	-0.077	-0.151	0.153
u_{radial}/u_o	LES	1.257	1.967	1.241
	RNG $k-\epsilon$	1.333	2.161	1.339
	RSM	1.203	1.973	1.056

Table 4.5: Mean velocity components at different planes along the injector axis, predicted by the numerical simulations using three turbulence models.

4.6 Turbulent properties at the exit section of the atomizer

In addition of the velocity and pressure profiles over the radius at the exit section of the atomizer, the turbulence characteristics are necessary to properly evaluate the jet break-up. To investigate this phenomenon, the value of the turbulent kinetic energy k_t and dissipation rate ϵ_t can be used to evaluate the turbulent fluctuation of all the properties. With the RNG $k-\epsilon$ and RSM these values can be extracted directly from the numerical simulations at the exit section of the atomizer, while for the LES they are evaluated adopting the Huh and Gosman model [35]: this model has been adapted to evaluate the initial turbulence characteristics of an hollow cone spray (see Tonini et al. [85]). From this model, the values of k_t and ϵ are evaluated as follows:

$$k_t = \frac{\Delta P_{hole} d_o}{8 \rho_l l_o} \tag{4.3}$$

$$\epsilon_t = K_\epsilon \frac{\Delta P_{hole} u_{axial}}{\rho_l l_o} \tag{4.4}$$

where K_ϵ is a constant parameter set equals to 1 and u_{axial} is the axial liquid velocity at the exit section of the atomizer. In Table 4.6 the values of k_t and ϵ extracted from the simulation performed with the RNG $k-\epsilon$ and RSM turbulent model for case 1 are reported: these values are also compared with the values predicted by the Huh and Gosman model [35] model for the LES on the same case. Both the turbulent parameter k_t and ϵ assumes different values for the three investigated turbulent models. However, comparing the turbulent intensity defined by Eq. 4.5 (where V represents the absolute liquid velocity magnitude at the exit section of the atomizer), it can be noticed that the RNG $k-\epsilon$ and the LES are in good agreement, while the RSM predicts an higher turbulent intensity, which explain the higher value of $2h_\alpha$ defined previously.

$$TI = \frac{\sqrt{2/3k_t}}{\overrightarrow{V}} \tag{4.5}$$

Turb. Model	$\epsilon[m^2/s^3]$	$k_t[m^2/s^2]$	TI [%]
RNG $k-\epsilon$	6.58e6	18.08	13.88
RSM	1.28e6	23.02	18.48
LES	3.61e6	14.01	13.12

Table 4.6: Liquid turbulent properties at the exit section of the atomizer for the three turbulent model adopted for case 1 listed in Table 4.1.

In Table 4.7 the value of the turbulent properties for four operating conditions investigated with LESs are reported. These data will be adopted to investigate the following jet break-up.

Case	$\epsilon_t[m^2/s^3]$	$k_t[m^2/s^2]$	TI [%]
1	3.61e6	14.01	13.12
3	5.39e6	18.01	12.82
5	4.57e6	22.37	12.53
6	3.61e6	15.99	13.12

Table 4.7: Liquid turbulent properties at the exit section of the atomizer for 4 cases listed in Table 4.1; all the data are evalueted from LES simulations.

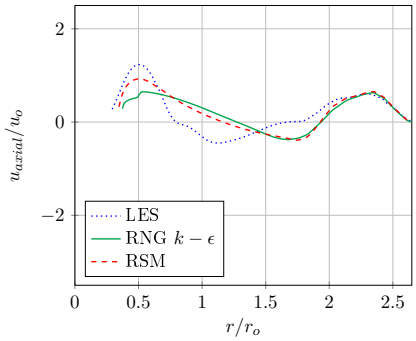

(a) Axial components - $z/r_o = 4.4$

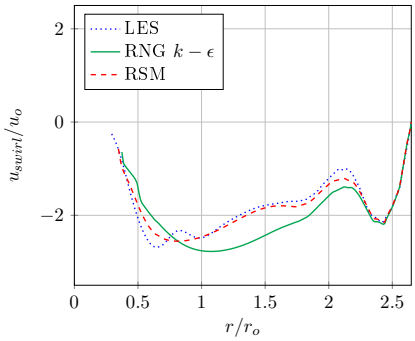

(b) Swirl component - $z/r_o = 4.4$

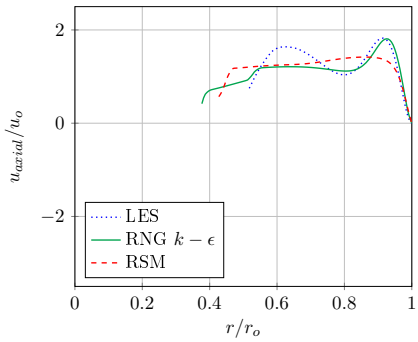

(c) Axial component - $z/r_o = 3.2$

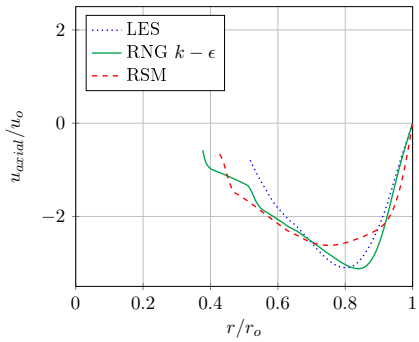

(d) Swirl component - $z/r_o = 3.2$

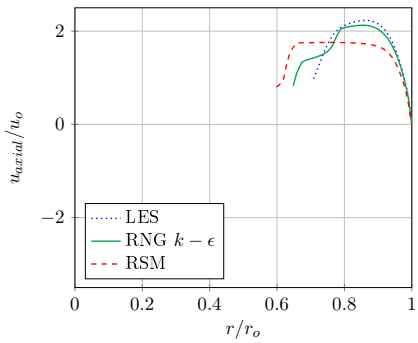

(e) Axial component - $z/r_o = 0.0$

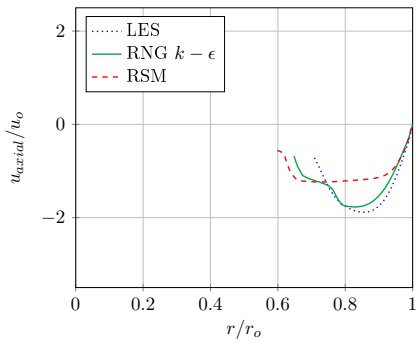

(f) Swirl component - $z/r_o = 0.0$

Figure 4.10: Radial profiles of axial(picture (a), (c) and (e)) and tangential (picture (b), (d) and (f)) velocity components at $z/r_o = 4.4$, $z/r_o = 3.2$ and $z/r_o = 0.0$.

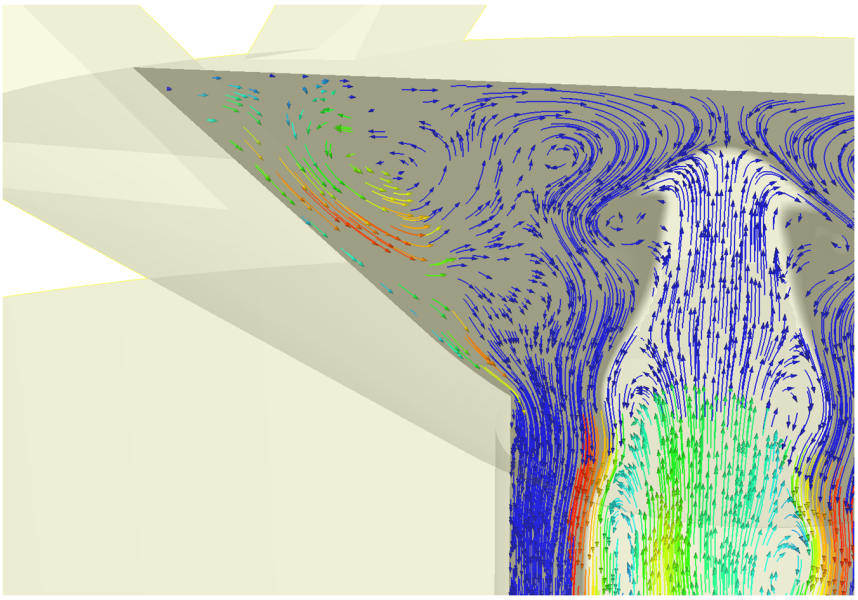

Figure 4.11: VOF distribution and flow vector map on a plane along the nozzle axis within the pressure swirl atomizer; test case No. 1 of Table 4.1.

Chapter 5

Conical swirled jet development and the subsequent primary break-up

5.1 Introduction

The analysis of the internal nozzle flow is aimed to evaluate all the initial characteristics of the conical swirled jet. Indeed, all the atomization models require the informations of the liquid lamella thickness at the exit section of the atomizer, its swirl velocity components and other informations linked to the perturbation waves. The latter one can be connected to turbulence phenomena or to the waves that move over the air-core interface (precession and helical waves). Most of the models, simplify the initial information and reduce all the results to averaged value with similar physical property of the realistic spatial trend. Although these models are very easy to use to define the break-up informations of the investigated jet, experimental data are not available to validate them.
Numerical simulations can be used to evaluate the jet behaviour after the injection upto its break-up and subsequent droplet production (primary

spray). This can be done only if the simulation is able to reproduce the real jet behaviour, without any model (adopted to simplify the calculations and the represented physics): this must be true not only for the turbulent or laminar nature of the flow, but also for the knecking phenomenon between different liquid structure, as the rupture of the ligaments in several smaller droplets. For all this reasons, in this chapter the investigations on the primary break-up on a conical swirled jet obtained by multiphase Direct Navies-Stokes Simulations (DNS) are presented, where the only limit to capture the whole behaviour of the jet is linked to the grid size. All the simulation are performed with the in-house Free Surface 3D (FS3D) solver [19].

5.2 Mathematical modeling

FS3D is a finite volume DNS solver able to track the position of the liquid phase and its interaction with the gas phase. Therefore it integrates directly the Navier-Stokes equations for incompressible two-phase flows with arbitrary free surfaces. Detailed information about the implementated numerical schemes are given by Rieber [65]. The incompressible flow is governed by the conservation equations for mass and momentum:

$$\frac{\partial \rho}{\partial t} + \nabla \bullet (\rho \overrightarrow{u}) = 0 \tag{5.1}$$

$$\frac{\partial \rho \overrightarrow{u}}{\partial t} + \nabla \bullet (\rho \overrightarrow{u}\,\overrightarrow{u}) = \nabla \bullet [S - IP] + \rho \overrightarrow{k} + f_\gamma \tag{5.2}$$

where $\overrightarrow{u}$ denotes the velocity vector, t the time, ρ the density and P the pressure. $\overrightarrow{k}$ denotes the external body force vector, such as gravity, while S represents the stress tensor equals to:

$$S = \mu \left[\nabla \overrightarrow{u} + \nabla \overrightarrow{u}^T\right] \tag{5.3}$$

To solve correctly the system of equation for two immiscible fluids, the capillary force acting on the interface between them must be evaluated: the last term in Eq. 5.2 f_γ represents the influence of the surface tension in the proximity of the liquid surface, and it is handled as a volume force that acts on every cell containing the interface [4]. The velocity discretization has been implemented in a staggered arrangement, in according with the Marker and Cell (MAC) method [29]: therefore scalar variable are evaluated at cell centers, while the velocities are evaluated at the cell faces.
To track the position of the liquid and the gas, the multiphase volume of fluid (VOF) [31] method has been implemented: it introduces an additional indicator variable α which represents the volume fraction of liquid inside each cell and it change as already explained in chapter 4, and re-presented here:

$$\alpha(\mathbf{x},t) = \begin{cases} 0 & \text{outside the liquid phase,} \\ ]0,1[& \text{at the interface,} \\ 1 & \text{inside the liquid phase.} \end{cases} \tag{5.4}$$

The value of the density and the dynamic viscosity for both the phases remain constant during the simulation; in each cell the value of this two variables must be calculated depending from the presence of the liquid. Therefore, adopting the value of the variable α into the cell, they are defined as follows:

$$\rho\,(x,t) = \rho_g + (\rho_l - \rho_g)\,\alpha(x,t) \tag{5.5}$$

$$\mu\,(x,t) = \mu_g + (\mu_l - \mu_g)\,\alpha(x,t) \tag{5.6}$$

where the subscripts l and g represent the liquid and the gas phase respectively. For the phase variable α, an additional transport equation is introduced:

$$\frac{\partial \alpha}{\partial t} + \nabla \bullet (\overrightarrow{u}\alpha) = 0 \tag{5.7}$$

The flux of the above equation is calculated using the method of piecewise linear interface reconstruction (PLIC) [64], which reconstructs the sep-

arating plane between the two phase inside the interface cells. This plane is defined to be orthogonal to the local normal $\widehat{n}_\gamma$ of the interface, which is equal to the negative gradient of the α variable.

Equations 5.1 and 5.2 are solved simultaneously to provide the velocity field. A second order upwind scheme is adopted to discretize the convective terms, while second order accurate central difference discretization scheme is used for the diffusive terms. For the time integration, a first-order explicit Euler scheme is adopted and the maximum time step sizes are restricted by the Courant-Friedrichs-Lewy (CFL) condition [30] (value of CFL limit equal to 0.5). After each time step, the pressure field is defined by using the Poisson equation. For more detailed information about the FS3D solver, see Eisenschmidt et al. [19].

5.2.1 Grid generation

To correctly perform a Direct Numerical Simulations, the most important aspect to evaluate is the grid size: this value must be close to the smallest turbulent fluctuation related to turbulent phenomenon. This scale η_k can be evaluated following the Kolmogorov's theory [84]:

$$\eta_k = \frac{L_t}{Re_t^{3/4}} \quad \text{where} \quad Re_t = \frac{\rho_l \sqrt{\overline{\vec{u}'}^2} L_t}{\mu_l} \tag{5.8}$$

where Re_t represents the turbulent Reynolds number, defined as a function of the largest turbulent fluctuation L_t and the turbulent velocity fluctuations $\sqrt{\overline{\vec{u}'}^2}$. The latter one has been estimated at the atomizer exit section from the previous internal nozzle flow simulations, which results are reported in section 4.6.

The value of L_t can be estimated considering the geometric characteristics of the phenomenon under investigation, as it is the pipe diameter for a confined flow. For all the investigated cases, the value of L_t is imposed to be equal to $2h/10$.

Build a grid which has a cell size equals to η_k yields to drastically increment

the numerical effort, and therefore a grid with larger cell size is preferred. To evaluate how far is the grid generated from the smallest length scale of the phenomenon under investigation, the Kolmogorov factor KF has been defined, which represents the ratio between the cell size η_c with the smallest turbulent length scale η_k:

$$KF = \frac{\eta_c}{\eta_k} \tag{5.9}$$

Increasing the value of KF yields to lose the information of the turbulent scales between the smallest scale upto the grid size: the effect of this filtering on the turbulent fluctuations is related to the energy lost. Typically, the energy spectrum of turbulence shows a low energy content at the smallest scales, and therefore their filtering do not influence the main aspects of the simulations. In literature several authors suggested that imposing the grid size resolution equals to the Kolmogorov lenght scale it is a too stringent condition (like Moin and Mahesh [53]): in Table 5.1 a list of DNS investigations made in the past can be found, with the value of the KF adopted along different spatial direction, which have a good agreement with the experimental data. These authors stated that a grid with KF higher than one can be adopted, and it must be able to take into account the first and second order of turbulent statistics to properly capture most of the dissipation.

Flow	KF		
Curved channel [55]	$z = 3.75$	$r = 0.13$	$\theta = 11.25$
Plane channel [39]	$x = 7.50$	$y = 0.03$	$z = 4.40$
Boundary layer [79]	$x = 14.30$	$y = 0.33$	$z = 4.80$
Homogeneus shear [71]	$x = 7.80$	$y = 3.90$	$z = 3.90$

Table 5.1: Resolution used in spectral simulations of some homogeneus and wall bounded flows.

As it can be understood, the maximum value of KF depends on the energy spectrum of each case: for example, from the work of Moser and Moin

[55] the most of the dissipation in the curved channel occurs at scales greater than $15\eta_k$ (based on average dissipation); Gorokhovsky and Hermann [25] suggested that to correctly estimate the primary break-up of of a liquid jet, the maximum value of KF which characterize the grid resolution, is equal to 10. Therefore, a specific investigation must be carried out to properly simulate the phenomenon under investigations.
For the jet break-up investigation, the Kolmogorov length scale is not the only dimension that must be take into account: indeed to properly evaluate the detachment of a liquid ligaments from a main jet body, and then its sub-sequent break-up into droplets, the grid must small enough to follow the thinning of the liquid connection between the initial liquid bodies. The dimension of the cell for this case must be order or magnitude lower than η_k ($KF << 1$), which yields to increase simulation CPU time and computational resources. To avoid this increment of the calculation effort, different authors introduced a pinching models able to reproduce the realistic break-up behaviour for specific jet (see Gorokhovsky and Hermann [25] for more detail). However, the limit imposed by the Kolmogorov length scale is often enough to properly investigate the break-up process, obtaining at the end a simulation with affordable numerical effort and without using any break-up models which can induces to a different evaluation of the spray production. This strategy has been adopted in the present work to investigate the primary break-up of a conical swirled jet; however, a grid dependence study has been carried out to evaluate the influence of the grid on the spray characteristics, as shown in section 5.4.1.

5.2.2 Geometry and boundary conditions

A rectangular domain has been adopted: the inlet boundaries are located at the center of the left side domain, while the remaining parts of the left side are set as no-slip wall. A continuous (Neumann) boundary condition is chosen for the other sides of the domain as can be seen in Figure 5.1. The dimension are as follows: 10.5 times the nozzle diameter d_o along both the directions of the nozzle plane (y and z) and $7.5 \times d_o$ in the axial direction of the jet (x). 2 or 4 additional diameter are located on the y and z direction

to avoid any influence of the boundary condition on the jet development. Due to the presence of the jet in the central part of the yz plane (coloured in dark gray in Figure 5.1), the cell size respects the value of the desired KF to properly follow the jet development and break-up; in the outer domain (coloured in light gray in Figure 5.1), a coarser grid is present to not excessively increase the computational effort. Along the axial direction (x) the grid is keep constant and uniform.

Figure 5.2 shows the joint of the atomizer geometry investigated in the previous chapter, with the geometry adopted for the investigation of the conical swirled jet break-up. For this analysis, a parallelepiped geometry has been preferred to properly generate the hexahedral grid with the desired dimension with high quality (no high distortion or skewness level). For the cell generated in the internal region (coloured in green), the cells aspect ratio has been taken higher than 0.9.

To properly follow the swirled jet development, an annular inflow has been generated where the liquid enters into the domain with the velocity components extracted from the previous LES simulations at the exit section of the atomizer (chapter 4). Due to low pressure generated along the atomizer axis as consequence of the internal vortex, the environmental gas rises up to the top wall of the swirl chamber: for this reason, in the circular region within the annular liquid inflow, the gas velocity components has been imposed, representing the air-core development. Due to the negative axial velocity components of the gas, the latter boundary can be approximately to an outflow. The final inlet region of the jet is resumed in Figure 5.3.

Commonly, the simplified models adopted to evaluate the conical swirled jet development and its subsequent break-up require the averaged value of the liquid velocity components. However, the effect of this simplification is not clear, and further investigations must be carried out. Therefore a comparison on the atomization process is performed imposing the velocity profiles extracted from the internal nozzle flow simulations and their averaged values. In Figure 5.4 the velocity profiles of all components are reported for both phases, together with the corresponding averaged values, for the case 1 listed in Table 4.1.

From the picture (a) of Figure 5.4 it can be noticed the averaged value

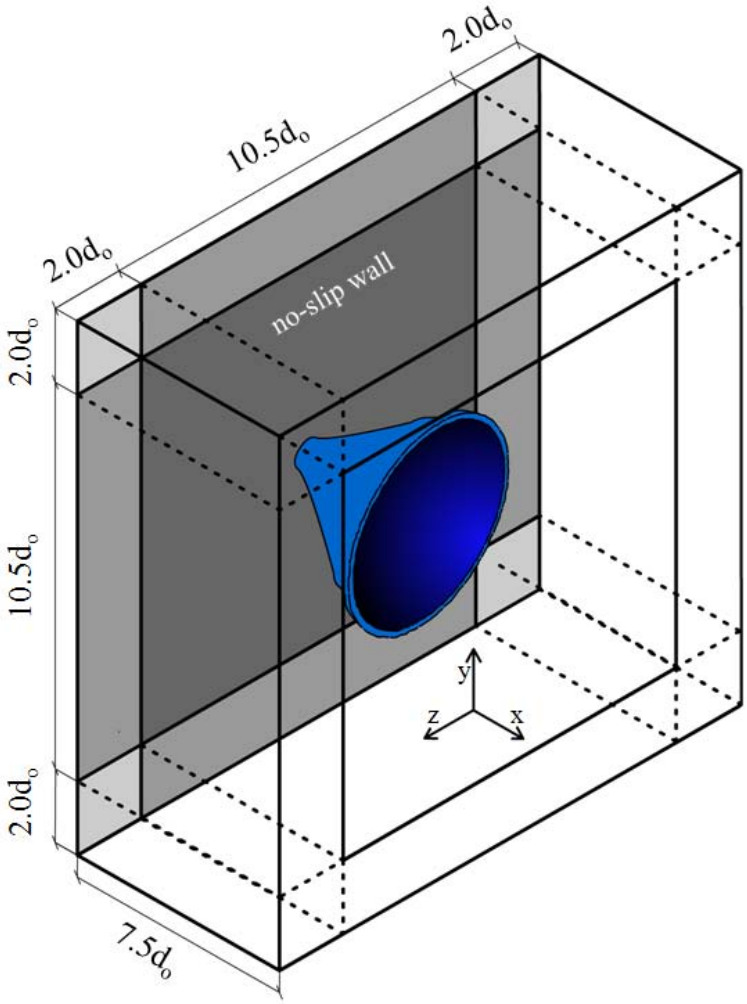

Figure 5.1: Total geometry adopted for the DNS investigations.

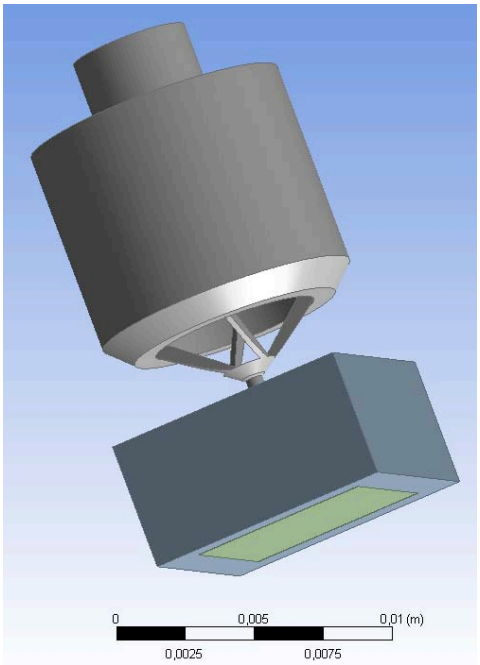

Figure 5.2: Combined geometry of the LES/RANS simulation of the internal nozzle flow in grey, and the geometry adopted to evaluate the jet developement into the combustion chamber: the green region represents the core of the geometry where the grid respect the value of the desired KF, while the blue part represents the additional region, where the coarser grid is present.

of the gas axial velocity component is close to zero, as expected, due to the balance of the gas mass within the atomizer. Indeed, the air entrainment, induced by the vortex motion, forces the gas to rise within the nozzle up to the top swirl chamber (negative value of the axial velocity component); after that, the air starts to move together with the liquid motion until it exits from the nozzle. For all the components shown in Figure 5.4 the presence of boundary layer between the liquid and the atomizer wall, and between the two phases, can be noticed.

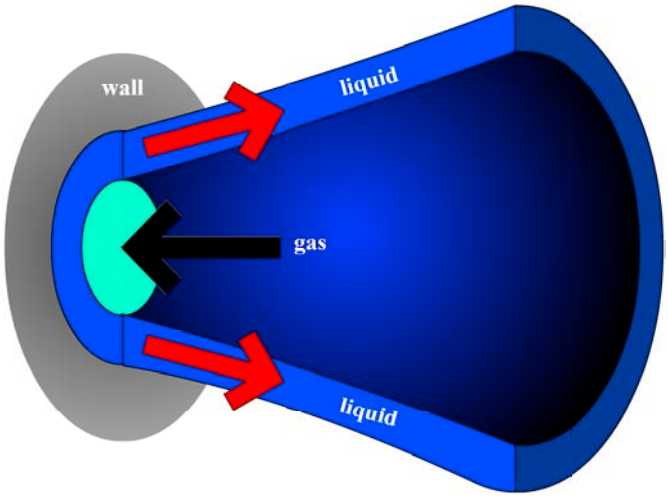

Figure 5.3: Topology of the inlet boundaries showing the annular nozzle injecting the liquid and the backflow region in the center surrounded by a no-slip wall.

5.2.3 Turbulent inflow

In section 4.6 the turbulent properties of the flow are extracted directly from the numerical simulations (from RANS) or are estimated (for LES) in such a way to define if the emerging conical swirled jet is turbulent or not. The information of the Turbulent Intensity (or the turbulent kinetic energy) is really important to properly generate the grid as shown in section 5.2.1, because with it the turbulent Reynolds number Re_t can be estimated. The information of the turbulent characteristics of the flow can be also adopted to generate a turbulent inflow: indeed, if the velocity profiles (uniform or not) are set as inlet boundary as they are shown in Figure 5.4, the inflow is considered laminar. Into the FS3D a synthetic inhomogeneous turbulent fields with prescribed autocorrelation functions (Kornev and Hassel [42]) has been implemented to generate a properly turbulent inflow. This algorithm has been validated on the classical round jet at different Reynolds numbers, but not for the conical swirled jet investigated in this work.

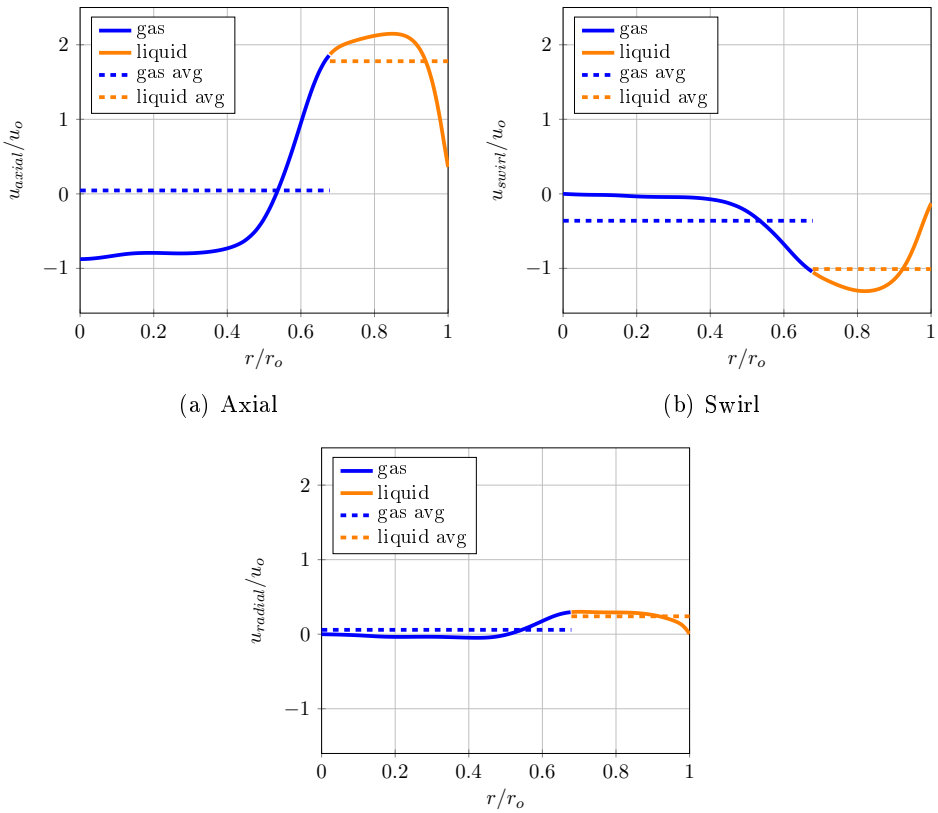

(a) Axial

(b) Swirl

(c) Radial

Figure 5.4: Velocity components profiles for both the liquid and gas phases for the case 1 listed in Table 4.1: the solid lines represent the realistic profiles extracted from the previous LES simulation, the dashed lines represent the corresponding averaged values and the the points are the value adopted into tor reproduce the realistic inlet flow into the FS3D.

Therefore, no turbulent fluctuations are imposed on the inlet flow field, and only laminar inlet profiles are considered.

5.3 Primary break-up informations

From DNS, different macro-parameters can be extracted to characterize the break-up process: the break-up length L_b and the spray characteristic (probabilistic size distribution and characteristic droplet diameter). Their definition are reported in the following paragraph.

5.3.1 Break-up lenght L_b

The break-up length represents the axial distance from the injection point where the liquid jet starts to break and the primary spray is formed. This distance can be directly measured from the simulations and it can be compared with the simplified linear break-up analysis present in literature.
This lenght can be defined differently depending on the characteristic of the jet that is take into account. In this work, two different methodologies have been adopted to evaluate L_b: the first consists to define the axial distance where the first hole can be found on the liquid film ($L_{b,h}$); the second has been developed by Dumochel et al. [16] ($L_{b,s}$) and it consists to in evaluating at each axial distance the total surface of the liquid jet. In this way, starting from the injection point, the total surface of the jet must increase with the axial distance, due to the opening of the annular jet induced by the swirl motion; where the jet starts to break in to a smaller structure, the total jet surface decreases and vice-versa the spray surface increases: from the definition of Dumochel et al. [16], the break-up point is located in correspondence of the maximum value of the total jet surface (i.e. where the total jet surface gradient changes sign). Figure 5.5 shows the normalized value of local jet perimeter $P_j(x)$ along the axial direction, which has the same trend of the local surface $S_j(x)$ because $S_j(x) = P_j(x) \times dx$, where dx represents the cell size along the axial direction (constant value). To damp all the fluctuations present on the liquid surface on the estimation of this point, a moving average has been consider, using 21 consecutive points.

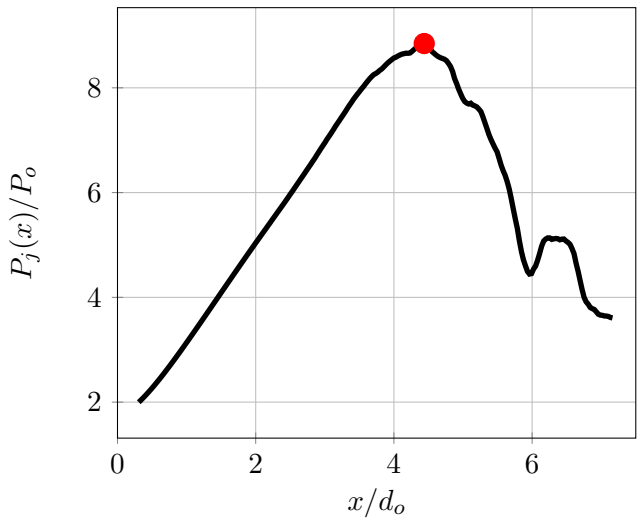

Figure 5.5: Normalized local value of the perimeter of the liquid interface, along the axial direction. The break-up lenght correspond to the x value where the $P_j(x)/P_o$ reaches its maximum value.

5.3.2 Droplets size

From the DNS, different droplet informations can be extracted. The main aspects to take into account are the droplet size distribution and the characteristic diameter. Generally, the latter one can be defined as follows:

$$D_{ab}^{a-b} = \frac{\int_{d_{d,min}}^{d_{d,max}} d_d^a p(d_d) d(d_d)}{\int_{d_{d,min}}^{d_{d,max}} d_d^2 p(d_d) d(d_d)} \tag{5.10}$$

where $p(x)$ is the probabilistic density function which provide a number of droplet with the specified diameter; d_d represents the droplet diameter, while $d_{d,min}$ and $d_{d,max}$ represent the minimum and the maximum diameter in the sample, respectively. The exponents a and b yield to define different aspects of the spray (see [48]), as the controlling of the droplets volume d_{30}

($a = 3$,$b = 0$), or the mass transfer for combustion process d_{32} ($a = 3$,$b = 2$). The latter one is also called Sauter Mean Diameter (SMD).

From experimental measurements, the probabilistic density function $p(d_d)$ is represented by a discrete function: the data are collected in a number of ranges i, which all the measured droplet diameters from $d_{d,min}$ to $d_{d,max}$ (histogram). In this case, Eq. 5.10 can be simplified:

$$D_{ab} = \left[\frac{\sum N_i d_{d,i}^a}{\sum N_i d_{d,i}^b} \right]^{1/(a-b)} \tag{5.11}$$

where N_i represents the number of drops in size range i and $d_{d,i}$ is the middle diameter of size range i. Therefore the SMD of a discrete distribution can be evaluate with Eq. 5.11, where $a = 3$ and $b = 2$.

The information of the droplet diameters d_d can be evaluated experimentally with different techniques, but the common used is the Phase Doppler Anemometry (PDA). It consist in a local measurement, over the time $t_{measurement}$; at the end of $t_{measurement}$ the collected data are processed to provide the characteristic droplet diameter. This procedure must be done for several points to cover a wider investigation area. From DNS, the evaluation of d_d has been done following a similar procedure of the PDA, but including the 3D informations of the spray: a plane normal to the jet axis is placed at different axial position (x): only the droplets which pass trough this plane during evaluation time, are take into account to define the characteristic diameter, as shown in Figure 5.6.

The droplet informations which can be extracted from the DNS are not only the droplet dimension d_d, but also their 3D position (particularly radial position) and deformation can be evaluated. The latter aspect represents the most crucial aspect that limits the use of laser Doppler measurement to define the primary spray drops size: droplets with high level of deformation are filtered from the acquisition system, and only spherical (or close to be) droplets are considered. In this region, the level of deformation is relatively high and then from PDA measurements the signal is affected by an high level

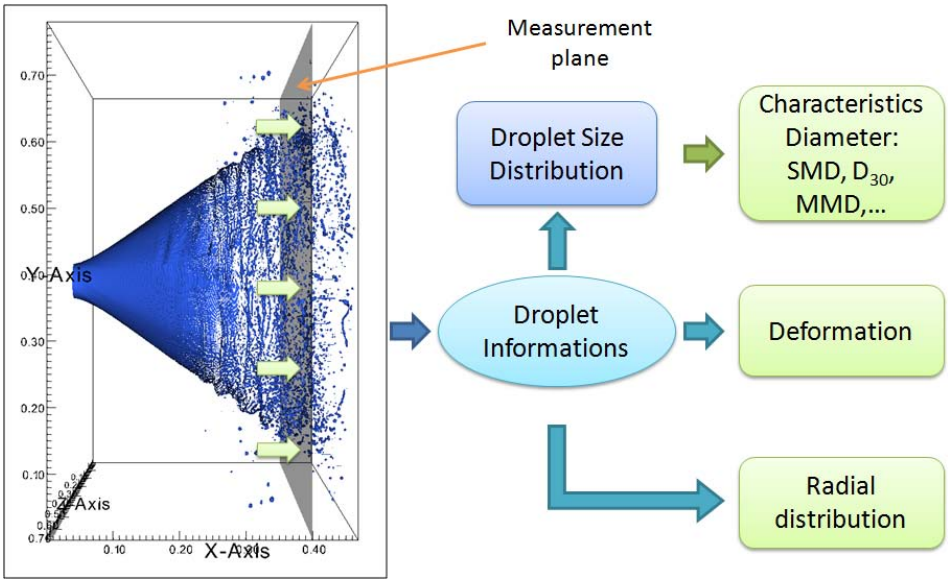

Figure 5.6: Methodology adopted to measured the droplets informations.

of filtering, which yields to not properly catch all the spray characteristics. For the simulation data, the effect of the deformation has been take into account considering all the liquid structures produced after the primary break-up as a prolate ellipsoid: the deformation, or Aspect Ratio AR, is defined as the ratio of the major axis A_e and the minor axis a_e (see Eq. 5.12). They are defined as the minimum and the maximum distance of the liquid structure surface from its center of gravity, as it can be observed in Figure 5.7.

$$AR = \frac{A_e}{a_e} \tag{5.12}$$

Together with the AR parameter, the liquid structure volume V_{ls} is considered to characterize the spray. In particular, if the liquid structure

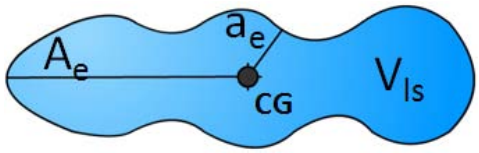

Figure 5.7: Generic liquid structure representation after the jet's break-up: CG is the center of gravity; V_{ls} is the liquid structure volume, while A_e and a_e representing the maximum and the minimum distance from the surface to the center of gravity respectively.

is a droplet, its diameter d_d can be evaluated approximating the liquid structure to a sphere:

$$d_d = \sqrt{\frac{6V_{ls}}{\pi}} \tag{5.13}$$

Otherwise, if the liquid structure is a ligament, its diameter $d_{L,DNS}$ can be evaluated approximating the liquid structure to a cylinder with the same value of AR and V_{ls} of the original liquid structure:

$$d_{L,DNS} = \sqrt[3]{\frac{4V_{ls}}{\pi AR}} \tag{5.14}$$

The sensitivity analysis performed assumed that all the liquid structures with $AR \leq 5$ can be approximated to droplets, while for $AR > 5$ can be considered ligaments.

5.4 Preliminary tests

5.4.1 Grid dependence study

As explained in section 5.2.1, the grid size is one of the main crucial issues for the DNS investigations on the conical swirled jet break-up. Therefore, case 1 listed in Table 4.1 has been investigated with 5 different grids with different size, and consequently different KF, imposing the uniform inlet

profile extracted from the RNG $k-\epsilon$ simulation of the internal nozzle flow. In Table 5.2 the characteristics of the five investigated grid are reported, in terms of Kolmogorov Factor, cell size and the total number of elements.

KF	$dx[\mu m]$	$dy, dz[\mu m]$	No. of cells [Mln]
6.56	7.32	8.55	$\approx$ 671.09
7.65	9.16	8.55	$\approx$ 536.87
8.19	9.16	9.32	$\approx$ 301.99
9.18	12.21	10.25	$\approx$ 226.49
10.93	12.21	13.67	$\approx$ 100.66

Table 5.2: Kolmogorov Factor, cell size and total amount of elements of the investigated grids.

All the performed simulations do not start from an already developed jet, but they simulate the initial transitional regime until the quasi-steady state solution is reached. Figure 5.8 shows the 3D jet surface for the finer and the coarser investigated grids at 0.1 ms after the start of the simulation: at this time the first rupture of the conical jet during its development into the domain can be seen and it can noticed that if the grid becomes coarser, the annular ligaments produced have different size and numbers: for $KF = 6.56$ there are 3 ligaments, one closer to the tip of the jet that is already breaks-up in smaller structures, while higher values of KF the number of ligaments decreases to one. This result shows that from the beginning of the simulation, the coarser grid induce to a coarser atomization.

Figure 5.9 shows the results obtained at 0.3 ms after the starts of the simulation for the grid with $KF = 6.56$ and $KF = 10.93$, where it can be noticed that the primary spray is already formed. The result obtained with the finer grid shows the presence of the jet more forward after the injection point respect the coarser cases, where there are thicker ligaments and large droplets closer to the inlet due to a earlier break-up. Moreover, for the finer case some perturbations moving over the liquid surface can be noticed, which yield to the lamella break-up; in the coarser case, no

(a) $KF = 6.56$ (b) $KF = 10.93$

Figure 5.8: Conical swirled jet at 0.1 ms with the two extreme investigated grid (finer and coarser).

fluctuations are visible and the droplets seem to be produced only by the numerical diffusion.

To quantify the effect of the grid resolution on the simulations, the break-up length L_b and the values of SMD and d_{30} (measurement plane located at $6.4d_o$ after the injection point) have been extracted and shown in Figure 5.10. The value of L_b evaluated with both the methodologies explained in section 5.3.1 are shown in picture (a): the break-up length remains almost constant for grid with $KF < 9$ (difference with the case at $KF = 6.56$ lower than 10%), while for the higher values the jet starts to break-up always closer to the injection point. This is connected to the faster thinning of the liquid film connected to a bad description of the flow. Also for the primary spray characteristics diameters (see picture (b)), it can be noticed that they remain almost constant for $KF < 9$, while for higher values, the spray is characterized by larger droplets. This result is clearly connected to the numerical diffusion introduced by the grid, which yields

(a) $KF = 6.56$ (b) $KF = 10.93$

Figure 5.9: Conical swirled jet at 0.3 ms with the two extreme investigated grid (finer and coarser).

to produce a very high number of big droplets.

From this grid dependence analysis on the conical swirled jet tbreak-up process, it has been established that there isn't an appreciable effect on the estimation of L_b and on SMD for the cases where $KF < 9$. Therefore the successive analysis are conducted adopting a grid with a $KF \approx 8$ which represents the balance between the numerical effort and the realistic reproduction of the atomization process.

5.4.2 Influence of the velocity profiles

The effect of inlet boundary is investigated and discussed in this section. Indeed, as explained in section 5.2.2, two different inlet profiles were set: the profile extracted from the previous investigation of the internal nozzle flow or the corresponding averaged uniform value. The latter one is common used into the break-up model to evaluate the evolution of the an-

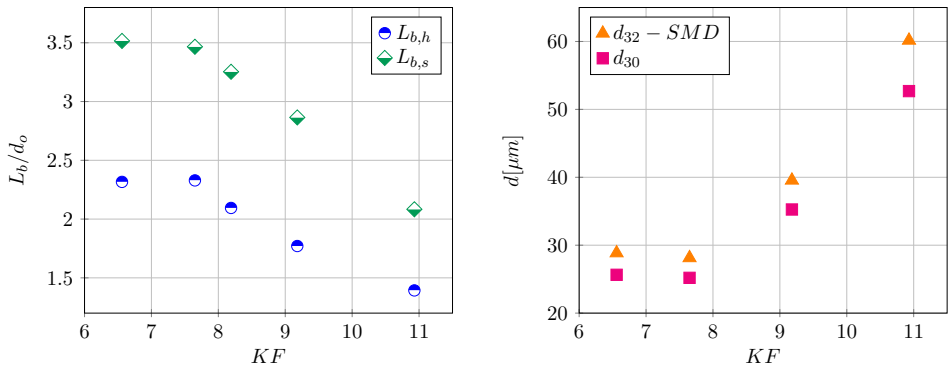

(a) Break-up length

(b) Characteristic diameter

Figure 5.10: Normalized break-up lenght (picture (a)) and characteristics diameter of the primary spray (picture (b)) variation with the KF.

nular liquid film until it breaks: the uniform velocity profiles have the same momentum information and they can be estimated with several simplified method. However, the effect on the atomization process is still unknown. Therefore, for case 1 listed in Table 4.1, both the inlet profiles are tested, adopting a grid with $KF = 8.4$.

Figure 5.11 shows the comparison for these two different simulations at 0.1 and 0.3 ms after the start of simulation. At 0.1 ms (picture (a) and (b)) it can be seen that the jet obtained with the realistic profiles penetrates more than the other case due to higher thinning of the annular film, which yields to have a finer tip of of the jet respect the other case, where the first ligaments are earlier produced. At 0.3 ms (picture (c) and (d)), the structure of the jet in a quasi-steady state condition is shown: the uniform profiles lead the jet to penetrate more before it starts to break; moreover, for this case, less droplets are produced which don't spread into the domain as for the other case. These differences are connected to the higher value of shear stress generated from the realistic profile inside the liquid film. Although there are these differences, in both the cases it can be seen a development of the perturbation which are moving over the liquid surface, in particular

in correspondence of the tip of the jet. This result suggests that in both the cases, the jet break-up is produced by the developing of unstable waves moving over its surface, but due to the different shear stress present into the liquid film generated as consequence of a different liquid internal velocity gradient, the final atomization result is different.

Table 5.3 reports the values of the break-up lengths: for both the cases the estimate value of L_b is always $\approx$ 15% higher for the uniform profile simulation respect the other case as expected.

	Uniform	Realistic
$L_{b,h}/d_o$	2.51	2.16
$L_{b,s}/d_o$	4.07	3.57
$d_{10}[\mu m]$	25.94	33.76
$d_{30}[\mu m]$	30.90	37.05
$d_{32}[\mu m]$	37.08	40.33
MMD $[\mu]$	21.56	32.21
No. droplets	929	2001
No. ligaments	638	1825

Table 5.3: Comparison of the break-up lenght L_b and SMD between the simulations with the uniform and realistic inlet profiles.

Considering the spray characteristics, Figure 5.12 shows the droplet size distribution for both the simulations, extracted on the plane located at 6.4 diameters after the injection point: as it can be seen, for the uniform inlet velocity profiles, there is a peak of droplet with diameter close to 18 μm, while for the non uniform inlet velocity profiles it can be noticed a bimodal distribution, with the first peak at 20 μm and the second at 35 μm. This difference on the droplet size distribution is directly connected to the different inlet boundary shape, which yields to a different atomization behaviour. Figure 5.13 shows the jet obtained imposing the uniform inlet velocity profiles at 0.3 ms after the start of the injection(quasi steady-state regime): in

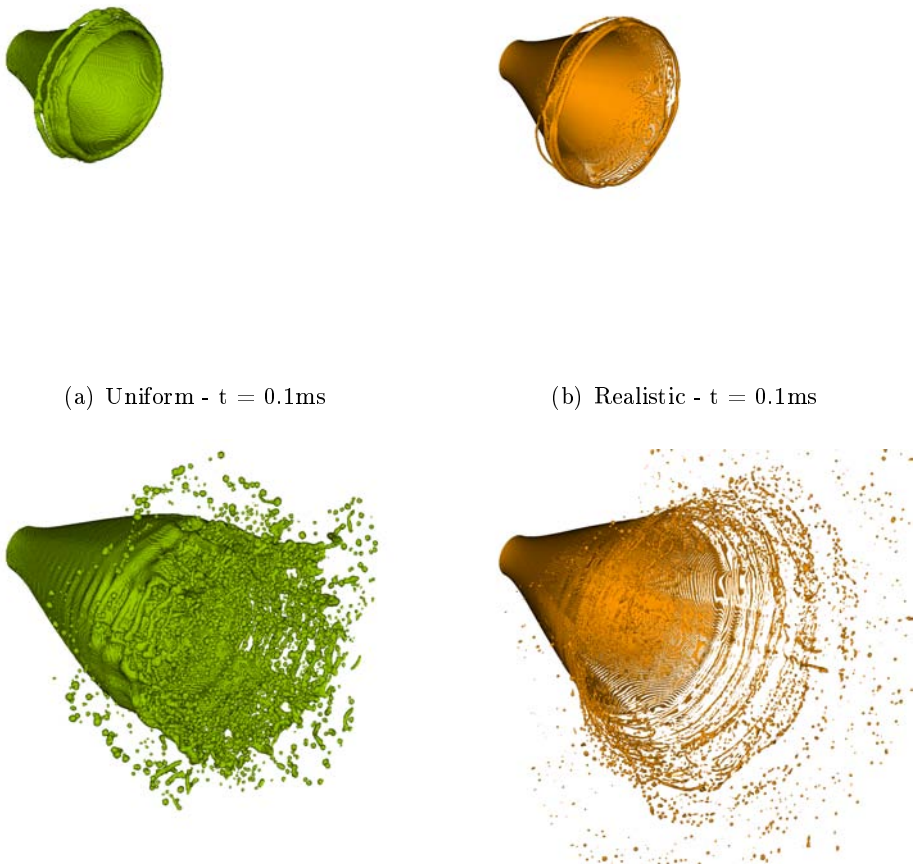

(a) Uniform - t = 0.1ms

(b) Realistic - t = 0.1ms

(c) Uniform - t = 0.3ms

(d) Realistic - t = 0.3ms

Figure 5.11: Comparison of the two investigated inlet velocity profiles, for case 1 listed in Table 4.1.

this picture it can be clearly identified that some ligament structures are produced as consequence of the perturbation moving on the liquid surface, but in some points some fingers liquid structures are present and connect

the "ligament" with the main body of the jet. This extended attachment of the ligament structure with the jet, shows the full break-up delay imposing the uniform velocity profile: as consequence, also these structures will delay their break-up into droplets.

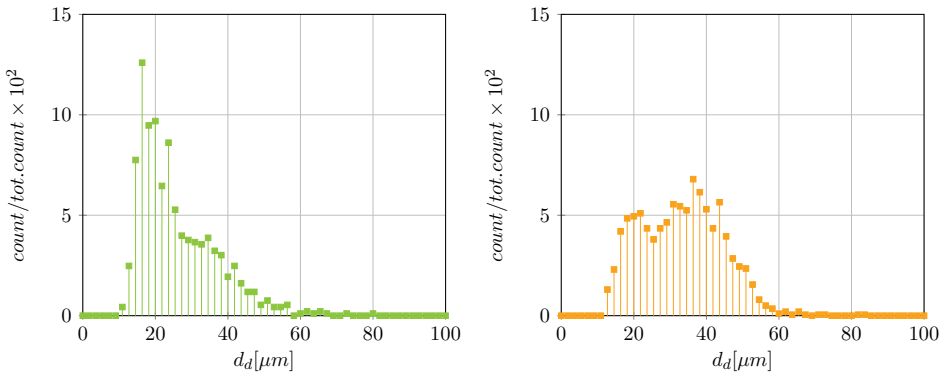

(a) Uniform inlet velocity profile (b) Realistic input velocity profile

Figure 5.12: Droplet size distribution obtained from the simulation where the uniform (picture (a)) and the realistic (picture (b)) inlet velocity profile is imposed.

Table 5.3 reports the resumed data of the investigated sprays for both the simulations with different inlet velocity profile: as it can be seen the characteristic diameters extracted ($d_{10}, d_{30}, d_{32} or SMD$) are in rather good agreement. The value of MMD extracted from the simulation with the realistic inlet velocity profiles is 49% higher, as consequence of the bimodal distribution of the droplet size observed in picture (b) of Figure 5.12. Table 5.3 also reports the number of droplets and ligaments used to provide the spray characteristics: as it can be noticed, the simulation with the uniform inlet velocity profiles yields to have a numbers of droplets and ligaments which are 54% and 65% lower than the total numbers extracted for the simulation with the realistic inlet velocity profiles imposed respectively. This result can further confirm the different atomization behaviour observed previously for the simulation with the uniform inlet velocity profiles.

At the end of this analysis, it can be concluded that the the realistic inlet velocity profiles must be preferred to correctly evaluate the atomization process for a conical swirled jet, even if the results obtained with the uniform inlet velocity profiles allow to get similar information of the characteristic diameter.

Figure 5.13: Zoom view of the liquid structure produced after 0.3 ms of simulation start for the case where the uniform profiles are set. Here it can be noticed that the ligament structure are produced regularly, but they remain also connected to the main body of the jet.

5.5 Comparison with analytical models

No available experimental data on the emerging jet, or the subsequent primary spray, for the specific atomizer under investigation can be found and used to check all the information that can be extracted from the 3D multiphase DNS performed in this work. However, in the open literature several analytical model evaluating some atomization steps, like the jet development, its break-up and the characteristics droplet diameter of the primary spray can be found.

5.5.1 Jet development

To evaluate the jet evolution before it starts to break, its development is compared with the model of Nonnenmacher and Piesche [57]. It requires the same input information adopted for the simulations, as the mean liquid velocity components, the liquid lamella thickness and the initial differential pressure between the liquid film surface, i.e. the difference of the injection chamber pressure with the air-core pressure. This model has been validated with experiments made with two different fluids (water and glycerine) and operating conditions: the comparison of the external jet position along the axial direction predicted by the model and the measured from the experiments shows a good agreement for a distance from the injection point less than 5 nozzle diameter ($x/d_o < 5$).
Figure 5.14 shows the comparison of the external jet profile (picture (a)) and liquid thickness (picture (b)) measured from the DNS with the data predicted with the model of Nonnenmacher and Piesche [57], for the case 1 listed in Table 4.1; the LES non uniform input velocity profiles have been adopted to perform the DNS calculation. The error bars plotted in both these figures, represent the standard deviation, evaluated considering the time fluctuations and the grid cell size error committed to define this quantities. As it can be seen, both the parameters are in agreement with the model, with an error lower than 5% upto $x/d_0 = 1.5$ (see picture (c)). At $x/d_o > 1.5$ an effect of the aerodynamic forces acting on the jet surface is present, due to the presence of a counter rotating vortex at the tip of the

jet, which can explain the difference on the prediction of the external edge, and consequentially on the liquid film thickness.

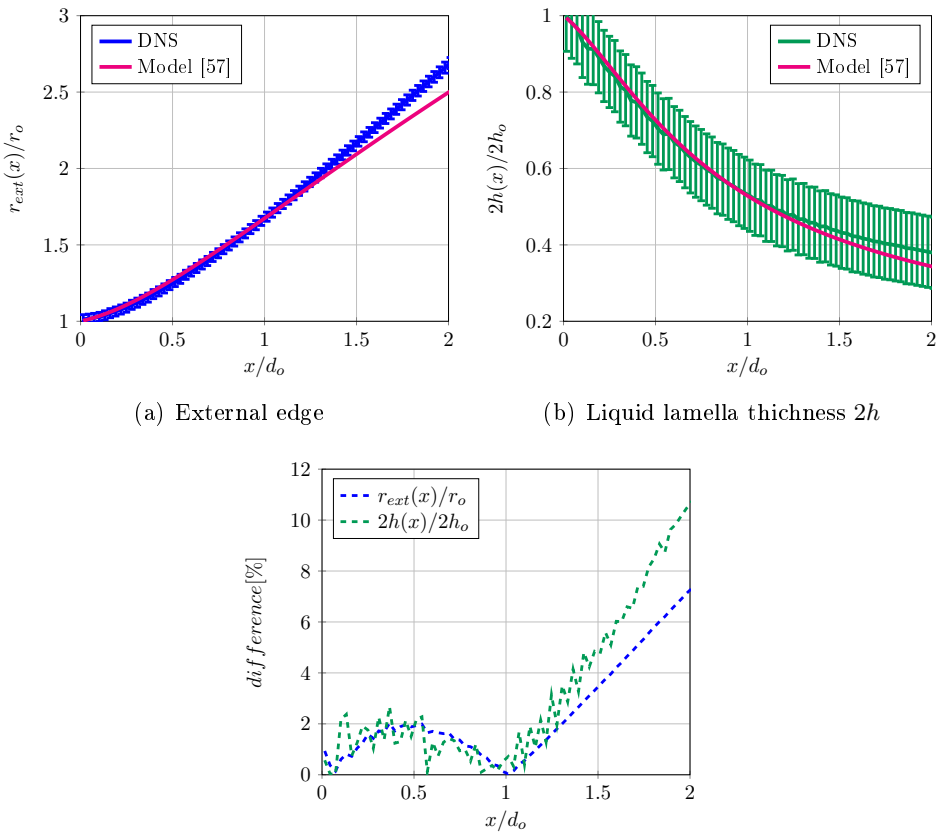

(a) External edge

(b) Liquid lamella thichness $2h$

(c) Variation from the model [57]

Figure 5.14: Comparison of the jet development evaluated with the Nonnenmacher and Piesche [57] and the measured data from DNS for case 1 listes in Table 4.1; picture (a) and (b) show the comparison in terms of external edge development and liquid lamella thickness along the axial direction, while picture (c) shows the variation of the numerical data from the analytical and validated model.

Another important parameter that can be evaluated from the jet development is the spray cone angle 2θ. Often, the half spray cone angle is preferred, and for this reason in the successive paragraph the results are expressed in term of θ. There are different definitions of this parameter that are connected to different characteristics of the jet. Figure 5.15 reports the value considering two different definitions adopted for the spray cone angle. The first definition represents the common used value of the spray cone angle and it is defined as:

$$\theta(x) = atan\left[\frac{r_{ext}(x)}{x}\right] \tag{5.15}$$

With this definition, the maximum aperture of the jet can be defined, and consequentially also the maximum spray spread.
Another definition used to evaluate the aperture of the jet consists to evaluate the local spray angle, i.e. considering the angular coefficient of the tangent line over the jet external profile:

$$\theta_{tan}(x) = atan\left[\frac{d\left(r_{ext}(x)\right)}{dx}\right] \tag{5.16}$$

If the jet continues to penetrates in the gas phase indefinitely, both the definitions must coincide:

$$\lim_{x\to+\infty} \theta_{tan}(x) = \lim_{x\to+\infty} \theta(x) \tag{5.17}$$

Figure 5.16 shows the variation of the half spray cone angle for both the adopted definition, together with the the value of θ obtained with the model of Nonnenmacher and Piesche [57] and the value of the spray cone angle predicted with the semi empirical correlation of Rizk and Lefebvre [69], which expression is reported in Appendix A.3. The values of θ measured from the DNS and the model of Nonnenmacher and Piesche [57] are in good agreement. Both the values of θ and θ_{tan} seems to reach an asymptote for high value of x. As it can be seen, the value of the half spray cone angle defined with the semi-empirical correlation of Rizk and Lefebvre [69], is

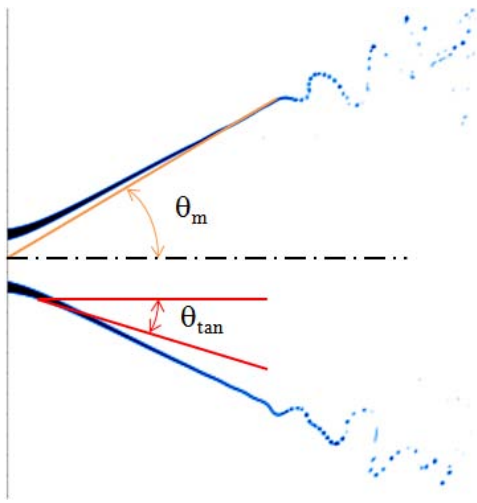

Figure 5.15: Definitions of the mesured half-spray cone angle θ.

in between the two definitions of θ. The latter definition is also in good agreement with the value of the spray cone angle defined considering the averaged velocity components of the liquid emerging from the nozzle:

$$\theta_{VR} = atan\left[\frac{\sqrt{u_{swirl}^2 + u_{radial}^2}}{u_{axial}}\right] \tag{5.18}$$

Often the value of u_{radial} assumes very low value respect the other two components, and then the definition 5.18 can be simplified considering only u_{swirl} and u_{axial}.
The last comparison between the value of θ_m and θ_{VR} shows that the spray cone angle obtained by the Rizk and Lefebvre [69] correlation, which is based only on the pressure drop across the atomizer ΔP, the geometry of the atomizer and the liquid properties, yields to indirectly estimate the correct velocity ratio as defined in Eq. 5.18.

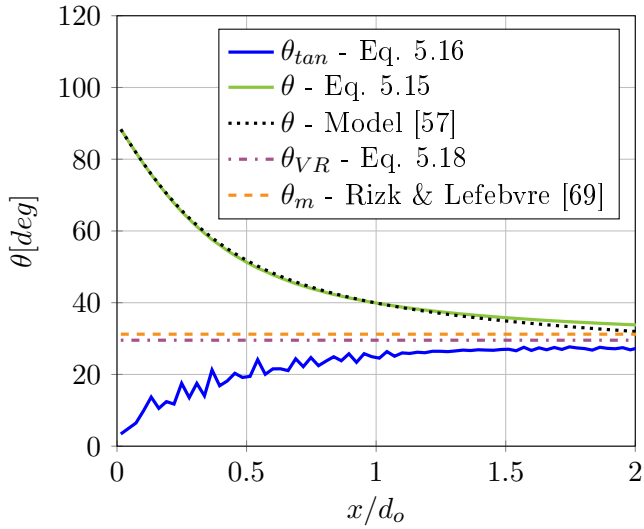

Figure 5.16: Variation of the spray cone angle accordig different definitions, along the axial direction; the value of θ_{VR} and θ_m are constant and not depend on the axial position.

The rather good agreement between the jet characteristics extracted from the DNS with the validated model of Nonnenmacher and Piesche [57] confirms the correct representation of the jet before its break-up.

5.5.2 Primary spray characteristics

All the DNSs results presented in this work have the aim to provide additional informations on the atomization process of a conical swirled jet. Therefore, every stage that composes the break-up must be compared with the experimental data. This procedure has been done indirectly previously for the jet development, however no experimental data are available on the investigated jet to compare the primary break-up process. In this section,

the data extracted from the simulations are compared with the model developed by Senecal et al. [75], which is also reported for a better comprehension in Chapter 3.
The model of Senecal et al. [75] allows to estimate the characteristics of the perturbation wave responsible of the lamella break-up. For all the cases reported in Table 4.1 the Weber gas number is always higher than 27/16 and the density ratio ρ_l/ρ_g is always less than 0.02: under these conditions only the short waves are expected to be present, and the simplified form of the viscous solution can be adopted. With this information, for case 1 listed in Table 4.1, the values of frequency ω_s and wave number k are defined and they are equal to 0.271 MHz and 1.74e5 m^{-1}, respectively, which correspond a period of 3.69 μs and a wavelength λ_b of 36.11 μm. The latter information can be used to properly define the grid size: indeed to capture the waves development over the jet, the grid cell size must assumes a dimension equal or lower than half of the wavelength, i.e. $L_c < 18.01\mu m$, according the Nyquist sampling theory. From the previous grid dependence study, the value of $KF \approx 8$ leads to have for case No. 1 a value of the cell size equals to 9.32 μm, which corresponds to $L_c \approx 1/4\lambda_b$: this result shows that the performed DNSs on the primary break-up are able to catch the behaviour predicted by the common analytical primary break-up models.
Figure 5.17 reports the comparison between the break-up information extracted from the DNS simulation of case 1, on a grid made with $KF = 8.4$, and the predicted values from Senecal's atomization model [75]. The following analysis has been done only for the sinuous mode, which is the only mode to be present for the investigated cases ($We_g > 27/16$). This result is also confirmed by the visualization of the 3D jet coming from the DNS, where only the antisymmetric waves can be recognized.

As it can be seen in Figure 5.17, the values of the break-up length are not in agreement, together with the following atomization parameters: the value $2h_b$ has been estimated imposing the the break-up length L_b in to the the Nonnenmacher and Piesche [57]; then with the information of $2h_b$, the ligament diameter, and the sub-sequent droplet diameter can be estimated. All these informations are compared with the corresponding measured values extracted from DNS.

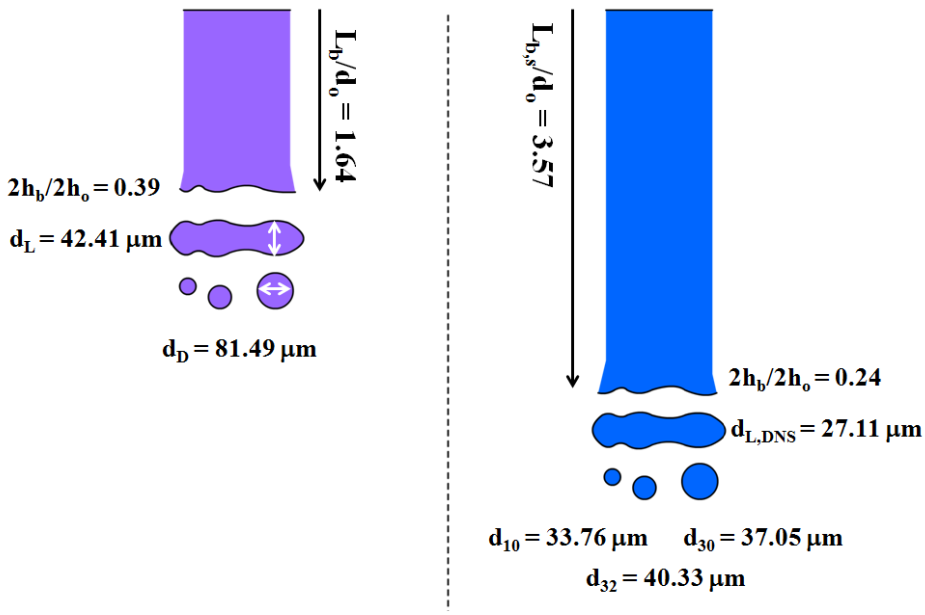

Figure 5.17: Comparison of the break-up characteristics obtained with the model of Senecal et al. [75] in violet, and the data extracted from the DNS in blue, for the case 1 in Table 4.1.

The value of $d_{L,DNS}$ is 38% lower than d_L, which is linked to the same variation on the values of $2h_b$, while the value of SMD is half of the droplet diameter predicted by the model d_D. All these differences are mainly connected to the estimated break-up length L_b which strongly depends from the initial model [75] assumptions: the first is the effect of the turbulence that is not take into account in any stages of the atomization process; the second is connected to the velocity input data, which is assumed to be constant and uniform. Moreover, the environmental gas is considered quiescent, which yields to increase the aerodynamic forces evaluated over the jet surface.
Although there are these differences, some similarities can be found considering non-dimensional parameters which are the ratio $d_L/2h_b$ and d_D/d_L,

evaluated with both the data series (model and DNS). The value $d_L/2h_b$ is equal to 1.087 and 1.089 for the model of Senecal et al. [75] and DNS data, respectively: this agreement suggests that the similar phenomenon can be taken into account in both the analysed cases (model [75] and DNS). Therefore, using Eq. 3.35, the characteristics of the break-up wave in the DNS simulations can be evaluated ($K_{S,DNS}$), and consequentially its growth rate can be defined assuming that the same growth rate spectrum defined with the Senecal et al. [75] model with the same input information. With these data extracted from the simulation the new break lenght $L_{b,n}$ is equal to 3.11, which is very close to the value estimated with the DNS. All the information related to this investigation are resumed in Table 5.4.

	$K_s h_o$	$\Omega_s h_o/U$	L_b/d_o	$2h_b/2h_o$	d_L
Senecal et al. [75]	8.728	0.585	1.648	0.390	42.408
DNS	14.092	-	3.569	0.236	26.376
Imposed $K_s \Rightarrow$ [75]		0.309	3.113	0.257	27.105

Table 5.4: Characteristic wave responsible of the break-up defined by Sencal et al. [75] model and from the DNS for case 1 in Table 4.1; the last row shows the characteristic wave defined from the DNS, imposing the value of $K_s = K_{S,DNS}$ into the Senecal et al. [75] model.

This result can be linked to the effects of turbulence, which can modify the growth rate of the initial perturbation spectrum over the liquid surface, in particular damping the wave with low wave number (the filtering effect linked to the grid size can be excluded due to the fact that also for this wave, the maximum cell size is equal to 22.22 μm). However, to properly validate this theory, further investigation must be conducted, also to exclude any other influence linked to the model assumptions as the initial velocity, which is uniform, constant and its magnitude does not change after the liquid injection (no drag effect induced on the jet by the environmental gas).

The ratio d_D/d_L is defined by the Weber [90] relation $1.88(1+3Oh)^{1/6}$ into the Senecal et al. [75] model: this relation had been defined for a

cylindrical viscous jet and it is equal to 1.93 for the case under investigation. The same ratio calculated with the DNS data is equal to 1.40 ± 0.61, which shows that the Weber [90] relation is in rather good agreement with the DNS simulation of the conical swirled jet break-up.

Influence of the ambient pressure on the atomization process

DNS are also performed for the cases No. 3, 5 and 6 listed in Table 4.1, where the liquid mass flow rate does not significantly change if compared with the previous investigated case (case 1), but the environmental gas properties change, accordingly to the variation of the ambient pressure. For all the cases, the grid have been generated such as to have a KF equals to 8.4, 9.3 and 8.4 for the case 3, 5 and 6 respectively, on the same geometry described in section 5.2.2. The inlet realistic velocity profiles have been used.
Table 5.5 reports all the results extracted from the DNS for all the cases, while Figure 5.18 shows the 3D jet after 0.3 ms of the simulation start for all the investigated cases: as it can be seen case 1 and 3 seems to break-up following the same atomization process; the other two cases, which have lower gas density, seem to be characterized by a different atomization process.

Case No.	L_b/d_o	$2h_b/2h_o$	$d_{L,DNS}[\mu m]$	$SMD[\mu m]$
1	3.569	0.236	26.376	40.329
3	3.843	0.183	28.914	42.913
5	3.839	0.169	24.322	36.797
6	3.408	0.181	32.286	47.042

Table 5.5: Data extracted from the DNS for the cases 1, 3, 5 and 6 listed in Table 4.1.

It must be noticed that case 6 and 1 differ only for the environmental gas density; also the grid adopted is the same for both the cases. Therefore, the only parameter that can yields to this difference it ambient gas density,

as also pointed out into the Senecal et al. [75] model.
Observing the 3D jet obtained from the DNS for cases 5 and 6, it seems that the jets break-up following the rim mode sheets. Under this condition, the jet break-up strongly depends from the grid resolution (connected to the thinning of the liquid film), which yields to adopt a finer grid to properly evaluate the film rupture. Therefore, further investigations on finer grids must be conducted to properly confirm this hypothesis.

The Senecal et al. [75] model has been adopted also for case 3, and the comparison between the DNS data and the model are reported in Table 5.6. For this case, the break-up length and ligament diameter predicted by the analytical model are smaller than the same values extracted from the simulation. The same analysis for case 1 on the shift in wave number, imposed mainly by turbulence effect (damping at low wave number), has been carried out, and the result confirm what has been found previously: the "corrected" unstable wave yields to have a break-up estimation closer to the DNS data, respect of what has been obtained following the analytical model of Senecal et al. [75].

	$K_s h_o$	$\Omega_s h_o/U$	L_b/d_o	$2h_b/2h_o$	d_L
Senecal et al. [75]	6.145	0.299	3.195	0.213	36.096
DNS	8.663	-	3.843	0.183	28.914
Imposed $K_s \Rightarrow$ [75]		0.235	4.071	0.175	27.582

Table 5.6: Characteristic wave responsible of the break-up defined by Sencal et al. [75] model and from the DNS for case 3 in Table 4.1; the last row shows the characteristic wave defined from the DNS, imposing the value of $K_s = K_{S,DNS}$ into the Senecal et al. [75] model.

This result suggest that the turbulence effect can have an important influence during the atomization process, but however further investigations must be conducted to prove it.

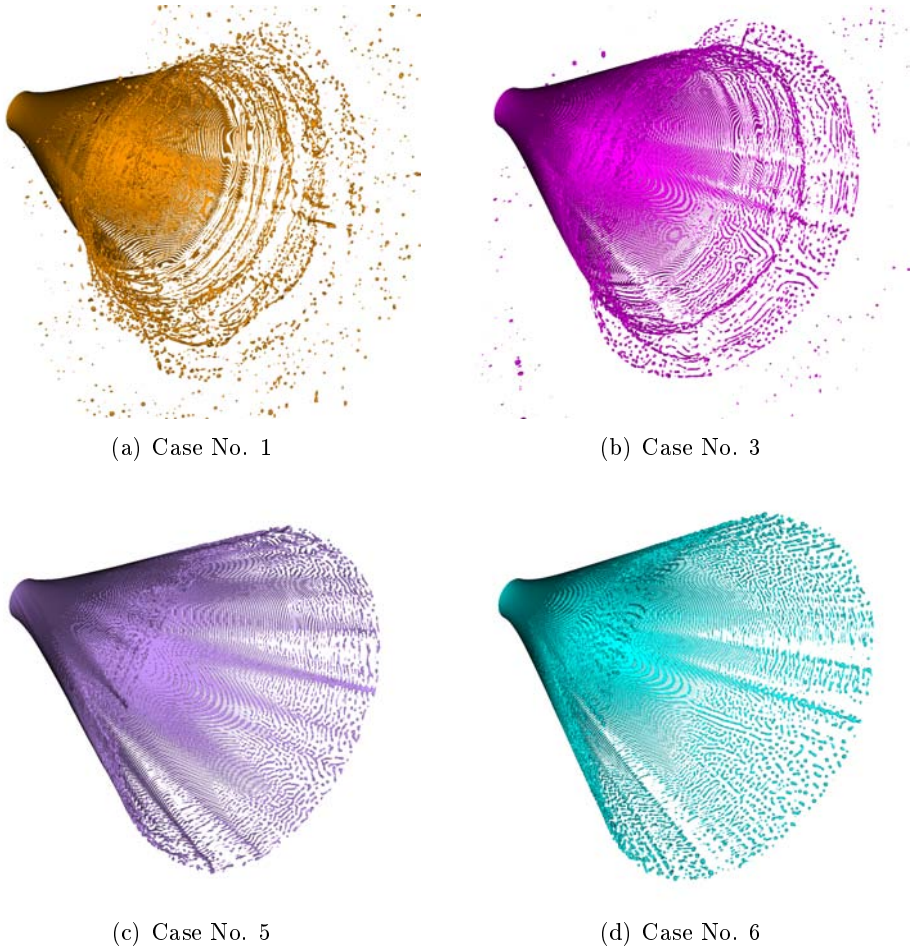

(a) Case No. 1

(b) Case No. 3

(c) Case No. 5

(d) Case No. 6

Figure 5.18: 3D jet visualization for case 1, 3, 5 and 6 listed in Table 4.1, evaluated at 0.3 ms after the beginnig of the simulation.

5.5.3 Jet instability propagation

The break-up of the liquid jet exiting the nozzle is caused by the unstable growth of disturbances on the jet surface, due to the aerodynamic inter-

action between the liquid jet and the environmental gas (Kelvin-Helmoltz instability). Among the spectrum of wavelengths characterising the disturbance, the fastest growing wave is the one that is directly responsible of the liquid jet rupture and it can be visually detected in the simulation results, as shown in Figure 5.19. The results evidence that the sinusoidal (anti-symmetric) wave is responsible of the jet break-up, while no evidence of varicose (symmetric) wave is found, in accordance with the theoretical predictions for these operating conditions [75]. From the extracted data, it is possible to measure the wavelength of the fastest growing disturbance, as evidenced also in Figure 5.19. Table 5.7 reports, for test cases of 1 and 3 listed in Table 4.1, which from the previous analysis show the presence of the wave break-up mode: the values of wavelength are extracted from the numerical simulations and predicted by the well-known model of Senecal et al. [75]. The wavelengths λ predicted by the numerical simulations are much larger than those predicted by the linear stability model, suggesting that further analysis is needed both in the DNS and analytical approaches.

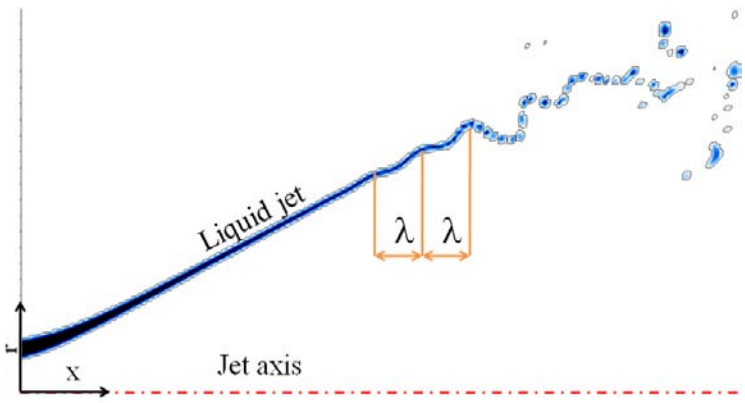

Figure 5.19: Jet profile extracted from numerical simulations, showing the sinusoidal instability that causes the jet break-up.

The above mentioned discrepancies, together with the previous differences found for the break-up length, could possibly be connected to the

Case	Senecal et al. [75]	DNS evaluation
1	35.9	245.5
3	51.1	264.5

Table 5.7: wavelength λ of the fastest growing disturbance; all the reported values are expressed in μm.

peculiarities of the air flow around the break-up region. Figure 5.20 shows the existence of a gas vortical structure which appears to strongly interact with the liquid jet that enhancing the aerodynamic effects that clearly accounted for by simplified analytical models. This suggests that further investigation are necessary to fully understand the complex gas/liquid interaction phenomena and their effect on the jet stability and break-up.

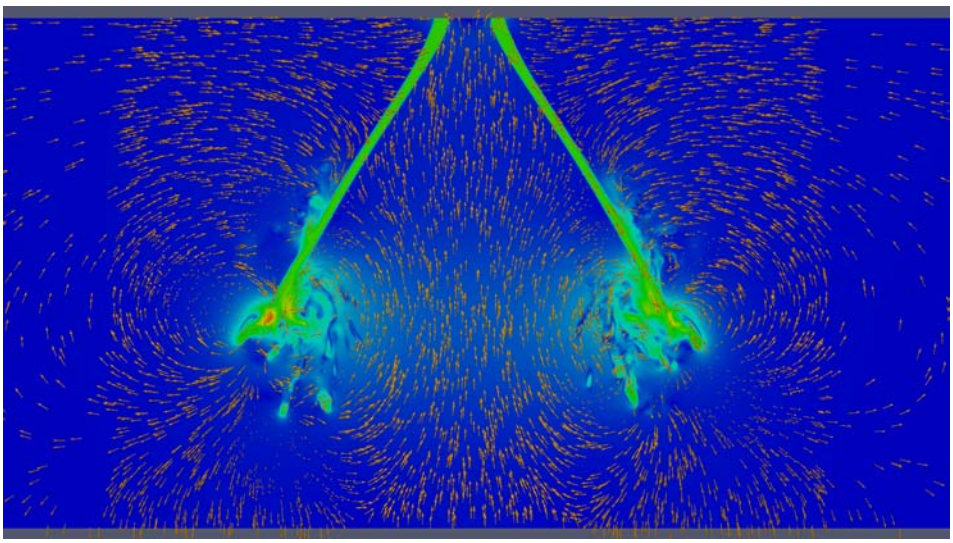

Figure 5.20: Slice of the solution along xy plane with $z = 0$ at 0.2 ms after the simulation start: the color map represents the velocity magnitude, while the vectors show the direction of the flow.

Chapter 6

Conclusions and future developments

The work proposed in the previous chapters has the purpose to provide additional information on the break-up process for conical swirled jet. However, the correct estimation of the jet development and its subsequent break-up, requires a good estimation of the initial jet velocity at nozzle exit. To properly define these informations, numerical simulations of the internal flow field, on a specific pressure swirl atomizer for aero-engine applications, have been performed, and the results are used as inputs for the successive investigations. The conical swirled jet break-up has been investigate by means of the Free Surface 3D (FS3D), a multiphase DNS solver.

6.1 Internal nozzle flow

In order to provide all the information of the emerging jet, 3D VOF simulations have been performed on the selected atomizer. On this geometry, a grid dependence analysis has been carried out for one condition and adopting the RNG $k - \epsilon$ turbulence model: the results show that the solution becomes grid independent for a number of cells higher or equals to 8 mil-

lions.
For all the selected operating conditions, the estimated values of liquid lamella thickness $2h$ at the exit section of the atomizer and the discharge coefficient C_d have been compared with the correlations available in literature, with the aim to define if some of them are able to correctly predict the flow behaviour. The results show a good agreement between the numerical data and the Suyary and Lefebvre [82] and Giffen and Muraszew [24] correlations; for the discharge coefficients, all the investigated correlations are in agreement with the numerical results.
The complexity of the investigated flow, does not allow to clearly identify the nature of the internal nozzle flow. For this reason, a sensitivity analysis on the variation of the turbulence model selected has been carried out. The RNG $k-\epsilon$, the RSM and LES are performed on one test case to evaluate their effect on the prediction of the liquid lamella thickness at the exit section of the atomizer, and the velocity profiles variations. The results show that the the RNG $k-\epsilon$ model predicts results closer to the LES and with the available correlations, while the RSM is able to predict a realistic behaviour of the internal nozzle flow, but with lower accuracy than for the other two turbulent models.
All this data are then used to investigate the liquid atomization process.

6.2 Primary break-up of the conical swirled jet

The primary break-up of the conical swirled jet has been investigated adopting a 3D multiphase DNS (FS3D) solver. The merging jet characteristics are used not only to set as input parameter to the simulation, but they are also used to properly generate the calculation grid. A sensitivity grid dependence study has been carried out, where a uniform inlet profiles, obtained from a previous RNG $k-\epsilon$ simulation of the internal nozzle flow, are set as input data. The break-up length and the mean characteristics droplet diameters (SMD and d_{30}) are used to evaluate the grid effect. The results show that for grid with Kolmogorov Factor $KF \leq 9$, there is no effective variation on the prediction of the investigated atomization parameters.

An investigation on the break-up mechanism has been carried out imposing the velocity profiles extracted from the previous LES numerical simulations of the internal nozzle flow and the corresponding averaged uniform profiles, for one test case. The comparison of spray characteristics shows that the uniform velocity profiles produce a spray with a lower number of droplets than for the case where the realistic initial jet velocity profiles is imposed: this is connected to the fact that the uniform velocity profiles induce the ligaments to be attached to the jet main body further downstream. This liquid connection yields the ligaments to not further atomize in droplets, which consequentially affects the spray characteristics: this can be clearly understood observing the droplet size distribution for both the cases. Therefore, the realistic velocity profiles must be preferred to properly evaluate the conical swirled jet break-up obtained from a pressure swirl atomizer.
The jet development extracted from the DNS is compared with the validated analytical model provided by Nonnenmacher and Piesche [57]. The results show that the model and the DNS data of the jet are in good agreement, demonstrating the correct implementation of the generated inlet boundary and the correct jet behaviour before its break-up.
The spray formation predicted with the DNSs for four operating conditions, is compared with the data predicted with the analytical model of Senecal et al. [75]. The comparison shows some differences, all linked to the break-up length: indeed the Senecal et al. [75] model predicts a lower value of break-up length, which yields to have a thicker film at the break-up point. This consequentially induces to have larger ligaments and droplets. However, the ratio between the ligament diameter and the value of the liquid lamella thickness at the break-up point predicted with the model is similar to the value extracted from the DNSs for the two cases with higher gas density: this result suggests that the same break-up mechanisms are taken into account in both the cases, and the only difference is linked to the correct estimation of the break-up wavelength and the related growth rate. Indeed, imposing into the analytical model the wavelength responsible of the break-up extracted from the DNS, and assuming that the waves growth does not change, the atomization process and the consequentially spray characteristics between the model and the simulation are in rather good agreement.

This result suggests that the turbulence effects can influence the effective growth of the perturbation waves. In particular it seems that turbulence damps the waves at low wave number. Further investigation must be conducted to validate this hypothesis on the break-up process. Changing the gas density, a different break-up mode have been recognized: indeed for the two cases at higher gas density ($\rho_g > 6kg/m^3$), the waves development over the jet surface can be recognized, suggesting that the wave break-up mode it is the responsible of the lamella break-up; for the two cases at lower gas density ($\rho_g \leq 6kg/m^3$), no wave can be identified over the jet surface, and the rupture of the jet seems to be induced by the rim break-up mode. However, to truly verify this assumptions, further investigations must be carried out on a finer grid for these two cases, due to the fact that this kind of break-up mode is strongly influenced by the grid resolution.
The latter result confirms that the gas density has an important role on the atomization process of a conical swirled jet.

6.3 Future developments

The proposed numerical investigation on the primary break-up can be applied to any kind of pressure swirl atomizer. The main aspects that must be further investigated concerning the definition of the wave responsible of the lamella break-up. Indeed from the DNS data a shift to high wave numbers has been observed respect to the analytical break-up model predictions. This shift in wave numbers can be connected to the presence of turbulence which influences the waves development. However, to truly verify this hypothesis further investigations considering more operating conditions must be carried out. Connected to the investigation on different operating conditions, there is the grid dependence analysis: indeed, as pointed out previously, changing the ambient gas density, a different break-up mode can be responsible of the lamella break-up (rim mode instead of the wave mode). This different break-up mode is strongly affected by the grid resolution, which consequentially influences the jet break-up and the primary spray characteristics. Therefore, at low ambient gas density, a grid depen-

dence study must be carried out, as it is already done for one case at higher gas density.
Moreover, a large vortex structures have been observed at the tip of the jet: their characteristics can help to better understand the atomization process for a conical swirled jet. Indeed, these vortex structures influence the jet before its break-up point, and their effect on the atomization process must be defined.
Another important aspect that must be further investigate concerning the liquid structures characteristics produced after the primary break-up: the common atomization models assume that the jet breaks into ligaments and then in spherical droplets. With the DNSs simulation, liquid structures with different aspect ratio AR have been found, showing that only a small part of them are approximately spherical. The liquid structures shape has an important role on the sub-sequent atomization process and evaporation rate, and therefore further investigations must be carried out to characterize it.

Appendix A

Semi-empirical correlations

In this appendix, a list of semi-empirical correlations able to describe the PSA behaviour are reported, together with the corresponding validity range.

A.1 Liquid lamella thickness $2h$

This section reports the mainly adopted semi-empirical correlations able to define the liquid lamella thickness. Some of them depends on different parameter, which are:

- X represents the ration of the air-core area and the total outlet area of the atomizer

$$X = \frac{A_{ac}}{A_o} = \frac{[d_o - 2(2h)]^2}{d_o^2} \tag{A.1}$$

- FN is the Flow Number, defined as

$$FN = \frac{\dot{m}_l}{(\Delta P \rho_l)^{0.5}} \tag{A.2}$$

- K represents the ratio between the total inlet area and the product of the swirl chamber and outlet diameter

$$K = \frac{A_i}{d_s d_o} \tag{A.3}$$

Rizk and Lefebvre [67]

$$(2h)^2 = \frac{1560 \dot{m}_l \mu_l}{\rho_l d_o \Delta P} \frac{1+X}{(1-X)^2} \tag{A.4}$$

Validated for the following operating conditions:

$$\begin{gathered} 6.9 < \Delta P < 27.0 bar \\ P_c = 101325 Pa \\ 8.0 < d_s < 10.0 mm \\ 1.2 < d_o < 2.4 mm \end{gathered}$$

Suyari and Lefebvre [82]

$$2h = 2.7 \left[\frac{d_o F N \mu_l}{\Delta P \rho_l} \right]^{0.25} \tag{A.5}$$

Validated for the following operating conditions:

$$\begin{gathered} 6.9 < \Delta P < 27.0 bar \\ P_c = 101325 Pa \\ 8.0 < d_s < 10.0 mm \\ 1.2 < d_o < 2.4 mm \end{gathered}$$

Fu et al. [21]

$$2h = 3.1 \left[\frac{d_o F N \mu_l}{\Delta P \rho_l} \right]^{0.25} \tag{A.6}$$

Giffen and Muraszew [24]

$$\left(\frac{A_i}{d_s d_o}\right)^2 = \frac{\pi^2}{32}\frac{(1-X)^3}{X^2} \tag{A.7}$$

This formulation is based on the inviscid theory. From Radcliffe [61], the emerging flow can be considered inviscid if $Re_o > 3000$.

Lefebvre [48]

$$\frac{(1-X)^3}{1+X} = 0.09\frac{A_i}{d_s d_o}\sqrt{\frac{d_s}{d_o}} \tag{A.8}$$

This formulation is based on the inviscid theory. From Radcliffe [61], the emerging flow can be considered inviscid if $Re_o > 3000$.

Benjamin et al. [3]

$$2h = \frac{0.253K^{0.33}}{\Delta P^{0.077} F N^{0.4}} \tag{A.9}$$

Validated for the following operating conditions:

$$\begin{gathered} 0.69 < \Delta P < 3.45bar \\ P_c = 101325Pa \\ d_s = 76mm \\ d_o = 18mm \end{gathered}$$

A.2 Discharge Coefficient C_d

Carlisle [5]

$$C_d = 0.0616\frac{d_s}{d_o}\frac{A_i}{d_s d_o} \tag{A.10}$$

This formulation is based on the inviscid theory. From Radcliffe [61], the emerging flow can be considered inviscid if $Re_o > 3000$.

Rizk and Lefebvre [68]

$$C_d = 0.35 \left(\frac{A_i}{d_s d_o} \right)^{0.5} \left(\frac{d_s}{d_o} \right)^{0.25} \tag{A.11}$$

This formulation is based on the inviscid theory. From Radcliffe [61], the emerging flow can be considered inviscid if $Re_o > 3000$.

Taylor [83]

$$C_d^2 = 0.225 \frac{A_i}{d_s d_o} \tag{A.12}$$

This formulation is based on the inviscid theory. From Radcliffe [61], the emerging flow can be considered inviscid if $Re_o > 3000$.

Giffen and Muraszew [24]

$$C_d = 1.17 \sqrt{\frac{(1-\widetilde{X})^3}{1+\widetilde{X}}} \tag{A.13}$$

where $\widetilde{X}$ is defined resolving the following equation:

$$2 \left(\frac{4K}{\pi} \right)^2 \widetilde{X}^2 = (1-\widetilde{X})^3 \tag{A.14}$$

This formulation is based on the inviscid theory. From Radcliffe [61], the emerging flow can be considered inviscid if $Re_o > 3000$.

Babu et al. [1]

$$C_d = \frac{K_{C_d}}{\sqrt{\frac{1}{(1-X)^2} + \frac{\left(\frac{\pi}{4B}\right)^2}{X^n}}} \tag{A.15}$$

Where:

$$K_{C_d} = 7.3423 \frac{A_o^{0.13735} A_s^{0.07782}}{A_i^{0.041066}} \quad B = \frac{A_i}{d_m d_o} \left(\frac{d_m}{d_o} \right)^{1-n} \tag{A.16}$$

$$n = \begin{cases} 17.57 \frac{A_o^{0.1396} A_i^{0.2336}}{A_s^{0.1775}} & \text{if } \Delta P \geq 27.6 \text{ bar} \\ 28 \frac{A_o^{0.14176} A_i^{0.27033}}{A_s^{0.17364}} & \text{if } 6.9 < \Delta P < 27.6 \text{ bar} \end{cases}$$

A.3 Spray cone angle 2θ

Rizk and Lefebvre [69]

$$2\theta_m = 6K^{-0.15} \left(\frac{\Delta P d_o^2 \rho_l}{\mu_l^2} \right)^{0.11} \tag{A.17}$$

List of Figures

List of Tables

List of publications

International journals and book

1. Galbiati C., Tonini S., Conti P. and Cossali G. E. (2015). Numerical simulations of internal nozzle flow in a pressure swirl atomizer for aircraft engines. *Submitted for publication in Journal and Propulsion and Power*, 2015.

2. Galbiati C., Ertl M., Tonini S., Cossali G. E. and Weigand B. (2015). DNS investigation of the primary break-up in a conical swirled jet. *High performance computing in science and engineering '15*, 2015.

Conference proceedings

1. Galbiati C., Tonini S., Cossali G. E. and Weigand B. (2015). (2014). DNS investigation of conical swirled jet break-up. *DIPSI Workshop 2015, Bergamo, Italy*, 2015.

2. Tonini S., Galbiati C., Belotti A. and Cossali G. E. (2014). Modelling of spray formation in a pressure swirl atomizer for aircraft engines. *Proceedings of ILASS Europe 2014, 8-10 Semptember 2014, Bremen, Germany*, 2014.

Bibliography

[1] Babu, K. R. Narasimhan, M. V., and Narayanaswamy, K. Correlations for prediction of discharge rate, core angle and air core diameter of swirl spray atomizers. In *Proceedings of 2nd ILASS America* (Madison, Wisconsins, 1982), pp. 91–97.

[2] Bayvel, L., and Orzechowski, Z. *Liquid Atomization.* Taylor and Francis, 1993.

[3] Benjamin, M. A. Jeng, S. M., and Jog, M. A. Comparison of simplex atomizer correlations with detaild cfd and experimental data. In *Proceedings of the 10th ILASS America Conference* (1997).

[4] Brackbill, J. U. Kothe, D. B., and Zemach, C. A continuum method for modeling surface tension. *J Computation Physics 100* (1992), 335–354.

[5] Carlisle, D. R. Communication on the performance of a type swirl atomizer. In *Proc. Ins. Mech. Eng.* (1955), vol. 169.

[6] Chinn, J. J. *The internal flow physics of swirl atomizer nozzles.* PhD thesis, University of Manchester Institute of Science and Technology, Thermo-Fluids Division, Department of Mechanical Engineering, October 1996.

[7] Chinn, J. J., and Yule, A. J. Computational analysis of swirl atomizer internal flow. In *Proceeding of ICLASS conference '97* (March 1997).

[8] Datta, A., and Som, S. Numerical prediction of air core diameter, coefficient of discharge and spray cone angle of a swirl spray pressure nozzle. *International journal of heat and fluid flow 21* (2000), 412–419.

[9] De Keukelaere, H. J. K. The internal flow in a swirl atomizer nozzle. Master's thesis, Dept. Mech. Eng. UMIST, 1995.

[10] Dombrowski, N., and Hooper, P. C. The effect of ambient density on drop formation in sprays. *Chem. Eng. Sci. 17* (1962), 291–305.

[11] Dombrowsky, N., and Hasson, D. The flow characterisitcs of swirl (centrifugal) spray pressure nozzles with low viscosity fluids. *AIChE J. 17* (July 1969), 604–611.

[12] Dombrowsky, N., and Jhons, W. R. The aerodynamic instability and disintegration of viscous liquid sheets. *Chemical Engineering Science 18* (1963), 203–214.

[13] Donjat, D., E. J. L., and Michau, M. A description of the pressure swirl atomizer internal flow. In *ASME proceedings FEDSM '02* (Montreal, Quebec, Canada, July 2002), vol. FEDSM2002-31017.

[14] Donjat, D. Estivaleze, J. M. M., and Lavergne, G. Phenomenological study of the pressure swirl atomizer internal flow. In *Proceeding of 9th ICLASS conference* (Sorrento, Italy, July 2003).

[15] Dumochel, C. A new formulation of the maximum entropy formalism to model liquid spray drop size distribution. *Part. Syst. Char. 23* (2006), 468–479.

[16] Dumochel, C. Cousin, J., and Triballier, K. Experimental analysis of liquid-gas interface at low weber number: interface length and fractal dimension. *Experiments In Fluids 39* (2005), 651–666.

[17] Ebbesen, K. Measurement and observation of flow characterisitc of two low pressure swirl atomizer. Master's thesis, Dept. Mech. Eng. UMIST, 1995.

[18] Escudier, M. P. Bornstein, J., and Zehnder, N. Observations and lda measurements of confined turbulent vortex flow. *J. FLuid Mech. 98* (1980), 49–64.

[19] et al., E. Direct numerical simulations for multiphase flows: An overview of the multiphase cose fs3d. *Applied Mathematics and Computation* (June 2015), 1–10.

[20] Fraser, R. P., and Eisenklam, P. Research into the performance of atomizers for liquid. *Imp. Coll. Chem. Eng. Eng. Soc. J. 7* (1953).

[21] Fu, Q. Yang, L., and Qu, Y. Measurement of annular liquid film thickness in an open-end swirl injector. *Aerospace Science and Technology 15* (2011), 117–124.

[22] Gatski, T. B., and Speziale, C. G. On explicit algebraic stress models for complex turbulent flows. *J Fluids Mech 254* (1993), 59–78.

[23] Giffen, E., and Massey, B. S. Some observations on flow in spray nozzles. Tech. Rep. 1950/5, The motor industry res. assoc., 1950.

[24] Giffen, E., and Muraszew, A. *The Atomization of Liquid Fuels.* Chapman & Hall, London, UK, 1953.

[25] Gorokhovski, M., and Herrmann, M. Modeling primary atomization. *Annual Review of Fluid Mechanics 40*, 1 (2008), 343–366.

[26] Halder, M.R. Dash, S., and Som, S. Initiation of air core in a simplex nozzle and the effects of operating and geometrical parameters on its shape and size. *Experimental thermal and fluid science 26* (2002), 871–878.

[27] Hanjalic, K., and Launder, B. E. A reynolds stress model of turbulence and its application to thin shear flows. *Journal of Fluid Mechanics 52* (4 1972), 609–638.

[28] Hansen, K.G. Madsen, J. T. C. M. I. C. H. S. T., and Hjertager, B. H. A computational and experimental study of the internal flow in a scaled pressure-swirl atomizer. In *Proceeding of 18th ILASS Europe conference* (Zaragoza, Spain, September 2002).

[29] Harlow, F. H., and Welch, J. E. Numerical calculation of time-dependent viscous incompressible flow of fluid with free surface. *Physics of Fluids 8*, 12 (1965), 2182–2189.

[30] Hirsch, C. *Numerical computation of internal & external flows*. John Wiley & Sons, Ltd., 2007.

[31] Hirt, C. W., and Nichols, B. D. Volume of fluid (VOF) method for the dynamics of free boundaries. *Journal of Computational Physics 39*, 1 (Jan. 1981), 201–225.

[32] Horvay, M., and Leuckel, W. Lda-measurements of liquid swirl flow in converging swirl chambers with tangential inlets. p. 11.

[33] Horvay, M., and Leuckel, W. Experimental and theoretical investigation of swirl nozzles for pressure-jet atomization. *German chemical engineering 9*, 5 (1986), 276–283.

[34] Hsieh, K. T., and Rajamani, R. K. Mathematical model of the hydrocyclone based on physics of fluid flow. *AIChE Journal 33*, 5 (May 1991), 735–746.

[35] Huh, K. Y., and Gosman, A. D. A phenomenological model of diesel spray atomization. In *Proceeding of the international conference on multiphase flows* (Tsukuba, 1991), vol. 2, pp. 515–518.

[36] Jedelský, J., and Jícha, M. Energy considerations in sprays process of a spill-return pressure-swirl atomizer. *Applied Energy 132* (2014), 485–495.

[37] Jedelský, J. Malý, M. H. M., and Jícha, M. Some aspects of disintegration of annular liquid sheet in pressure-swirl atomization. In *Proceeding of 16th ICFFT* (Budapest, Hungary, September 2015).

[38] Jeng. S. M, Jog, M. A., and Benjamin, M. A. Computational and experimental study of liquid sheet emanating from simplex fuel nozzle. *AIAA Journal 36* (1998), 201–207.

[39] Kim, J. Moin, P., and Moser, R. Turbulence statistics in fully developed channel flow at low reynolds number. *Journal of Fluid Mechanics 177* (4 1987), 133–166.

[40] Kong, W. K. To investigate and understanding the performance of rpessure swirl nozzles for producing water sprays. Master's thesis, Dept. Mech. Eng. UMIST, 1994.

[41] Koo, J. Y., and Martin, J. K. Near-nozzle characteristics of a transient fuel spray. *Atomization and Spray 5* (1995), 107–121.

[42] Kornev, N., and Hassel, E. Method of random spots for generation of synthetic inhomogeneous turbulent fields with prescribed autocorrelation functions. *Communications In Numerical Methods In Engineering 23*, 1 (Jan. 2007), 35–43.

[43] Kutty, S. P. Narasimhan, M. V., and Narayanaswamy, K. Prediction of the coefficient of discharge of swirl chamber atomizers. Tech. rep., 1978.

[44] Launder, B. E., and Sharma, B. I. Application of the energy-dissipation model of turbulence to the calculation of flow near a spinning model disc. *Lett Heat Mass Transf 1* (1974), 131–138.

[45] Launder, B. E., and Spalding, D. B. The numerical computations of turbulent flows. *Computational Methods Appl Mech Eng 3* (1974), 269–289.

[46] Lawrence, O. *Proc. Inst. Mech. Engr 157* (1947).

[47] Lee, E. J. Oh, A. Y. K. H. Y. S. C. J., and Yoon, S. S. Measuring air core characteristics of a pressure-swirl atomizer via a transparent acrylic nozzle at various reynolds numbers. *Experimental Thermal and Fluid Science 34* (2010), 1475–1483.

[48] Lefebvre, A. H. *Atomization and Sprays.* Hemispher, New York, 1989.

[49] Levich, V. G. *Physicochemical Hydrodynamics.* Prentice-Hall, New Jersey, 1962.

[50] Madsen, J. Hjertager, B. H., and Solberg, T. Numerical simulation of internal flow in a large-scale pressure-swirl atomizer. In *Proceeding of 19th ILASS Europe conference* (Nottingham, UK, September 2004).

[51] Mandal, B. Barman, P., and Kushari, A. Study of primary atomization in a helical passage pressure-swirl atomizer. In *Proceeding of 19th ILASS Europe conference* (Nottingham, UK, September 2004).

[52] Mani, J., N. S., and Rao, M. Atomization of pressure nozzles. *Trans. indian inst. chem. engrs. 12* (1960).

[53] Moin, P., and Mahesh, K. Direct numerical simulation: A tool in turbulence research. *Annual Review of Fluid Mechanics 30*, 1 (1998), 539–578.

[54] Moon, S., and Bae, C. Estimation of the breakup length for a pressure-swirl sray from the experimentally measured spray angle. 235–246.

[55] Moser, R. D., and Moin, P. The effects of curvature in wall-bounded turbulent flows. *Journal of Fluid Mechanics 175* (2 1987), 479–510.

[56] Nagano, Y., and Hishida, M. Improved form of the $k-\epsilon$ model for wall turbulent shear flows. *J Fluids Eng 109* (1987), 131–138.

[57] Nonnenmacher, S., and Piesche, M. Design of hollow cone pressure swirl nozzles to atomize newtonian fluids. *Chemical Engineering Science 55*, 19 (2000), 4339 – 4348.

[58] Panchangula, M. V. Sojka, P. E., and Santangelo, P. J. On the three-dimensional instability of a swirling, annular, inviscid liquid sheet subject to unequal gas velocities. *Phys. Fluids 8*, 12 (1994), 3300–3312.

[59] Park, B. S. Kim, H. Y., and Yoon, S. S. Transitional instability of a pressure-swirl atomizer due to air core eruption at low temperature. *Atomization Sprays 17* (2007), 551–568.

[60] Patankar, S. V. *Numerical Heat Transfer and Fluid Flow.* Hemisphere, Washington DC, 1980.

[61] Radcliffe, A. The performance of a type of swirl atomizer. In *Proc. Inst. Mech. Eng.* (1955), vol. 169, pp. 93–106.

[62] Ramamurthi, K., and Tharakan, T. J. *AIAA Journal 36*, 3 (March 1998), 420–427.

[63] Reitz, R. D., and Braco, F. V. Mechanism of breakup of round liquid jets. In *Encyclopedia of Fluid Mechanics.* Gulf Pub, Huston, Texas, USA, 1986, pp. 233–249.

[64] Rider, W. J., and Kothe, D. B. Reconstructing volume tracking. *Journal of Computational Physics 141*, 2 (Apr. 1998), 112–152.

[65] Rieber, M. *Numerische Modellierung der Dynamik freier Grenzflächen in Zweiphasenströmungen.* PhD thesis, University of Stuttgart, 2004.

[66] Rizk, N. K., and Lefebvre, A. H. Influence of liquid properties on the internal flow characteristcs of simplex swirl atomizers. In *ASME proceedings 1985* (1985), vol. 85-WA/HT-49.

[67] Rizk, N. K., and Lefebvre, A. H. Influence of liquid properties on the internal flow characteristics of simplex swirl atomizers. *Atomisation and Spray Technology 2*, 3 (1985), 219–233.

[68] Rizk, N. K., and Lefebvre, A. H. Internal flow characteristcs of simplex swirl atomizers. *Journal of Propulsion 1*, 3 (1985), 193–199.

[69] Rizk, N. K., and Lefebvre, A. H. Prediction of velocity coefficient and spray cone angle for simplex atomizers. In *Proceedings of the 3rd international conference on liquid atomizazion and spray systems (ILASS)* (London, 1985), pp. 111C/2/1–16.

[70] Rizk, N. K., and Lefebvre, A. H. Influence of liquid properties on the internal flow characteristics of simplex swirl atomizers. *Atomisation and Spray 2*, 3 (1986), 219–233.

[71] Rogers, M. M. *The structure and modeling of the hydrodynamic and passive scalar fields in homogeneous turbulent shear flow.* PhD thesis, Stanford University, 1986.

[72] Sakman, A. T. Jog, M. A., and M., J. S. Parametric study of simplex fuel nozzle internal flow and performance. *AIAA Journal 38*, 7 (July 2000), 1214–1218.

[73] Santolaya, J. Aisa, L. C. E. G. I. n. C. L. Experimental study of near-field flow structure in hollow cone swirl sprays. *Journal of Propulsion and Power 23*, 2 (2007), 382–389.

[74] Savini, M. Turbulence and turbulence models.

[75] Senecal, P. K. Schmidt, D. P. R. C. J. R. R. D., and Corradini, M. L. Modeling high-speed viscous liquid sheet atomization. *International Journal of Multiphase Flow 25*, 6-7 (1999), 1073–1097.

[76] Sirignano, W. A., and Mehring, C. Review of theory of distortion and disintegration of liquid streams. *Progress in Energy anc Combustion Science 26* (2000), 609–655.

[77] Sleicher, C. A., and Sterlig, A. M. The instability of capillary jets. *J. Fluid Mechanics 68* (1975), 477–495.

[78] Söhngen, F., and Grigull, U. *Forsch. Geb. Ingenieurwes. 17*, 3 (1951), 77–82.

[79] Spalart, P. R. Direct simulation of a turbulent boundary layer up to Rθ = 1410. *Journal of Fluid Mechanics 187* (2 1988), 61–98.

[80] Squire, H. B. Investigation of the instability of a moving liquid film. *Brit. J. Appl. Phys. 4* (1963), 167–169.

[81] Sumer, B. Erkan, N. U. O., and Tuncer, I. Experimental and numerical investigation of a pressure swirl atomizer. In *Proceedings of the 12th Triennal International Conference on Liquid Atomization and Spray Systems* (Heidelberg, Germany, September 2-6 2012).

[82] Suyary, M., and Lefebvre, A. H. Film thickness measurements in a simplex swirl atomizer. *Journal of Propulsion and Power 2*, 6 (1986), 528–533.

[83] Taylor, G. I. The boundary layer in the converging nozzle of a swirl atomizer. *The quarterly journal of mechanics and applied mathematics 3*, 2 (1950), 129–139.

[84] Tikhomirov, V. On the degeneration of isotropic turbulence in an incompressible viscous fluid. In *Selected Works of A. N. Kolmogorov*, V. Tikhomirov, Ed., vol. 25 of *Mathematics and Its Applications (Soviet Series)*. Springer Netherlands, 1991, pp. 319–323.

[85] Tonini, S. Galbiati, C. B. A., and Cossali, G. E. Modelling of spray formation in a pressure swirl atomiser for aircraft engines. In *Proc. of ILASS Europe 2014, 26th Annual conference on Liquid Atomization and Spray Systems* (Bremen, Germany, September 8-10 2014), ILASS Europe.

[86] Tratnig, A., and Brenn, G. Drop size spectra in sprays from pressure-swirl atomizers. *Internaional journal of multiphase flow 36* (2010), 349–363.

[87] Ubbink, O., and Issa, R. A method for capturing sharp fluid interfaces on arbitrary meshes original research article. *Journal of Computational Physics 153*, 1 (1999), 26–50.

[88] Villermaux, E. Marmottan, P., and Duplat, J. Ligament-mediated spray formation. *Phys. Rev. Lett. 92*, 074501 (2004).

[89] Walzel, P. Liquid atomization. *Intr. Chem. Eng. 33*, 1 (1993), 46–60.

[90] Weber, C. On the breakdown of a fluid jet. *Z.A.M.P. 11* (1931), 289–298.

[91] Widger, I. R. *Improvement of high pressure water sprays used for coal dust extraction in mine safety.* PhD thesis, Dept. Mech. Eng. UMIST, 1993.

[92] Yakhot, V., and Orszag, S. A. Renormalization group analysis of turbulence. i. basic theory. *Journal of scientific computing 1*, 1 (3 1986), 3–51.

[93] Yeh, C. Turbulent flow investigation inside and outside plain-orifice atomizers with rounded orifice inlets. *Heat Mass Transfer 44*, 1 (2005), 810–823.

[94] Yeh, C. Turbulent flow simulation of liquid jet emanating from pressure-swirl atomizer. *Heat Mass Transfer 44* (2008), 275–280.

[95] Yule, A. J., and Chinn, J. J. Three dimensional computer modelling of the internal flow within a swirl atomizer: an initial investigation. In *PARTEC 95* (Nürnberg, March 1995).

[96] Yule, A. J., and Widger, I. R. Swirl atomizers operating at high water pressure. *Int. J. Mech. Sci. 38*, 8-9 (1996), 981–999.